EXPERIMENTAL AND THEORETICAL STUDIES OF MAGNETIC ALLOYS

Thesis submitted for the degree of

Doctor of Philosophy (Science)

in

Physics (Experimental)

by

Tanmoy Ghosh

Department of Physics
University of Calcutta
March 2017

To my parents . . .

Acknowledgements

The journey of a Ph.D. thesis work takes place in such an important phase of life that it shapes not only one's professional career but every aspects of life and I guess this is true for everyone pursuing a Ph.D. degree. My journey, albeit little longer than usual, has been a colourful, memorable and enjoyable one. I would like to take this opportunity to express my sincere gratitude to all those people who have guided me, motivated me and made this journey wonderful.

First and foremost, I would like to express my sincere gratitude to my supervisor Prof. Pratip Kr. Mukhopadhyay. It is his guidance which always kept me on the right track of the problem and his continuous enthusiasm and encouragement kept me motivated to complete this dissertation. His insistence with long-enduring patience on clarity and critical thinking improve the quality by bringing out various different aspects of the problems and made them presentable in an organized manner. His knowledge and ideas of setting up various experimental methods have always inspired me. Working with him was a rewarding experience and I am indebted to him for the freedom he has given me in exploring various scientific ideas.

I would like to deeply acknowledge Prof. Abhijit Mookerjee for his guidance, particularly in completing the theoretical section of this work. This thesis wouldn't have been possible to complete without his continuous support and guidance. I am greatly indebted to him for introducing and guiding me in the fields of first-principles theories and computational materials science. His constant encouragement was also a critical motivation for me in completing this dissertation.

I am also thankful to Dr. T. Fukuda and Prof. T. Kakeshita of Osaka University for extending various experimental facilities and active collaboration. I sincerely acknowledge Prof. Ranjan Chaudhury and Prof. A. K. Raychaudhuri of our centre, Prof. Sangam Banerjee (SINP, Kolkata), Dr. Dipankar Das (UGC-DAE-CSR, Kolkata), Dr. V. R. Reddy (UGC-DAE-CSR, Indore) and Prof. S. N. Kaul (University of Hyderabad) for their help with various experimental measurements, valuable suggestions and stimulating scientific discussions. I would also like to acknowledge Prof. P. K. Chakrabarti (The University of Burdwan) who encouraged me during my M.Sc. to undertake this journey. I sincerely acknowledge the opportunity and financial support provided by S. N. Bose National Centre for Basic Sciences to carry out this thesis work.

I have been fortunate to have the company of Sandeep'da and Jena'ji: while Sandeep'da introduced me to the various experimental set-up in the laboratory, Jena'ji guided me in the turns of DFT codes and Monte-Carlo simulations. It is my pleasure to thank my lab-mates Arun, Nandan, Sudipta, Inji, Sarowar, Abhishek, Chayan, Alo'di, Tapas, Dr. B. Rajini Kanth and Animesh for providing a cooperative, pleasant and joyful atmosphere in the laboratory. I would also like to thank Shreemoyee'di, Rudra'da, Rajiv'da and Prashant'da for their endless support in first-principles calculations. I am also greatly indebted to Amit for his tireless support in arc-melting in the workshop. I will forever cherish the great company of Debraj'da, Rajib'da, Abhijit, Sandeep Singh'ji, Wasim, Tukun, Ravi, Arindam, Subhajit and Rishi'ji. The endless support and encour-

agement of my friends Anirban, Pathak'da, Srijib'da, Hafijur and Bisu'da were also instrumental in navigating many difficult times in life during this period.

Finally, I would like to thank my parents and elder sister for their unconditional love and support which have been the pillars of my strength and made this journey possible. Their continuous enthusiasm and encouragement in my academic endeavours helped me to tread the path I have travelled so far.

Tanmoy Ghosh
Kolkata
March 2017

List of Publications

1. Electronic and magnetic properties of disordered AuCr alloys : A first-principles study,
   Tanmoy Ghosh, Shreemoyee Ganguly, P.K. Mukhopadhyay and Abhijit Mookerjee,
   Journal of Magnetism and Magnetic Materials **332** (2013) 199.

2. Interesting magnetic behavior of Fe:Al disordered alloys,
   P.K. Mukhopadhyay, **Tanmoy Ghosh** and Abhijit Mookerjee,
   Physica B: Condensed Matter **448** (2014) 226.

3. Effect of short range ordering on the magnetism in disordered Fe:Al alloy,
   Tanmoy Ghosh, Ambika Prasad Jena, Biplab Sanyal, Hirosuke Sonomura, Takashi Fukuda, Tomoyuki Kakeshita, P.K. Mukhopadhyay and Abhijit Mookerjee,
   Journal of Alloys and Compounds **613** (2014) 306.

4. Effects of chemical ordering and composition on the magnetic properties of disordered FeAl alloys,
   Tanmoy Ghosh, Ambika Prasad Jena and Abhijit Mookerjee,
   Journal of Alloys and Compounds **639** (2015) 583.

5. Concomitant antiferromagnetic transition and disorder-induced weak localization in interacting-electron system,
   Tanmoy Ghosh, Takashi Fukuda, Tomoyuki Kakeshita, S. N. Kaul and P.K. Mukhopadhyay,
   Under review.

6. Structural, magnetic and transport properties of disordered $Fe_{1-x}Al_x$ ($0.25 \leq x \leq 0.55$) alloys: on the short-range ordering and lattice parameter anomaly,
   Tanmoy Ghosh, S. Banerjee and P.K. Mukhopadhyay,
   Under preparation.

7. Magnetic properties of $FeAl_{2-x}Ga_x$ ($0 \leq x \leq 0.5$): properties of low temperature spin glass phase and weak interplaner interaction induced antiferromagnetic phase,
   Tanmoy Ghosh, Takashi Fukuda, Tomoyuki Kakeshita, S. N. Kaul and P.K. Mukhopadhyay,
   Under preparation.

Table of Contents

List of Abbreviations

AFM	Antiferromagnetic
ASR	Augmented Space Recursion
ASA	Atomic Sphere Approximation
BCC	Body Centred Cubic
CPA	Coherent Potential Approximation
C_P	Specific heat at constant pressure
C_{lat}	Lattice specific heat
C_{elec}	Electronic specific heat
C_{mag}	Electronic specific heat
DFT	Density Functional Theory
DMFT	Dynamical Mean Field Theory
EDX	Energy Dispersive X-ray analysis
EPMA	Electron Probe Micro-Analysis
EEI	Enhanced electron-electron interactions
FCC	Face centred Cubic
FC	Field Cooled
FM	Ferromagnetic
GPM	Generalized Perturbation Method
GGA	Generalized Gradient Approximation
GPIB	General Purpose Interface Bus
H	Magnetic Field
KKR	Korringa-Kohn-Rostocker
LDA	Local density Approximation
LMTO	Linear Muffin-Tin Orbital
M	Magnetization
MC	Monte-Carlo
M_{ZFC}	Zero field cooled magnetization
M–H	Isothermal Magnetizations
P	Pressure
RKKY	Ruderman-Kittel-Kasuya-Yoshida
SEM	Scanning Electron Microscope

SQS	Special Quasi-random Structure
SRO	Short-Range Ordering
SG	Spin Glass
SQUID	Superconducting Quantum Interference Device
TB-LMTO	Tight-Binding Linear Muffin-Tin Orbital
T	Temperature
T_C	Curie Temperature
T_N	Néel Temperature
T_{sg}	Spin glass transition temperature
T_m	Weak localization temperature
VSM	Vibrating Sample Magnetometer
XRD	X-ray Diffraction
ZFC	Zero Field Cooled
WL	Weal Localization
α	Warren-Cowley order parameter
ρ	Resistivity
σ	Conductivity
χ'	Real part of ac susceptibility
θ_D	Debye Temperature

List of Figures

List of Tables

1 Introduction

1.1 Disordered magnetic alloys

Alloys are metallic materials formed as a mixture of two or more chemical elements, at least one of which is a metal. They have attracted our attention since the ancient times of human civilization due to their improved material properties as well as ability of tuning their properties to the desired target by changing alloy composition, preparation technique or by applying an external stimulus. The discovery of alloys such as brass, bronze, and steel greatly impacted the growth of human civilization. Alloys represent a large family of materials which are apart from their countless applications in our day to day life, are also important to study for understanding the diverse range of novel physical phenomena that occur in these systems. The magnetic alloys form a class of this family which in general contain a magnetic element such as Fe, Co, Ni.

All the material properties invariably depend upon the arrangement of its constituent atoms, which in an alloy is determined by the inter-atomic forces along with the atomic diffusions controlled by the thermodynamic conditions. Based on the atomic arrangements, alloys can be categorized into ordered, substitutional, interstitial and amorphous alloys.

An ordered alloy is formed when the constituent atomic species make a periodic arrangement [1, 2] in the crystal such as shown in Figs. 1.1(a)–(b) for a binary *AB* alloy. The probability $\Pr(\mathbf{R}_i)$ that a lattice site $\mathbf{R}_i$ will be occupied by a particular

type of chemical species is either *one* or *zero* and the knowledge of atomic occupations in the unit cell can be used to map the atomic occupations of all other sites in the whole system with absolute certainty. For example, let's consider a binary *AB* alloy of equiatomic composition as shown in Fig. 1.1(a). The lattice sites can be described by $\mathbf{R}_i = N_1\mathbf{a}_1 + N_2\mathbf{b}_2 + N_3\mathbf{a}_3$ where N_1, N_2, N_3 are all integers or *half*-integers and $\mathbf{a}_1, \mathbf{a}_2, \mathbf{a}_3$ are the lattice parameters. In a perfectly ordered alloy, *A* and *B* atoms will respectively occupy all the lattice sites corresponding to the integer and *half*-integer values of N_1, N_2, N_3 (i.e., $\mathrm{Pr}_A(\mathbf{R}_i) = 1$ for integer values of N_1, N_2, N_3 and $\mathrm{Pr}_A(\mathbf{R}_i) = 0$ for *half*-integer values of N_1, N_2, N_3; $\mathrm{Pr}_B(\mathbf{R}_i) = 1$ for *half*-integer values of N_1, N_2, N_3 and $\mathrm{Pr}_B(\mathbf{R}_i) = 0$ for integer values of N_1, N_2, N_3) or the vice-verse. B2 FeAl, an example of such ordered alloy, is shown in Fig. 1.1(b).

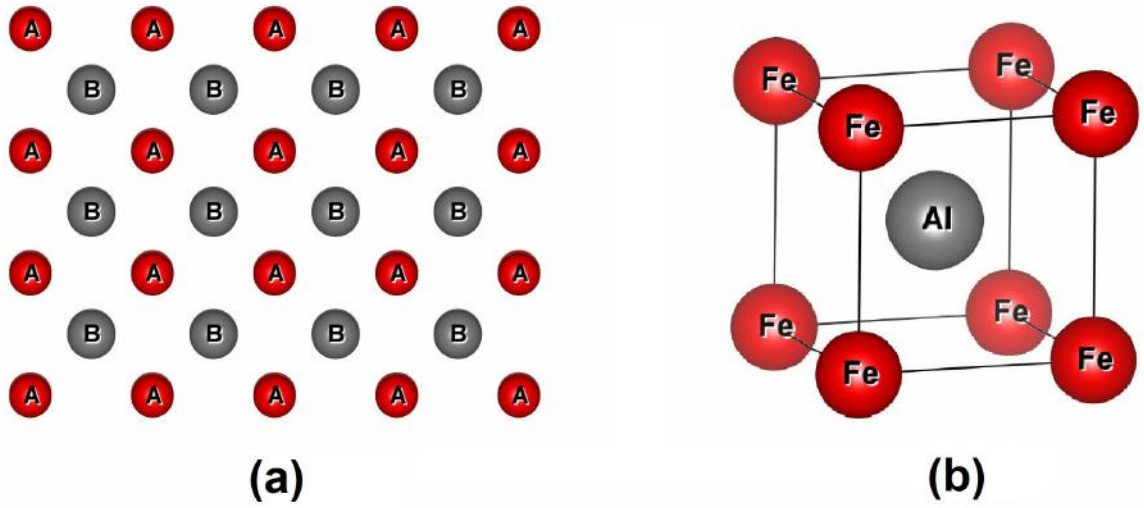

Figure 1.1: Examples of ordered alloys: (a) ordered arrangement of the constituent atoms in an *AB* alloy and (b) cubic B2 FeAl alloy.

In substitutional type disordered alloys the constituent atomic species randomly occupy the lattice sites [3–5]. Whether a lattice site $\mathbf{R}_i$ is occupied by a certain type of chemical species cannot be told with certainty. The lattice sites are occupied by the constituent atomic species with probability $\mathrm{Pr}(\mathbf{R}_i)$ equal to their concentration in bulk. The translational symmetry of the system disappears and can only be restored in terms of statistical occupancy of the atoms on the lattice sites. The previous example

of ordered *AB* alloy will turn into a substitutional type disordered alloy if we consider $\mathrm{Pr}_A(\mathbf{R}_i) = \mathrm{Pr}_B(\mathbf{R}_i) = 0.5$ for both the integer and *half*-integer values of N_1, N_2, N_3. This is shown in Fig. 1.2(a). Fig. 1.2(b) shows the crystal structure of A2 FeAl which is a substitutional type disordered alloy. In many cases, the low temperature ordered phase of an alloy transforms into a substitutional type disordered alloy at higher temperatures which constitute an intriguing topic known as *order-disorder* transformation [3–5]. Instead of the whole lattice, the substitutional disorder could also occur in selective sublattices of the system such as in Heusler alloys.

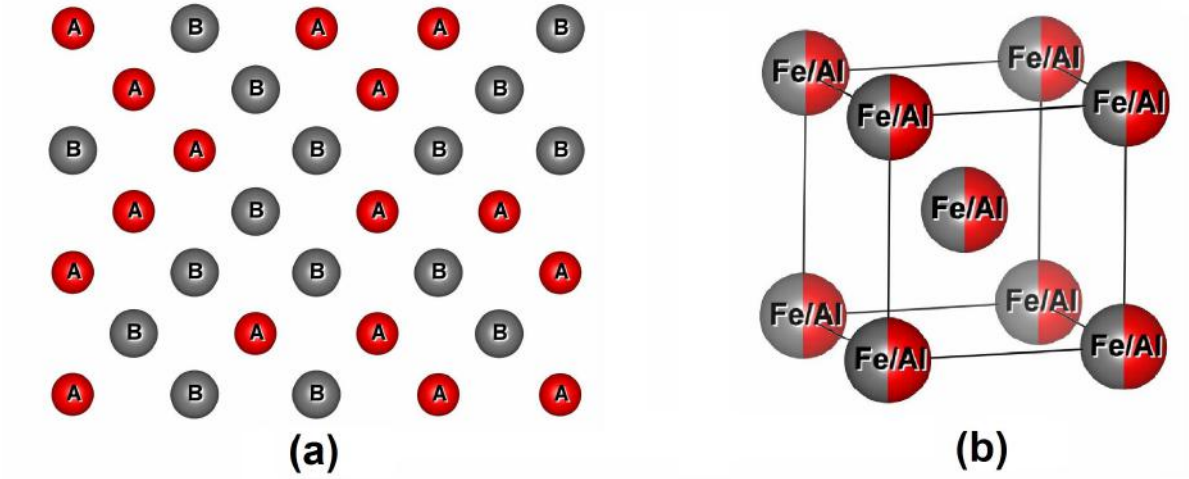

Figure 1.2: Examples of substitutional type disordered alloys: (a) a random arrangement of the constituent atoms in a substitutionally disordered *AB* alloy and (b) cubic A2 FeAl alloy.

The substitutional disorder is prevalent when the constituent atomic species have approximately the same size. However, when the size of the constituent atomic species differs largely ($\geq 15\%$) from each other, the smaller atoms randomly occupy the interstitial positions of the lattice. Such alloys are known as interstitial alloys [6] and an example is shown in Fig. 1.3. Steel is one of the best-known examples where smaller carbon atoms occupy the interstitial positions.

The alloy categories so far discussed are crystalline in nature and have a regular lattice. However, in amorphous alloys [7], even the underlying lattice disappears. The constituent atomic species randomly occupy the positions in the crystal (an example

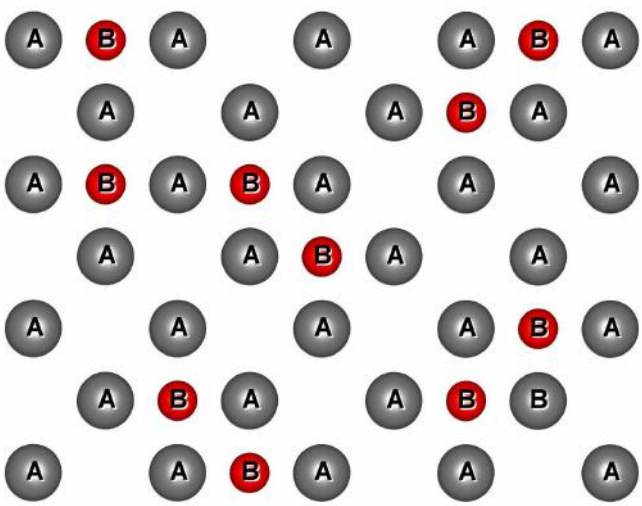

Figure 1.3: An example of the arrangement of the constituent atoms in an interstitial *AB* alloy. The smaller *B* atoms are randomly occupying the interstitial positions of the lattice.

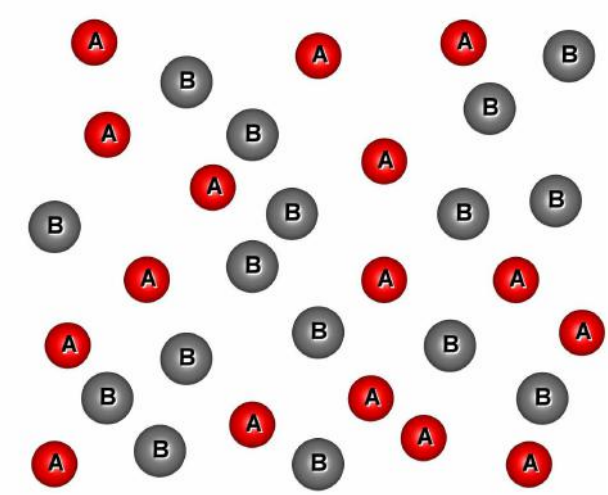

Figure 1.4: An example of the arrangement of the constituent atoms in an amorphous *AB* alloy.

for *AB* alloy is shown in Fig. 1.4) and do not form any type of periodic arrangements. These alloys are non-crystalline and also known as metallic glass. Although perfect randomness in site positions and atomic occupations are expected for an amorphous alloy, in practical situations nearest-neighbour correlations often exist in these alloys.

1.2 Substitutional disorder: short-range ordering and clustering

The substitutional disorder is one of the most common forms of disorder in alloys. Many common alloys such as brass, bronze fall into this category. In these alloys, the constituent atomic species are arranged in a completely random fashion so that the occupational probability $\Pr(\mathbf{R}_i)$ at any lattice site $\mathbf{R}_i$ is same for a type of atomic species and the nearest neighbor environment of any lattice site $\mathbf{R}_i$ is identical throughout the whole system. However, in real alloys, this complete randomness in occupancy is rarely found. To some extent, local correlation always exists among the constituent atomic species which gives rise to atomic ordering in short length scale. Two different cases arise in such situations: when the same type of atomic species tends to occupy the nearest neighbour sites the situation is called clustering (shown in Fig. 1.5) and when another type of atomic species tend to populate the nearest neighbor environments, the situation is called short-range ordering (SRO) (shown in Fig. 1.6).

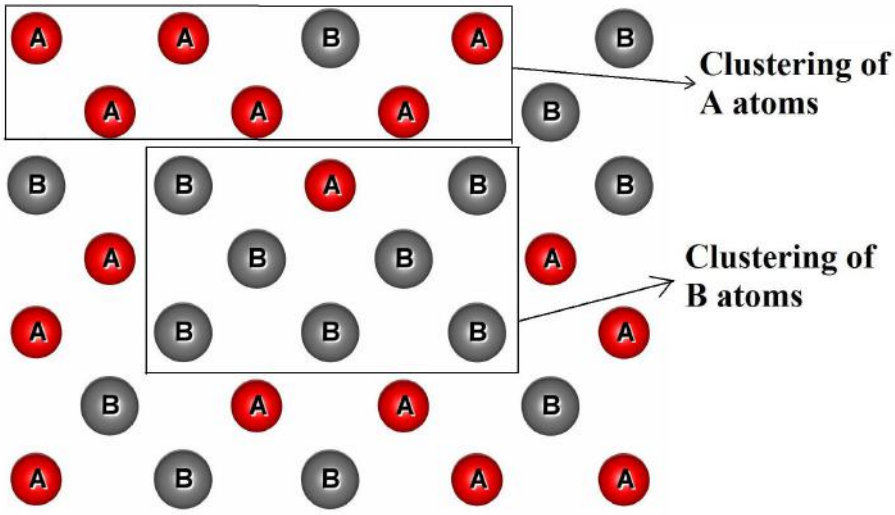

Figure 1.5: A depiction of the arrangement of the constituent atoms in the situation of clustering in an *AB* alloy.

The situation of short-range ordering and clustering can be classified in terms

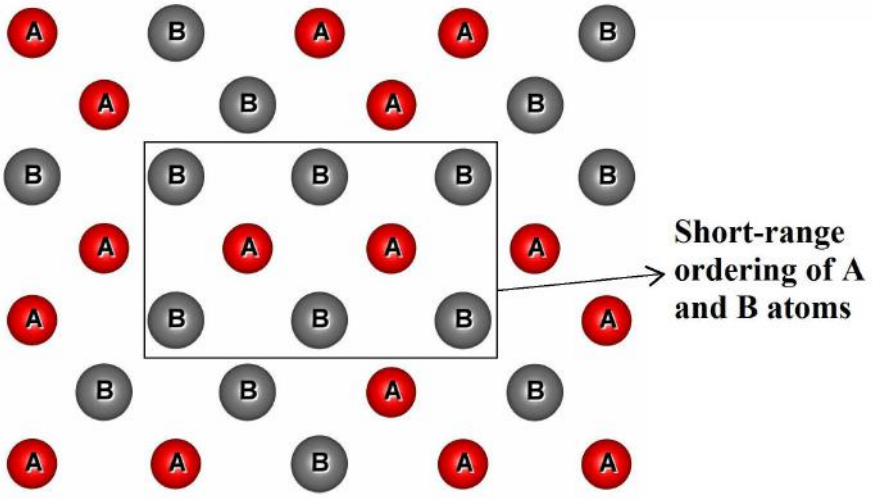

Figure 1.6: A depiction of the arrangement of the constituent atoms in the situation of short-range ordering in an *AB* alloy.

of chemical pair exchange energy $E^{(p)}$, the energy required to place an atom in the nearest neighbor environment of another atom. For a binary *AB* alloy $E^{(p)}_{AA}$, $E^{(p)}_{BB}$ and $E^{(p)}_{AB}$ are respectively the pair exchange energies between *AA*, *BB* and *AB* pairs. Short-range ordering occurs when $\Delta E^{(p)}(= E^{(p)}_{AB} - \frac{1}{2}\{E^{(p)}_{AA} + E^{(p)}_{BB}\}) < 0$, whereas clustering occurs when $\Delta E^{(p)} > 0$.

1.2.1 Warren-Cowley order parameter

Warren-Cowley order parameter, α, describes the atomic ordering in the short length scale and differentiates between short-range ordering and clustering phenomena. The order parameter α is given by [8, 9]:

$$\alpha = 1 - \frac{\mathrm{Pr}_{AB}}{c_B} = 1 - \frac{\mathrm{Pr}_{BA}}{c_A} \tag{1.1}$$

where $\mathrm{Pr}_{AB}(\mathrm{Pr}_{BA})$ is the probability of finding a *B(A)* atom in the nearest neighbor of an *A(B)* atom and c_A, c_B are respectively the concentrations of *A* and *B* atoms in the system ($\mathrm{Pr}_{AB} + \mathrm{Pr}_{BA} = 1$ and $c_A + c_B = 1$). Now the following cases can be obtained from Eq. 1.1:

(i) $\alpha = 0$ sets $\mathrm{Pr}_{AB} = c_B$ or $\mathrm{Pr}_{BA} = c_A$, then the system is perfectly disordered. This corresponds to the case $\Delta E^{(p)} = 0$ in terms of the pair exchange energy description.

(ii) $\alpha < 0$ means $\mathrm{Pr}_{AB} > c_B$ or $\mathrm{Pr}_{BA} > c_A$, then short-range ordering sets in and the situation corresponds to $\Delta E^{(p)} < 0$.

(iii) $\alpha > 0$ means $\mathrm{Pr}_{AB} < c_B$ or $\mathrm{Pr}_{BA} < c_A$, then clustering of like atoms occur and the situation is equivalent to $\Delta E^{(p)} > 0$.

The above nearest neighbor description of Warren-Cowley short-range order parameter can extended for any i-th shell neighbor:

$$\alpha^i = 1 - \frac{\mathrm{Pr}^i_{AB}}{c_B} = 1 - \frac{\mathrm{Pr}^i_{BA}}{c_A} \tag{1.2}$$

where $\mathrm{Pr}^i_{AB}(P^i_{BA})$ is the probability of finding a *B(A)* in the i-th coordination shell around an *A(B)* atom.

1.3 Some novel phenomena in magnetic alloys

1.3.1 Order-Disorder transformations

The phenomenon of *order-disorder* transition, also known as *solid-solid* transition, is a century old subject and still continues to be an important research area because it provides insight into alloy formations and their stabilities which are important aspects of metallurgy. In the early developments of metallurgy, it was thought that the constituent atomic species in an alloy always randomly occupy the lattice sites and forms substitutional or interstitial alloys. However, with the advances in X-ray crystallography, researchers found that the constituent atomic species can occupy the lattice sites in an orderly fashion too and thereby form an ordered alloy. With the increase in temperature, some of these ordered alloys were found to transform into a substitutionally

disordered phase at a characteristic temperature T_C similar to ferro- to para-magnetic transitions. This type of transformation between two solid phases constitutes the subject of *order-disorder* or *solid-solid* transition [5].

The *order-disorder* transformation in alloys is mainly controlled by two competing parameters: $\Delta E^{(p)}$ and E_{config}, the configurational energy of the system [3, 4]. E_{config} is determined by the number ways in which the constituent atomic species can be arranged and is a measure of disorder in the system. Configurational entropy is given by $S_{config} = k_B \ln\Omega$, where Ω is the number accessible state of the system at a given energy. At absolute zero temperature, the system tries to form an ordered arrangement dictated by $\Delta E^{(p)}$ so that the internal energy of the system is minimum. With increasing temperature atom exchange between different lattice sites increases and in that process, some atoms get located on a wrong sublattice. This occurs due to the fact that Ω increases with temperature and consequently E_{config} also increases. When the contribution of E_{config} dominates over the internal energy of the system, the system transforms from the ordered state into a disordered phase.

The arrangement of the atomic species in the ordered state can be expressed through a long-range order parameter ξ given by:

$$\xi = \frac{\mathrm{Pr}_A - c_A}{1 - c_A} = \frac{\mathrm{Pr}_B - c_B}{1 - c_B} \tag{1.3}$$

where Pr_A and Pr_B are respectively the probabilities of A and B atoms occupying their right lattice (sublattice) sites.

ξ can decrease continuously with increasing temperature and becomes zero at the transition temperature (as shown in Fig, 1.7(a)). This is a second order phase transformation where disordering takes place gradually over a range of temperature such as $\beta' \rightarrow \beta$ transformation in brass [3]. However, it is also possible that ξ drops abruptly to zero at the transition temperature (as shown in Fig. 1.7(b)) such as in

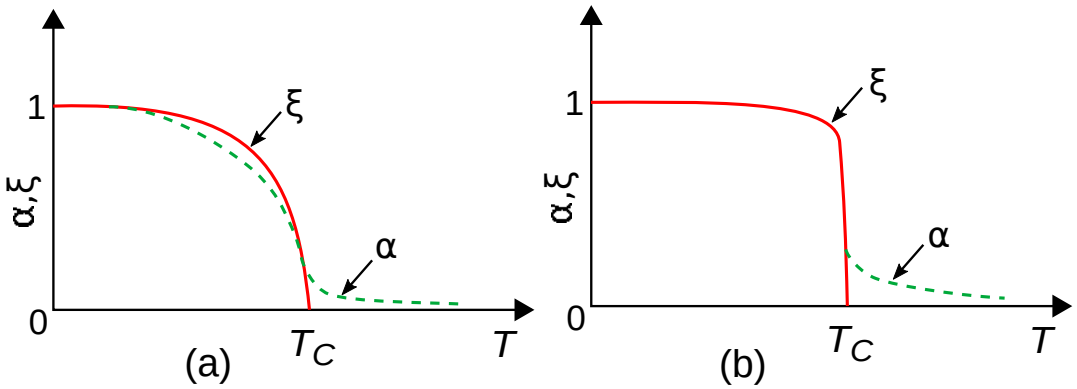

Figure 1.7: The variation of α and ξ (schematic) for different types of order-disorder transition: (a) second-order transition and (b) first-order transition. T_C is the *order-disorder* transition temperature.

Cu_3Au which is a first order phase transition [3, 5, 8].

Although α and ξ provide an equivalent description of atomic arrangement, they are intrinsically different. ξ ensures that a translational symmetry exists throughout the whole system whereas α governs only the local atomic arrangement. Their values are identical only in two specific cases: (1) if $\alpha = 0$ then we must have $\xi = 0$, and (2) when $\xi = 1$ we must have $\alpha = 1$. As can be seen from Figs. 1.7(a)–(b), even when there is no long-range order is present, the short-range order can still persist in the system.

1.3.2 Electron localization

Resistivity (ρ) of metals and alloys is controlled by elastic scattering of electrons from disorder and defects present in the lattice, and inelastic scattering processes, such as electron-phonon scattering, spin-orbit scattering or scattering from single impurity spin or collective excitations of the spin system. The rate of inelastic scattering decreases as temperature decreases and can be neglected at very low temperature in the leading order of approximation. Then resistivity at very low temperature is dominated by elastic scattering of electrons from defects and disorder present in the system which also determines the lower limit of resistivity. According to classical theory, electronic

conductivity (σ) is directly proportional to the electrons mean free path ℓ, the average distance electrons travel between two successive scattering events, and is given by Drude's formula:

$$\sigma = \frac{ne^2\tau}{m} \tag{1.4}$$

where e and m are respectively the charge and mass of electron, n is the density of free electrons and τ ($= \ell v$, where v is the electrons average velocity) is the mean free time. With increasing disorder, ℓ decreases which consequently causes the electronic conductivity σ to decrease and the motion of electrons become more of diffusive in nature rather than ballistic. When $\ell \sim a$, where a is the inter-atomic spacing, the electronic conductivity reaches the minimum value (σ_{min}) which is known as Mott-Ioffe-Regel limit [10–13]. However, P. W. Anderson showed that beyond a critical amount of disorder scattering electronic conductivity vanishes to zero rather than go to a finite minimum and the material turns into an insulator [14]. He showed that disorder induced fluctuations can trap electrons so that electron diffusions stop completely. This phenomenon is known as Anderson localization [15]. The presence of disorder in the system causes fluctuation in the site energies. As a consequence, the spatially nearby orbitals, the wave functions of which can overlap significantly, are well separated in energy so that admixture between different orbitals are very small and the orbitals, which are close in energy, can be found only at a large spatial distance so that their overlap is exponentially small. This causes the electrons to localize in their respective sites.

In a metallic state, electronic wave functions are extended throughout the system, whereas they are exponentially localized in the Anderson insulator. At a given energy, electronic states are either all localized or all remain in the extended state in a disordered medium. N. F. Mott introduced the concept of mobility edge [16–18], an energy level that separates the localized and extended states. Metallic behavior prevails when the Fermi level lies in the extended region, whereas the material turns into an insulator when the Fermi energy lies in the localized region. The scaling theory of local-

ization [19] shows that the conductivity near the mobility edge depends on the system size and provides a dimensionless scale parameter g that governs this size dependence following the equation:

$$\beta[g(L)] = \frac{d\ \ln(g)}{d\ \ln(L)} \tag{1.5}$$

where L and d are respectively the size and dimensionality of the system. Scaling theory predicts that all electronic states are localized in 1D and 2D systems for any arbitrary amount of disorder and therefore, no true metal-insulator transition exists there. However, in 3D metal to insulator transition occurs when the amount of disorder exceeds a critical amount.

The effect of this electron localization is felt even deep inside the metallic region (i.e., when disorder is weak so that $k_F\ell >> 1$ where k_F is the Fermi wave vector) which is known as weak localization (WL) or quantum interference (QI) effect and is regarded as a precursor phenomenon to Anderson localization [20–24]. The weak localization phenomenon can be understood in terms of the wave nature of electrons and coherent backscattering. In a disordered medium, electron undergoes multiple scatterings from a scattering center i.e., electron returns to its primary scattering center after a series of intermediate elastic scatterings from the nearby scattering points. Constructive quantum interference between these coherent, counter-propagating electron waves traversing a closed loop enhances the probability of backscattering. For the interference effect to take place, the condition $\tau_\phi >> \tau$, where τ_ϕ is the average time over which the phase coherence of electron waves is retained and electron diffuses over a length $L_\phi = \sqrt{D\tau_\phi}$ with a diffusion constant D, must be satisfied.

The weak localization effect decreases the conductivity of a material. The contribution of weak localization effect to conductivity is temperature dependent given by the following expression [24]:

$$\Delta\sigma_{WL} = \frac{e^2}{\hbar\pi^3 a} T^{p/2} \tag{1.6}$$

where the value of the index p depends on the nature of inelastic scattering process dominating the given temperature range.

We so far treated the electrons as non-interacting particles and neglected the electron-electron interaction effects. In normal metals and alloys, Coulomb field of electron-electron interaction is screened by the fast moving conduction electrons. However, as disorder increases and electron localization sets in, the slow diffusive motion of electrons fails in completely screening the Coulomb field [25]. This weakened screening results in the enhancement of effective electron-electron interaction strength. The enhanced electron-electron interaction (EEI) causes a further correction in conductivity, given by [24]:

$$\Delta\sigma_{EEI}(T) = \frac{e^2}{4\pi^2\hbar}\left(\frac{1.294}{\sqrt{2}}\right)\left(\frac{4}{3} - \frac{3}{2}\tilde{F}_\sigma\right)\sqrt{\frac{k_B T}{\hbar D}} \tag{1.7}$$

where $\tilde{F}_\sigma$ is the screening factor for the Coulomb interaction and k_B is the Boltzmann constant.

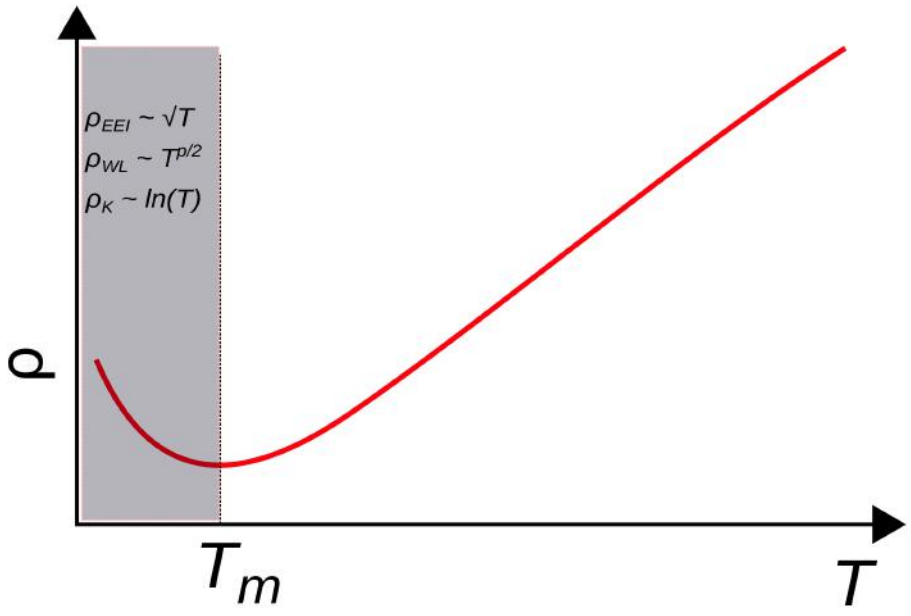

Figure 1.8: (schematic) Resistivity minimum due to variety of reasons, such as weak localization (ρ_{WL}), enhanced electron-electron interactions (ρ_{EEI}), Kondo effect (ρ_K) etc. T_m is the temperature at which resistivity minimum occurs and the index p in ρ_{WL} is explained in the text in Sec. 1.3.2.

Any inelastic scattering of electrons results in the destruction of the phase co-

herence of electron waves. With increasing temperature, the rate of inelastic scattering increases. Therefore, the weak localization and enhanced electron-electron effects die out and the classical Boltzmann transport behavior is restored. The competition of weak localization and enhanced electron-electron interactions with the inelastic scattering processes produces a minimum in the temperature dependence of resistivity as the former effects cause the resistivity to increase while the latter cause the resistivity to decrease with the lowering of temperature. A schematic of such resistivity minimum is shown in Fig. 1.8.

1.3.3 Spin glass

The high temperature phase of a magnetic system is paramagnetic where thermal fluctuations of the spin system ensure their random orientations of the spins. With the lowering of temperature thermal fluctuations of the spin system dies out and below a characteristic transition temperature all spins in the system spontaneously align themselves establishing a long-range magnetic order. Depending on the alignment of the adjacent spins, these are known as ferro-, ferri- or antiferro-magnetic ordering. However, when magnetic properties of some noble metals (e.g., Au, Cu) containing a small amount of magnetic atoms (e.g., Fe, Mn) were closely studied, another exciting magnetic phase, called spin glass was discovered [26–31]. Instead of establishing a long-range magnetic order, spins were found to be frozen into random orientations below a characteristic temperature known as spin freezing temperature T_f or spin glass transition temperature T_{sg}. The time average of a spin $\langle S_i \rangle_t \neq 0$ when observed for a long time, however $\frac{1}{N}\sum_i \langle S_i \rangle_t exp(i\mathbf{k}\cdot\mathbf{R}_i) = 0$ for $N \to \infty$ where $\mathbf{k}$ is the wave vector [28]. Below T_{sg}, the frozen-in magnetic state was found to be highly irreversible and metastable. For any magnetic perturbation to the system below T_{sg}, spins were found to be relaxing very slowly for a long time, some longer than any macroscopic time scale. Such a slow relaxation of the randomly oriented frozen-in spin system is analogous to

the structural glasses where the constituent atoms are randomly positioned and frozen into a metastable state when rapidly cooled through a glass transition.

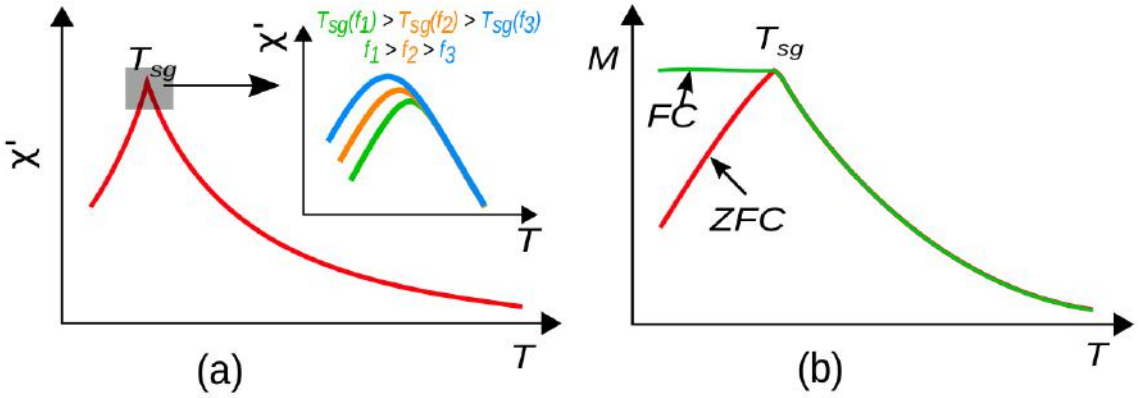

Figure 1.9: Schematics of (a) the temperature dependence of ac susceptibility and its frequency dependence, and (b) the temperature variations of ZFC and FC magnetizations. χ' is the real part of ac susceptibility and f_i's are the frequency of the ac field.

The signature of spin freezing can be observed in a variety of measurements. Low field ac magnetic susceptibility is one of the most reliable and powerful methods of probing a spin glass phase. At the spin freezing temperature T_{sg}, low field ac susceptibility shows a cusp (a schematic variation is shown in Fig. 1.9(a)) and the cusp is very sensitive to the frequency and strength of the applied field. This cusp in low field ac susceptibility shifts to lower temperatures as the frequency of the ac field decreases (inset of Fig. 1.9(a) shows a schematic variation) and this frequency dependence occurs even at very low frequencies ($\sim$ Hz). The long-range ordered magnetic states, ferromagnet, and antiferromagnet, also show frequency dependence of their respective transition temperature T_C and T_N but only at very high frequencies ($\sim$ MHz or $\sim$ GHz). Application of a small external field H ($k_B T_f \geq \mu_{eff} H$) causes smearing of the cusp. This peculiar field and frequency dependence of the cusp in low field ac susceptibility is a universal feature of the spin glass systems. The temperature dependence of dc magnetization also displays the signature of spin freezing. The zero field cooled (ZFC) (magnetization is measured in the warming cycle after cooling the system below T_{sg} without applying any external magnetic field) and field cooled (FC) (magnetization is

measured in the warming cycle after cooling the system below T_{sg} in presence of an applied magnetic field) magnetizations bifurcate below T_{sg} in spin glasses (a schematic variation is shown in Fig. 1.9(b)). The remanence magnetization between ZFC and FC states also differ in their nature of saturation. Another distinctive property of spin glass state is that when external magnetic perturbation changes, spins relax very slowly towards equilibrium and depends on the time (called aging time t_w) of how long it was in a particular (T,H) state before the perturbation changed. This slow relaxation along with the ageing and history dependences of field cycling is another universal feature of the spin glass systems. Apart from the ac susceptibility and dc magnetization measurements, a distinct signature of spin glass state can also be observed in μSR, Hall Effect, and Neutron diffraction.

The spin glass phase was initially found in the dilute noble-metal magnetic alloys which are now known as canonical spin glasses. Later, the occurrence of spin glass phase was found in other type of materials such as insulating magnetic systems (one of the prototype spin glass $Eu_xSr_{1-x}S$ is a magnetic insulator), concentrated magnetic alloys, frustrated magnetic systems etc. A multitude of theoretical and experimental investigations found that the essential ingredients needed to form spin glass phase are the simultaneous presence of magnetic frustration and disorder [26, 29]. Magnetic frustration arises when all the magnetic interactions in the system cannot be satisfied simultaneously. Magnetic frustration could arise from the presence of antiferromagnetic interaction in the system for purely geometrical reasons or when a mixture of ferro- and antiferro-magnetic couplings are present in such a way that all of them cannot be satisfied simultaneously. Such frustration results in a multi-degenerate ground state of the system. However, frustration alone cannot create a spin glass phase [26]. The disorder must be present along with the magnetic frustration. The disorder could arise from the random positioning of impurity spins or the randomness in magnetic exchange couplings. In dilute magnetic alloys, magnetic impurities are randomly dis-

tributed in the system and have localized spins which interact among them via RKKY (Ruderman–Kittel–Kasuya–Yosida [32–34]) interaction $J_{RKKY}(r) \sim \frac{Cos(2k_F r+\phi)}{(k_F r)^3}$ where k_F is the Fermi wave vector and ϕ is a constant. J_{RKKY} could be positive as well as negative depending on the positioning of the impurity atoms. The random distribution of impurity spins and the oscillatory nature of J_{RKKY} create frustration in the system which leads to the spin glass phase at low temperature.

The behaviors of the low field ac susceptibility and its fairly universal nature in a diverse range of spin glass materials, from metal to insulator and crystalline to amorphous, were not explainable within the existing theories and created a surge in the theoretical research. In the model proposed by Edward and Anderson [35] (known as *EA* model), the Hamiltonian is given by:

$$\mathscr{H} = \sum_{ij} J_{ij} \boldsymbol{S}_i \cdot \boldsymbol{S}_j - \sum_i \boldsymbol{H}_i \cdot \boldsymbol{S}_i \tag{1.8}$$

where $\boldsymbol{S}_i$ and $\boldsymbol{S}_j$ are respectively the spins situated at the sites i and j separated by a distance r_{ij} and are coupled by the magnetic exchange interaction $J_{ij}(r_{ij})$. The disorder has been introduced in the exchange coupling J_{ij} by a Gaussian distribution of J_{ij} as:

$$\Pr(J_{ij}) = \frac{1}{\sqrt{2\pi\Delta^2}} exp\left(-\frac{J_{ij}^2}{2\Delta^2}\right) \tag{1.9}$$

The order parameter of the system has been assigned to:

$$q_{EA} = \langle \langle \boldsymbol{S}_i \rangle_T^2 \rangle_C \tag{1.10}$$

where $\langle \cdots \rangle_T$ and $\langle \cdots \rangle_C$ represent thermal and configurational averages respectively. Although EA model was successful in reproducing the cusp in ac susceptibility, it has several drawbacks which prompted the development of other models such as Sherrington-Kirkpatrick (SK) model, Replica symmetry breaking etc. [28]. The realization that spin

glasses closely resemble the problems in other areas of science (e.g., complex systems, neural networks, non-equilibrium systems) attracted researchers from a diverse range of field such as mathematics, biology, statistics for example. The spin glass problem also created a surge in numerical methods and computer simulations.

1.3.4 Kondo effect

Kondo effect [36–39], the occurrence of resistivity minimum in metal and alloys in presence of a small amount of magnetic impurity, was one of the perplexing problems of the last century and continues to remain an active area of research. In normal metal and alloys, the rate of inelastic scattering of electrons decreases as the temperature decreases, and therefore resistivity decreases with the lowering of temperature. However, in multiple cases, it was observed that at low temperature resistivity of some metals and alloys suddenly start to increase with the lowering of temperature below a characteristic temperature and the magnitude of the increment increases as the concentration of magnetic impurities present in the system increases. Later, Sarachik et al. [40] showed that this resistivity increment occurs only when the impurities are magnetic in nature. Other important aspects observed in those studies were that the resistivity increment varies logarithmically with temperature and tends to saturate at further lower temperatures along with the disappearance of the magnetic moments of the impurity atoms. Using perturbation theory in the second Born-approximation, Jun Kondo showed that the scattering of conduction electrons from localized spin impurities is the origin of logarithmic increase of resistivity and occurs only when the impurity spins are antiferromagnetically exchange coupled with the conduction electron cloud [39]. The temperature range where Kondo-scattering becomes effective is given by Kondo temperature T_K:

$$T_K \sim \mathscr{D} e^{-\frac{1}{2|J|N(0)}} \tag{1.11}$$

where $\mathscr{D}$ is the width of the conduction band, $N(0)$ is the density of state of electrons in the conduction band, and J is the exchange interaction between the impurity spin and conduction electron cloud. Resistivity due to Kondo-scattering is given by:

$$\rho_K(T) \sim Jc\rho_0 \ln\left(\frac{k_B T}{\mathscr{D}}\right) \tag{1.12}$$

where c is the concentration of magnetic impurities. The original derivation of $\rho_K(T)$ by Kondo had logarithmic divergence which predicted that resistivity becomes infinite as $T \to 0$. Later, this divergence was removed from the temperature dependence of Kondo resistivity. These investigations showed that the coupling between the spin impurities and conduction electrons cloud gets stronger as the temperature decreases so that the perturbative approach breaks down and Kondo's result is correct only at temperatures above T_K. With the lowering of temperature below T_K, the impurity spins are gradually screened out by spins of the conduction electrons and this screening effect leads to the observed deviation of magnetic susceptibility from Curie-Weiss behavior and the tendency of resistivity towards a saturation. Analytical expression of Kondo resistivity considering such screening of impurity magnetic moments is given by [37, 41]:

$$\rho_K(T) = \frac{2\pi c}{ne^2 k_F}\left[1 - \frac{\ln(T/T_K)}{\{\ln^2(T/T_K) + S(S+1)\pi^2\}^{1/2}}\right] \tag{1.13}$$

where S is the spin of the local atomic magnetic moment and n is the electron density.

1.4 Overview of the thesis

Magnetic alloys continue to be a fascinating area of research for their numerous functional properties as well as for understanding the vast number of novel physical phenomena that occur in these alloys. Improved device fabrication techniques enable us to employ materials in applications that wouldn't have been possible earlier which

consequently demands a better understanding of these systems. The progress in experimental and theoretical methods combined with the advances in computer simulations enable us to explore previously inaccessible regions as well as to compare the experimental and theoretical results. With the advances in experimental techniques, for example in electron microscopy, in laboratory X-ray diffraction measurements, availability of high-energy X-ray's in synchrotrons help us to explore crystal structure and local inhomogeneities with greater accuracy. In addition, with increasing computational power combined with the advances in density functional theory (DFT), algorithms of Monte-Carlo simulations and molecular dynamics enable us in exploring material properties, phase transition and phase diagram with finer details.

The primary aspect of this thesis is to explore disorder effects in magnetic alloys and the effects of short-range ordering on the magnetic and transport properties of some disordered alloys. The various novel phenomena described in Sec. 1.3 are explored in various situations. Cubic phase of FeAl, which forms at the low and intermediate ranges of Al concentration [42–45], has been investigated extensively in this thesis. The electronic and magnetic behaviors of the solid solutions between the transition metals (e.g., Fe, Mn) and noble metals (e.g., Au, Cu) and also with metals like Al is a topic of interest for many years and many novel phenomena such as Kondo effect, spin glass have emerged from these studies. Cubic Fe-Al alloy system is one such prototype system which offers a test bed to study the dilution behavior of Fe magnetic moment with increasing TM-*d* and Al-*sp* hybridization by increasing the Al concentration in the system. Substitutionally disordered body centred cubic (BCC) solid solution of Fe and Al persists up to nearly 23 at% of Al concentration [42–45] and consequently Fe moment decreases linearly with increasing Al concentration in this concentration region [46–50]. With a further increase of Al concentration, the BCC solid solution changes to ordered arrangements of Fe and Al atoms. The BCC solid solution could be extended up to nearly 55 at% of Al concentration by different disordering methods such

as cold working and ball milling, however, Fe moment now falls faster than a simple dilution law [46–50]. In addition, a complete destruction of atomic ordering is difficult which gives rise to short-range orderings of Fe and Al atoms that strongly influences the magnetic properties and further complicates the dilution behavior. In this regard of order-disorder transformation of the cubic Fe-Al system, the change in magnetic behavior due to disordering has immense potential in practical applications. Near 40 at% of Al concentration, ordered FeAl is paramagnetic at room temperature whereas the disordered one is ferromagnetic and by controlled disordering procedures, such as with high-energy ion-irradiation, patterned magnetic media of nanometer size could be created [51, 52]. We have investigated the structural, magnetic and transport properties of this alloy system with special emphasis on the effects of short-range ordering.

The low and intermediate Al concentration ranges, where the cubic phases are formed, are the most studied compositions in Fe-Al alloy system. In the Al-rich region of the phase diagram, Fe_2Al_5, $FeAl_2$ and Fe_4Al_{13} are the stable intermetallic compounds [44, 45, 53, 54]. Out of these alloys, Fe_2Al_5 and Fe_4Al_{13} are quasicrystalline approximants. $FeAl_2$ crystallizes into a very low symmetric crystal structure (space group 2) and its unit cell comprises 19 atoms [54]. Despite containing such a large number of atoms, the atomic density in the unit cell is very low. The substitutional disorder appears in this intermetallic compound due to the random occupancy of Fe and Al atoms at some lattice sites. The presence of substitutional disorder, combined with the antiferromagnetic interactions among the Fe atoms, results in a low temperature spin glass phase [55–58]. Above the spin glass transition, another magnetic transition appears where various experimental reports contradict each other [55–58]. The temperature variation of resistivity depicts a minimum below which resistivity increases linearly with $\sqrt{T}$ [55]. Such a variation of resistivity with temperature generally arises from the quantum corrections in resistivity of disordered alloys due to weak localization and enhanced electron-electron interactions effects. However, in earlier studies these aspects were not explored

in details. In contradiction to experimental reports, DFT based electronic structure calculations indicated that $FeAl_2$ should stabilize into a $MoSi_2$ type tetragonal structure instead of the experimentally observed triclinic aP19 phase [53, 59, 60]. However, this tetragonal $FeAl_2$ has never been found in experiments. DFT based phonon calculation [53] indicate that the low atomic density of the experimentally observed triclinic aP19 phase is the reason behind its stability over the hypothetical tetragonal structure. Low atomic density results in higher vibrational entropy which stabilizes the triclinic structure at higher temperatures and subsequent lowering of temperature slows down the atomic diffusions which prevent the formation of the tetragonal structure. We investigated this intermetallic compound for its structural, magnetic and transport properties. We have also investigated the substitution of Al atoms by isoelectronic Ga atoms to explore whether that results in the stabilization of the hypothetical tetragonal phase. We also made a detailed investigation of the effects of Ga substitution on the magnetic and transport properties of $FeAl_2$.

Experimental reports [61, 62] indicate that below 10 at% of Cr concentration, the low-temperature magnetic phase of disordered $Au_{1-x}Cr_x$ alloy is a spin glass and above 15 at% of Cr concentration a long-range antiferromagnetic ordering sets in. In between these two ranges of Cr concentration, the magnetic phase is a possible mixture of spin glass and antiferromagnet. We have explored the magnetic phase diagram of this system by mean field analysis of the magnetic exchange interaction parameters calculated from first-principles theories to compare with experimental reports. Disordered $Au_{1-x}Cr_x$ alloys have face centred cubic (FCC) crystal structure and in such close-packed structures of disordered alloys with antiferromagnetic interactions, the spin configuration of the system often becomes a noncollinear type [63–68]. Therefore, we also checked the possibility of noncollinear spin configurations in this system.

The thesis is organized as follows:

I. The major instruments used for the compositional and structural characterization

of the samples are briefly described in Chapter 2. Measurement methods of various physical properties and the corresponding techniques are also discussed in this chapter. As a significant portion of this thesis deals with first-principles density functional theory (DFT) based calculations, theoretical aspects of the DFT codes used in this thesis are also briefly discussed in this chapter.

II. Chapter 3 deals with the magnetic properties of equiatomic FeAl alloy. How the presence of short-range ordering affects the magnetic state of the disordered Fe:Al alloy is explored in this chapter. The experimental results are supplemented with the magnetic properties obtained from Monte-Carlo (MC) simulations using the magnetic exchange interaction parameters calculated from first-principles theories.

III. Chapter 4 presents the magnetic and transport properties of disordered $Fe_{1-x}Al_x$ ($0.25 \leq x \leq 0.55$) alloys. The evolution of short-range ordering with composition and its effects on the lattice parameter, electrical transport, and magnetic properties are discussed. The magnetic exchange interaction parameters of these alloys obtained from first-principles calculations are also presented in this chapter. Magnetic transition temperature obtained using the calculated magnetic exchange interaction parameters in a Monte-Carlo simulation are compared with the experimental results.

IV. Chapter 5 describes the structural, magnetic, electrical transport and magneto-transport properties of $FeAl_{2-x}Ga_x$ ($0 \leq x \leq 0.5$) alloys. Effects of Ga addition on the magnetic and transport properties of $FeAl_2$ are also presented in this chapter. A novel phenomenon, antiferromagnetic transition concomitant with disorder-induced weak localization, found in these alloys is described in this chapter.

V. Chapter 6 deals with the magnetic properties of disordered $Au_{1-x}Cr_x$ ($0 \leq x \leq 0.3$) alloys. The possibility of a noncollinear spin ordering in disordered AuCr alloy is

investigated in this chapter using density functional based theories. Magnetic phase diagram of the system is constructed by mean field analysis of the magnetic exchange interaction parameters obtained from first-principles theories.

VI. Chapter 7 is the conclusion of this thesis and the future scopes are discussed in it.

2 Experimental and Theoretical Methods

2.1 Experimental methods

2.1.1 Sample preparation

2.1.1.1 Arc melting

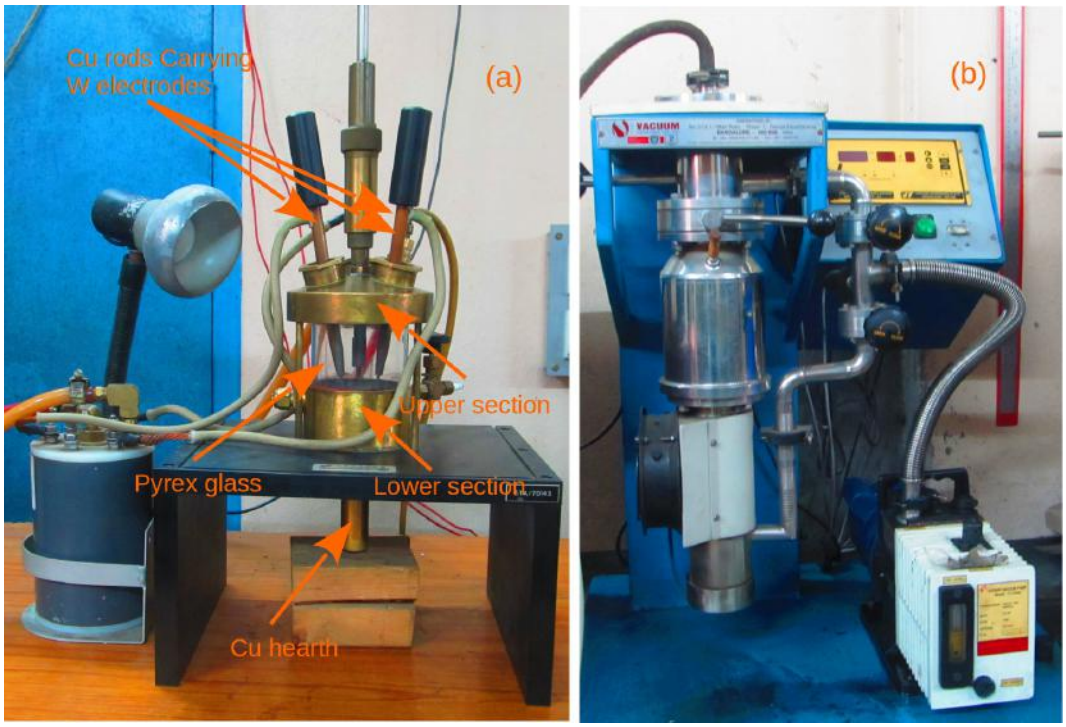

Figure 2.1: (a) The tri-arc furnace used for sample preparation, and (b) the vacuum pump used in pumping the sample chamber of the tri-arc furnace.

Bulk polycrystalline samples of the alloys studied in this thesis were prepared

by melting appropriate amounts of high purity (≥ 99.9%) constituent elements in a Centorr/Vacuum Industries™ made (model no. 5TA) tri-arc furnace (shown in Fig. 2.1(a)). The furnace is capable of reaching up to 3500 °C and the maximum current that can pass through the system is 400 A. This furnace has two main sections: (i) the lower section contains a copper hearth, and (ii) the upper section comprises three copper rods which carry three tungsten electrodes. These two sections are separated by a cylindrical pyrex glass section which acts as a window to view the melting process as well as acts as an insulating stage between the upper and lower sections. Both the upper and lower sections are cooled by running chilled water. The copper hearth carries the elements to be melted. The copper rods in the upper section of the furnace are placed through swivel balls which allow vertical as well as angular movements of the rods. The air inside the chamber was first evacuated by a rotary pump (made by Vacuum Techniques (P) Ltd.™ and shown in Fig. 2.1(b); the model can also be used as a diffusion pump, however here we used only the rotary pump option) which was followed by flushing of argon gas through the chamber. This process was repeated for 3 – 4 times. During melting, argon gas was flowed in continuously through the chamber to ensure an oxygen free environment of the chamber. High current was generated by a 3-phase transformer. Arcing was initiated by momentarily touching the tungsten tips to the copper hearth. Ingots were remelted several times by turning it over and the chamber was cooled down to room temperature before each melting.

2.1.1.2 Annealing

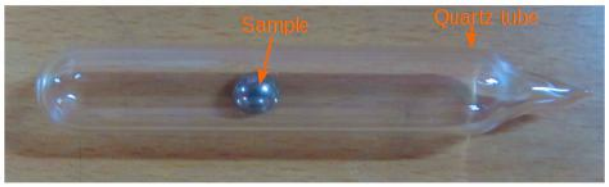

Figure 2.2: A typical quartz ampule containing arc-melted sample ingot used for annealing.

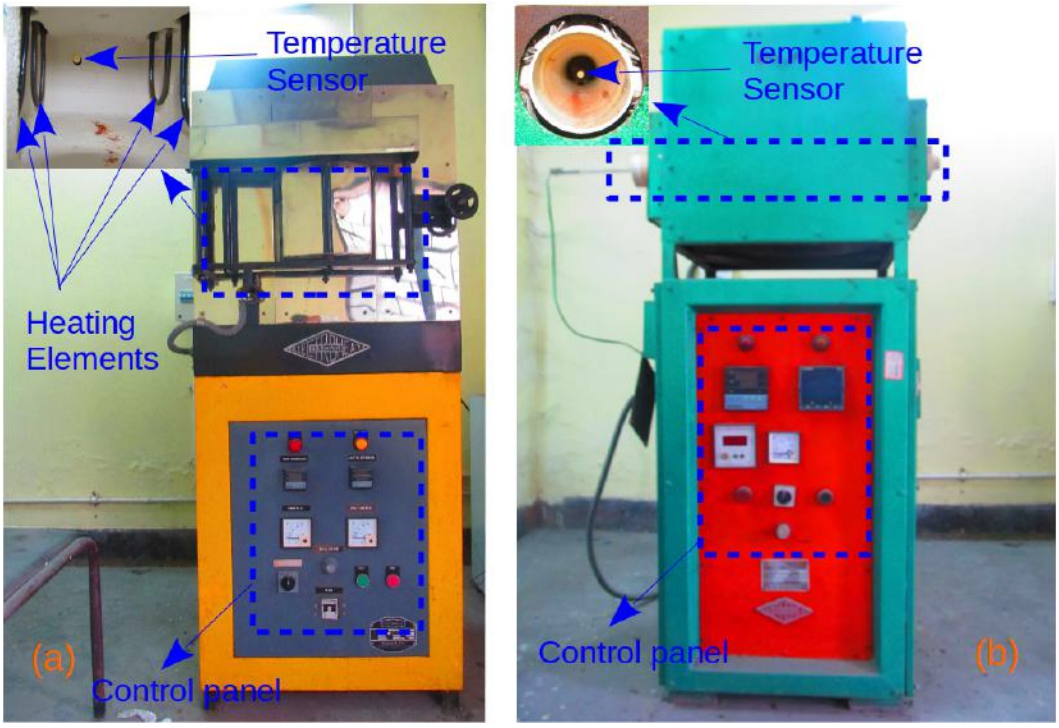

Figure 2.3: High temperature furnaces used for annealing of the samples: (a) box type furnace capable to reach temperature up to 1800 °C, (b) tubular muffler type furnace capable to reach up to temperature 1200 °C.

After the arc-melted ingots cooled down to room temperature, they were vacuum-sealed in quartz ampules. Before sealing, the quartz tubes were evacuated using the rotary pump and purged with argon gas for 3 – 4 times. A typical vacuum-sealed quartz ampule containing a sample ingot is shown in Fig. 2.2. The quartz ampules containing the ingots were then placed inside high temperature furnaces for annealing. A box type and a tubular muffler furnace (shown in Figs. 2.3(a)–(b)), both made by Naskar & Co.™, were used for annealing purposes. The box type furnace has $MoSi_2$ heating elements and the system could reach temperature up to 1800 °C. The tubular muffler furnace uses SiC heating elements and the maximum temperature range of the furnace is 1200 °C. Both the furnaces have programmable temperature controllers for controlling the annealing time as well as heating and cooling rates. After annealing, either the quartz ampule containing sample ingots were furnace cooled or quenched into liquid nitrogen. The details of this along with the details of annealing temperature and

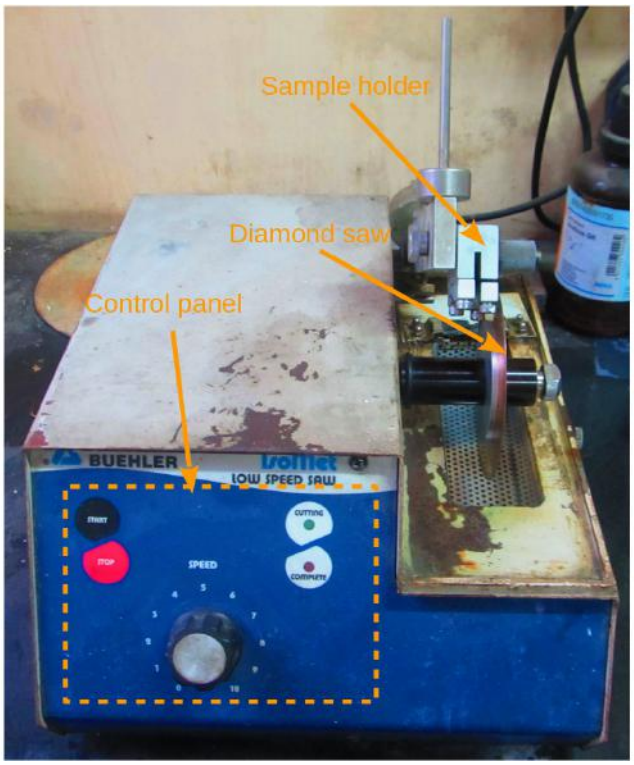

Figure 2.4: Buehler IsoMet® low speed sample cutter.

duration of the samples are given in their respective chapters. The sample ingots were then taken out of the quartz ampules and cut into various shapes and sizes according to the need of the experiments using a Buehler IsoMet® (shown in Fig. 2.4) low-speed diamond saw. A few parts of the samples were also grounded into fine powder using diamond file and mortar pestle.

2.1.2 Compositional characterization

2.1.2.1 EPMA and EDX

The compositions of the prepared ingots were checked using a wavelength dispersive (WDS) electron probe X-ray micro-analysis (EPMA) system and a scanning electron microscope (SEM) machine with energy dispersive X-ray analysis (EDX) attachment. Both these two methods are non-destructive analytical techniques and are

widely used to probe the chemical composition as well as the degree of chemical homogeneity of the metallic samples. The basic principle behind these methods is that when high-energy electrons interact with materials, characteristic X-ray is generated which is unique for each element in the periodic table [69]. For this, a high-energy ($\approx$ 20 – 30 keV) electron beam is focused on the sample surface. The penetration depth of this incident beam in metals and alloys is of the order of few microns. The incident energy excites electrons from the inner shells of the atoms and ejects them from the material which are known as *secondary electrons*. To fill the vacancies created by the secondary electrons, electrons from outer orbitals then jump to the inner shells and the difference in energy between the inner and outer shells is released in the form of X-ray. The emitted X-ray is then detected by an energy dispersive (SEM/EDX) or wavelength dispersive (WDS/EPMA) spectrometer. As each element has a unique electronic structure, the generated X-ray spectrum can be used to fingerprint the chemical elements present in a material. Apart from the secondary electrons and characteristic X-ray, backscattered electrons are also generated in the process [69]. The secondary electrons and backscattered electrons generated in the process can be used for imaging purpose of the sample surface. The imaging in SEM using secondary electrons is a widely used technique in materials science which are most useful in showing the morphology and topology of the samples. This attractive feature of SEM images come due to the large depth of field in SEM which allows for a large sample surface to be at focus at a time. The combination of higher magnification and greater depth of field makes SEM one of the most heavily used instrument in scientific research. Imaging of sample surface using the backscattered electrons is useful for illustrating contrasts in compositions in multiphase samples and phase identification. EPMA and SEM/EDX analysis were respectively carried out using Cameca^{TM} SX100 and FEI Quanta^{TM} FEG 250 instruments. The composition analysis was performed at several different spots in the sample to check for the compositional homogeneity.

2.1.3 Structural characterization

2.1.3.1 X-ray diffraction

X-ray diffraction (XRD) is the most used technique for structural characterization and phase identification of materials. All the crystalline materials have a periodic arrangement of lattice points which can be described by the Bravais lattice system. The constituent atoms of a material sit on these lattice points and form regular atomic arrangements that can be described by lattice planes and are generally indicated by Miller indices ($h\ k\ l$). When an X-ray beam falls on the material, it gets scattered at the lattice sites by the electrons of the constituent atoms. The scatterings can be both elastic and inelastic in nature. Here in x-ray diffraction, we are concerned only with the elastic scattering so that the incident and scattered waves have the same wavelength and a definite phase relationship between them. The scattering occurs in every direction, however, except for a few specific directions, waves scattered from parallel lattice planes cancel out through destructive interference. Constructive interference occurs only in the directions given by Bragg's law [70]:

$$2d_{hkl} \sin\theta = n\lambda \tag{2.1}$$

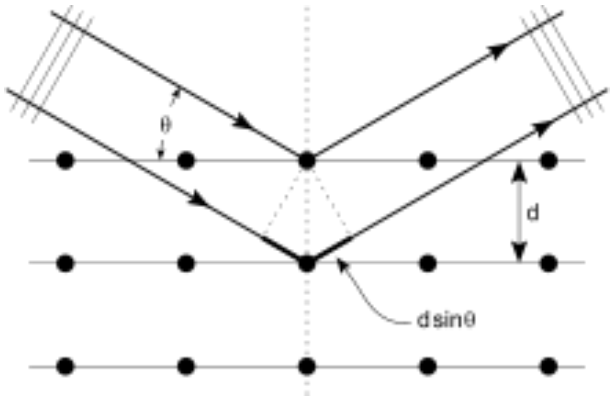

Figure 2.5: Schematic of Bragg's diffraction condition $2d_{hkl} \sin\theta = n\lambda$ from a lattice. The details is described in the text. Image source Ref. [71].

where d is the spacing between the diffracting lattice planes, θ is the angle between

the incident wave and lattice plane, λ is the wavelength of the incident X-ray and n is an integer. A schematic of the process is shown in Fig. 2.5. If the angles at which the constructive interference occur are known, then from the above relation one can get the information about lattice planes and consequently the atomic arrangement inside the material. Also, as the scattering intensity from an atom depends on its number of electrons, higher the number of electrons higher is the scattering intensity, the intensity of the XRD peaks or interference can be used to infer information about the nature of the constituent atoms occupying a particular type of lattice site [72].

We used powder specimens of the samples for XRD study at room temperature. These powdered specimens were placed in a monochromatic beam of x-ray. Each powder particle acts as a tiny crystal oriented in random directions so that the Bragg's reflection condition is satisfied for all lattice planes. We used a PANalytical X'Pert PRO powder diffractometer with Mo Kα (wavelength $\lambda = 0.71$ Å) source and a Rigaku^{TM} MiniFlex^{II} with Cu Kα (wavelength $\lambda = 1.54$ Å) source for XRD study. Ni and Zr filters were used for the Cu and Mo X-ray sources respectively to remove the Kβ lines. In the PANalytical^{TM} X'Pert PRO powder diffractometer the sample stage was fixed while both the source and the detector rotated. However, in the Rigaku MiniFlex^{II} diffractometer, the source was fixed while the sample stage and the detector rotated. The XRD pattern was obtained by scanning the 2θ angles with a scan rate of 1°– 2°/min with step size 0.02°. The collected XRD patterns were then analyzed using MAUD software [73–75].

2.1.4 Transport measurements

2.1.4.1 Resistivity measurement

The materials explored in this thesis are metallic alloys which have very low resistances ($\sim$ mΩ). We used a four probe low resistance circuit method to measure the resistivity of these materials [76]. A schematic of the method is shown in Fig. 2.6. The

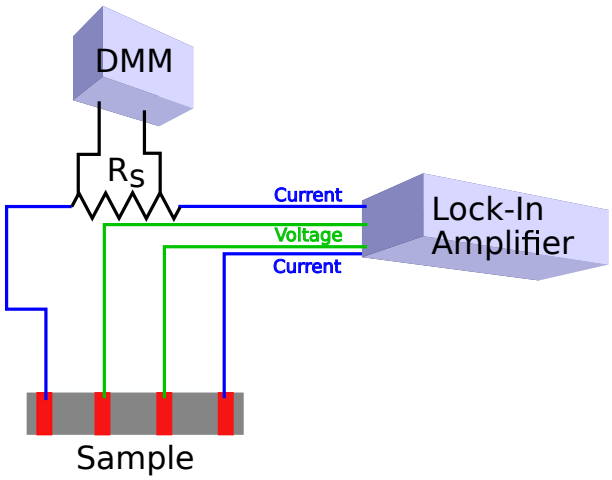

Figure 2.6: Schematic of four probe method used for resistivity measurement. R_S is the standard resistance and DMM refers to digital multimeter.

probe current was passed through the outer leads, while inner leads were used to sense the voltage drop. As negligible current passed through the voltage leads, lead and contact resistances were avoided in this method. To minimize the effects of thermoelectric effect at the contacts we used ac excitations for which polarity changed according to the frequency of the ac signal and consequently emf generated due to thermoelectric effect got canceled. As the current passing through the sample and the standard resistance is same we can write $\frac{V_{sample}}{R_{sample}} = \frac{V_{std}}{R_{std}}$ where V_{std} and V_{sample} are respectively the voltage drops across the standard resistance and the sample, R_{std} and R_{sample} are the resistances of the standard resistance and the sample. Thus by measuring V_{sample}, V_{std} and knowing R_{std} we can get the sample resistance as $R_{sample} = V_{sample} \times \frac{R_{std}}{V_{std}}$.

An ac current ($\sim$ 1 – 2 mA) at a frequency of 111.11 Hz was sourced from a lock-in amplifier through a standard resistance ($\sim$ 1 kΩ) and the voltage drop across the sense leads was detected also using the lock-in amplifier. A Stanford Research Systems 830 (SR830) digital signal processing (DSP) lock-in amplifier was used for the source of ac current and the measurement of the voltage across the sample. The voltage drop across the standard resistance was measured using a Keithly 2000 digital multimeter (DMM) again in four probe configuration. A closed cycle cryostat (CCR) from Oxford

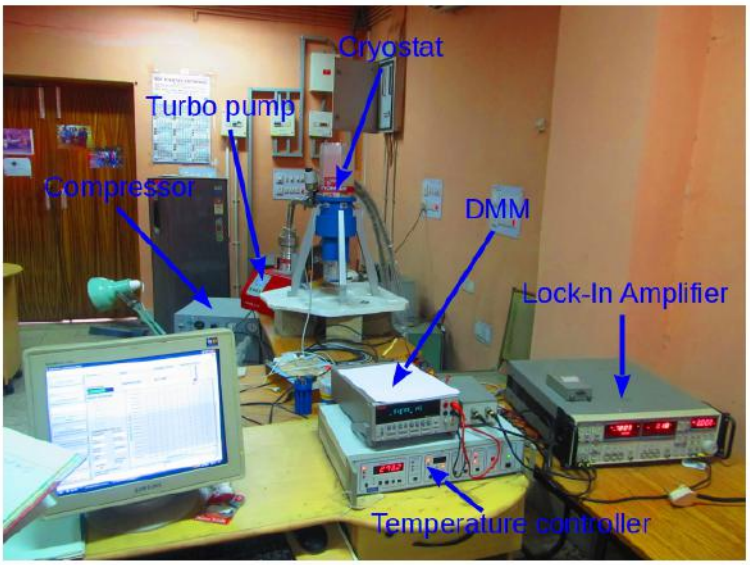

Figure 2.7: The picture of the low temperature resistivity set-up along with the measuring instruments. The details are described in the text.

Instrument™ (Optistat AC-V®) with pulsed tube refrigerator (PTR) was used to obtain the low temperature environment needed for the measurement of resistivity data at low temperature. In this system resistance could be measured in the temperature range 2.8 K – 325 K. The temperature of the sample environment was detected using Rh-Fe thermometer mounted on the low temperature stage of the cryostat and the temperature inside the cryostat was controlled by an Oxford Instrument™ ITC-503 temperature controller. The sample chamber was pumped using a turbo molecular pump from Pfeiffer Vacuum Technology™ AG which provided low pressure environment inside the sample chamber to $\leq 5 \times 10^{-5}$ mbar. The photo of the resistivity set-up is shown in Fig. 2.7. The measurements were performed by slowly heating the sample at a rate 1 K/min.

The entire set-up was connected to a computer via GPIB (GPIB: General Purpose Interface Bus) and controlled by a program developed in LabVIEW™. The front panel control and block diagram of the software developed for resistivity measurement are shown in Fig. 2.8.

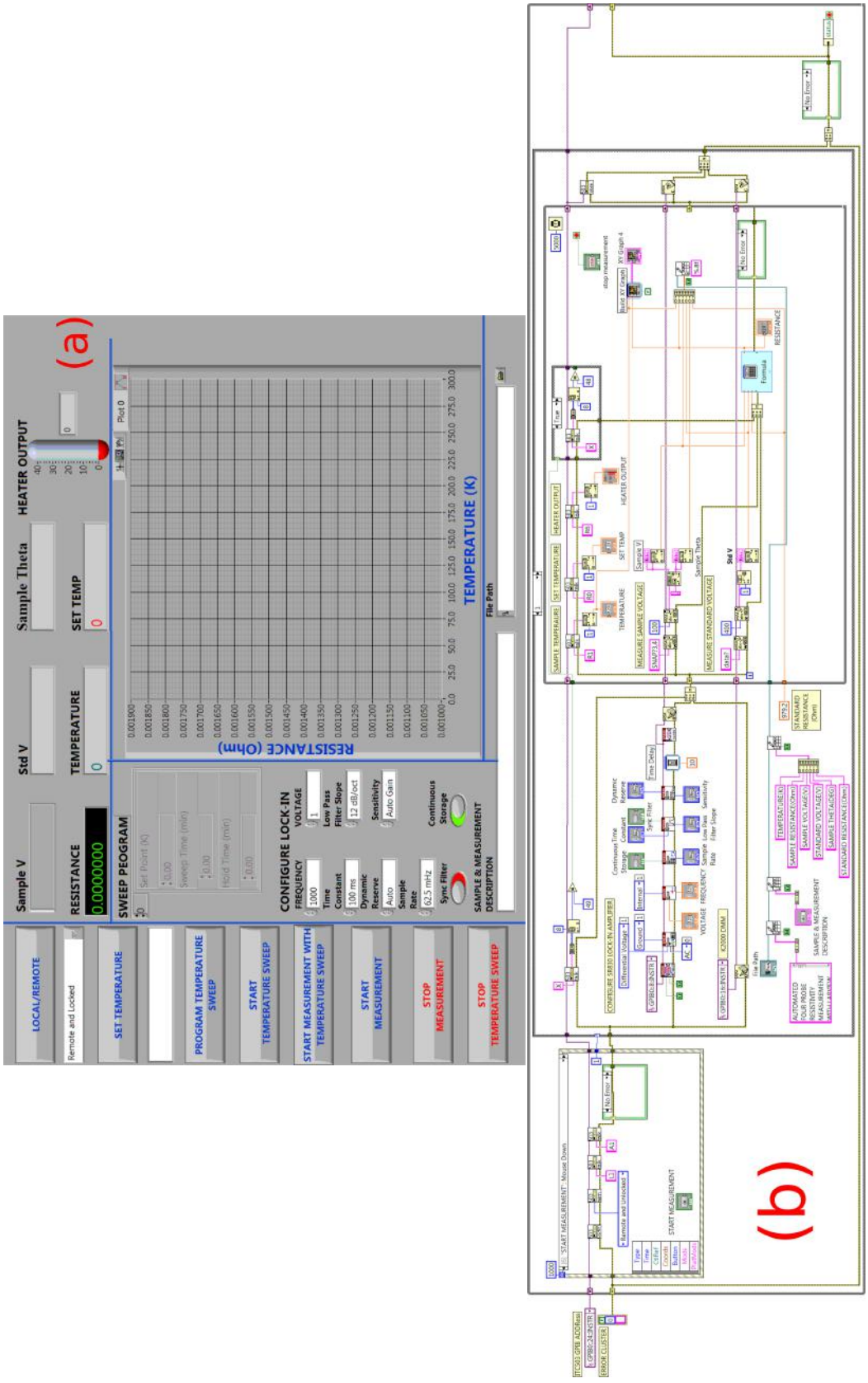

Figure 2.8: (a) Front panel view and (b) block diagram of the resistivity measurement program developed in LabVIEW.

2.1.4.2 Magnetoresistance measurement

Figure 2.9: The picture of the 10 T magnet system from Cryogenic Limited used for magnetoresistance measurements. Image source Ref. [77].

Magnetoresistances were measured using the standard four probe technique. However here dc excitation was used and to avoid the thermal emf, average data were taken by alternating the polarity of the signal. The dc current was sourced from a Keithley 2450 sourcemeter and the voltage drop across the voltage leads was measured using a Keithley 182 Sensitive Digital Voltmeter in which voltage as low as few nV can be measured reliably. These measurements were carried out using a 10 T magnet system from Cryogenic Limited™. A photo of the set-up is shown in Fig. 2.9. The current flowing through the sample was in perpendicular to the magnetic field direction. In the magnetoresistance measurements, the temperature was fixed at a particular temperature and resistance was measured by varying the magnetic field. The temperature was controlled by a Lake Shore Cryotronics™ 332 temperature controller and the stability of the temperature was better than 0.25 K i.e., $\Delta T \leq 0.25$ K.

2.1.5 DC magnetization measurements

2.1.5.1 VSM

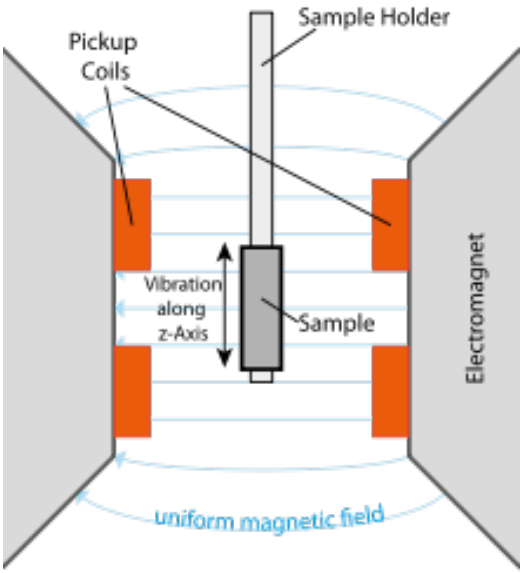

Figure 2.10: Schematic of vibrating sample magnetometer (VSM). Image source Ref. [78].

Vibrating sample magnetometer (VSM) [79] was used to measure dc magnetization of the samples as a function of temperature and magnetic field. The basic principle which this measurement relies on is the Faraday's law of induction according to which changing magnetic flux induces a voltage. Under a magnetic field H, a moment m is induced in the material. The sample to be studied is placed within suitably placed pick-up coils under an applied magnetic field which magnetizes the sample. The sample is given a vertical sinusoidal mechanical oscillation due to which magnetic flux enclosed by the pick-up coils changes as a function of time. Consequently, according to Faraday's law, this changing magnetic flux induces a voltage in the pick-up coils. The induced voltage in the pick-up coil is given by $V_{coil} = \frac{d\phi}{dt} = \frac{d\phi}{dz}\frac{dz}{dt}$ where ϕ is the magnetic flux enclosed by the pick-up coil, z is the vertical position of the sample with respect to the coil. For sinusoidal oscillation of the sample, V_{coil} is proportional to the magnetic moment of the sample and is given by $V_{coil} = KmA\omega \sin(\omega t)$ where K is the coupling

constant, m is the dc magnetic moment of the sample, $\omega = 2\pi f$ where f is the frequency of oscillation of the sample and A is the amplitude of oscillation. A schematic of a VSM system is shown in Fig. 2.10.

We used two different commercial VSM systems for magnetization measurement of the samples: (i) Lake Shore Cryotronics™ VSM and (ii) Quantum Design™ physical property measurement system® (PPMS) based VSM. The VSM system from Lake Shore Cryotronics has two different cryostats, one for low temperature measurement in the temperature range 80 K – 400 K and another one for measurement in the high temperatures in the range 300 K – 1273 K. The maximum magnetic field available in this system is 1.6 T. In the PPMS VSM system magnetization was measured in the temperature range 2 K – 300 K and in the field up to 5 T.

2.1.5.2 SQUID

The superconducting quantum interference device (SQUID) is a highly sensitive magnetometer which operates on the basis of Josephson effect and flux quantization (a magnetic flux quantum $\Phi = h/2e = 2.0678 \times 10^{-15}$ Tm^2 where h is the Plank constant and e is the electron charge). The Josephson effect [80] is an example of macroscopic quantum phenomena: when two superconductors are separated by a thin insulating layer, tunneling of Cooper pairs of electrons through the junction occur even in the absence of an applied voltage. In dc Josephson effect, a current proportional to the phase difference of the wave functions flow through the junction in absence of an externally applied voltage while in ac Josephson effect the Josephson junction oscillates with a characteristic frequency proportional to the voltage applied across the junction. SQUID based on both dc Josephson effect (dc-SQUID) and ac Josephson effect (rf-SQUID) have been made. In a dc-SQUID, a superconducting loop is interrupted by two Josephson junctions placed in parallel. When a magnetic flux is applied perpendicular to the plane of the loop, the loop responds with a current due to the quantization

of flux. The critical current and the SQUID output voltages are periodic functions of the externally applied flux. A schematic of SQUID is shown in Fig. 2.11.

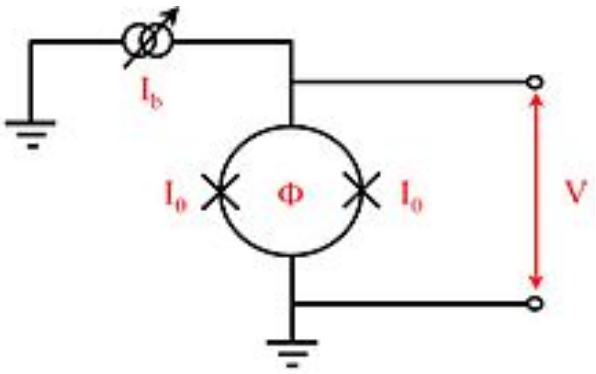

Figure 2.11: Schematic of a SQUID where I_b and I_0 are respectively the bias current and critical current, Φ is the flux threading the SQUID and V is the voltage response of that flux. Image source Ref. [81].

In this thesis Quantum Design™ magnetic property measurement system® (MPMS) SQUID was used to measure magnetization of the samples in the temperature range 2 K – 300 K and in the field range up to 7 T. Here the measurements are performed by moving the sample through superconducting detection coils. As the sample moves through the superconducting coils, the magnetic moment of the sample causes the change in magnetic flux enclosed by the pick-up coils. These superconducting pick-up coils are inductively coupled to a SQUID sensor and so the change in the signal of the pick-up coils is reflected in the SQUID output voltage. The SQUID magnetometers have sensitivity higher than that of a conventional VSM system and can be used to detect very small magnetizations in the samples that are otherwise unreliable when measured using a conventional VSM system.

2.1.6 AC susceptibility

The magnetic susceptibility χ of a material is given by $\chi = M/H$ where M is the magnetization per unit volume in presence of an applied field H [1]. In dc magnetometry described above, the sample is magnetized by a dc magnetic field and the

measured magnetizations are the equilibrium values as the sample moment remains constant during the measurement time. In ac susceptibility measurement, the sample is driven by an ac magnetic field $H_{ac} = H_a \cos(\omega t)$ where $f = \omega/2\pi$ is the frequency of the applied field. In this case, as the applied field changes with time, the moment detected in the measurement is ac moment of the sample which is time dependent and gives information about the magnetization dynamics of the sample. At low field and frequency of the applied field, the measured ac magnetization is equivalent to that one could obtain from the dc magnetic measurements. However, by varying the frequency or the applied field strength one could obtain the dynamic behavior or probe different region of the $M(H)$ curve. The slope of the $M(H)$ gives the susceptibility χ ($\chi = \frac{\partial M}{\partial H}$) and magnetization of the sample is given by:

$$M(t) = \sum H_{ac}\left(\chi_n' \cos(n\omega t) + i\chi_n'' \sin(n\omega t)\right) \tag{2.2}$$

where n represent the order of the harmonics. The real (χ_n') and imaginary (χ_n'') part of the susceptibility are then given by:

$$\chi_n' = \frac{1}{\pi H}\int_0^{2\pi} M(t)\sin(n\omega t)\mathrm{d}(\omega t) \tag{2.3}$$

and

$$\chi_n'' = \frac{1}{\pi H}\int_0^{2\pi} M(t)\cos(n\omega t)\mathrm{d}(\omega t) \tag{2.4}$$

In the dc magnetization measurements described above using VSM and SQUID, the measurements are inductive where the sample is moved relative to pick-up coils which causes the change in magnetic flux and consequently a voltage is induced in the pick-up coils which is measured. However, in ac susceptibility measurements the induced magnetization in the sample by the time varying magnetic is time dependent and thereby the induced magnetization itself causes the change in magnetic flux enclosed

by the pick-up coils. The ac susceptibilities were measured using a Quantum Design™ physical property measurement system® (PPMS) system. The measurements were carried out by applying a small ac field $H_{ac} = 100$ Oe at different frequencies in the range 100 Hz to 10000 Hz.

2.1.7 Specific heat

Specific heat of a material is defined as the amount of heat required to change the temperature of unit mass of the material by one degree. In mathematical form it can be expressed as $C = \frac{dQ}{dT}$ where dQ is the amount of heat transferred to or from the system and dT is the resulting change in temperature. In the above definition, we also need to specify the whether the pressure P or the volume V is kept constant during this temperature change and the respective specific heat quantities are known as the specific heat at constant pressure C_P and specific heat at constant volume C_V. In this thesis work, specific heat at constant pressure $C_P = \left(\frac{dQ}{dT}\right)_P$ was measured for several disordered alloys in a Quantum Design™ physical property measurement system® (PPMS) system in the temperature range 2 K – 300 K.

In PPMS relaxation technique was used to measure heat capacity of a material. In this method, a known amount of heat was applied at constant power for a fixed time which was followed by cooling down time of the same duration. The temperature response was then fitted to a relaxation model to obtain the heat capacity value. In this modeling, thermal relaxation of the sample platform to the temperature bath as well as the relaxation between the sample platform and the sample was accounted for. The sample was mounted on the sample platform by Apiezon grease. First, the heat capacity of this addendum was recorded and then the heat capacity of the sample with addendum was measured. The addendum heat capacity was then subtracted from the measured heat capacity of the sample with addenda to obtain the heat capacity of the

sample.

2.2 Theoretical methods

In this thesis, the calculations of electronic structure and magnetic exchange interaction parameters of disordered alloys have been carried out based on first-principles density functional theories. We used tight-binding linear muffin-tin orbital (TB-LMTO) [82] based augmented space recursion (ASR) [83] to study the electronic structure of the materials. The electronic structure calculations were then further advanced to the calculations of magnetic exchange interaction parameters. The obtained magnetic exchange interaction parameters were then used in Monte-Carlo simulations to study finite-temperature magnetic properties of the materials. The materials studied in this thesis are disordered in nature. Various methods are available to handle disorder in a system such as ASR [83], special quasi-random structure (SQS) [84], coherent potential approximation (CPA) [85–88] etc. The methods of DFT based electronic structure calculations, the calculations of magnetic exchange interaction parameters and the theories of disordered alloys are briefly discussed in the sections below.

2.2.1 Density functional theory

Solids are made of its constituent atomic species and each atomic species have a positively charged nucleus and negatively charged electrons. The starting point of first-principles calculations of a material comprising N_c ion-cores and N_e valance electrons is the many-body Schrödinger equation with Hamiltonian (in atomic units) [89]:

$$\mathscr{H} = \sum_{I=1}^{N_c} \frac{-\nabla_I^2}{2M_I} + \frac{1}{2}\sum_{i=1}^{N_e} -\nabla_i^2 + \frac{1}{2}\sum_{i,j}\frac{1}{r_{ij}} + \mathscr{V}_{eI}(\{\mathbf{r}_i\},\{\mathbf{R}_I\}) + \mathscr{V}_{II}(\{\mathbf{R}_I\}) \tag{2.5}$$

where M_I is the mass of the I^{th} ion-core, $\mathbf{r}_i$ and $\mathbf{R}_J$ are respectively the positions of electrons and ions, $r_{ij} = |\mathbf{r}_i - \mathbf{r}_j|$ is the distance between i^{th} and j^{th} electrons, $\mathscr{V}_{II}$ and $\mathscr{V}_{eI}$ are respectively the Coulomb interactions between the ion-cores themselves and between the electrons and ions. Now, according to the Born-Oppenheimer approximation, during the short mean free time of electrons motion ions can be treated as stationary since they are much heavier than electrons and can be decoupled from the electronic degrees of freedom. Then the many-body Schrödinger equation with the Hamiltonian given in Eq. 2.5 can be solved for the wave functions of electrons alone. Consequently, for a given positions of the ion-cores $\{\mathbf{R}_I\}$, the Schrödinger equation of the system reduces to:

$$\left[-\sum_{i=1}^{N_e} \frac{\nabla_i^2}{2} + \mathscr{V}_{eI}(\{\mathbf{r}_i\}|\{\mathbf{R}_I\}) + \frac{1}{2}\sum_{i,j} \frac{1}{r_{ij}} \right] \psi(\{\mathbf{r}_i\}|\{\mathbf{R}_I\}) = E(\{\mathbf{R}_I\})\psi(\{\mathbf{r}_i\}|\{\mathbf{R}_I\}) \tag{2.6}$$

where ψ is the many-body electronic wave function and E is the total energy. However, as solids contain a large number of electrons, direct solution of Eq. 2.6 still remains impractical. The density functional theory in which the ground state properties of a system is described by the electron density $n(\mathbf{r})$ is one of the most popular method to approximately solve the above problem. The method arises from the two theorems provided by Hohenberg and Kohn [90] which tell us that for a electronic system in an external potential, the potential is a unique functional of the electron density $n(\mathbf{r})$ and the ground state energy obtained from the total energy functional is lowest only when the corresponding $n(\mathbf{r})$ is the true ground state density. The total energy functional of the system can be expressed as:

$$E^{(HK)}[n(\mathbf{r})] = T_S[n(\mathbf{r})] + E_H[n(\mathbf{r})] + E_{xc}[n(\mathbf{r})] + \int \mathscr{V}_{ext}(\mathbf{r})n(\mathbf{r})\mathrm{d}\mathbf{r} \tag{2.7}$$

where $\mathscr{V}_{ext}(\mathbf{r})$ is the external potential, $T_S[n]$ is the kinetic energy of non-interacting electrons, $E_H[n] = \frac{1}{2}\int\int \frac{n(\mathbf{r})n(\mathbf{r}')}{|\mathbf{r}-\mathbf{r}'|}\mathrm{d}\mathbf{r}\mathrm{d}\mathbf{r}'$ is the Hartree energy and $E_{xc}[n]$ is the exchange

correlation energy. The exchange-correlation energy comprises of the difference between the exact and the non-interacting kinetic energies, and also contain the non-classical contribution to the electron-electron interactions. However, the Hohenberg-Kohn theorem does not suggest a way to compute the ground state electron density. The route to obtain this was provided by Kohn and Sham [91] where they suggested to minimise the Hohenberg-Kohn energy functional E^{HK} with respect to the electron density

$$n(\mathbf{r}) = \sum_{i=1}^{N_e} \psi_i^*(\mathbf{r})\psi_i(\mathbf{r}) \tag{2.8}$$

which leads to the famous Kohn-Sham equation

$$\left[-\frac{\nabla_i^2}{2} + \mathcal{V}_{eff}(\mathbf{r}) \right] \psi_i(\mathbf{r}) = \epsilon_i \psi_i(\mathbf{r}) \tag{2.9}$$

where ϵ_i is the orbital energy corresponding to the Kohn-Sham orbital ψ_i and

$$\mathcal{V}_{eff}(\mathbf{r}) = \mathcal{V}_{ext}(\mathbf{r}) + \mathcal{V}_H(\mathbf{r}) + \mathcal{V}_{xc}(\mathbf{r}) \tag{2.10}$$

$\mathcal{V}_H(\mathbf{r}) = \int \frac{n(\mathbf{r}')}{|\mathbf{r}-\mathbf{r}'|} d\mathbf{r}'$ is the Hartree potential and $\mathcal{V}_{xc}(\mathbf{r}) = \frac{\delta E_{xc}[n]}{\delta n(\mathbf{r})}$ is the exchange-correlation potential. The above equation describes the behaviours of electron in an effective local potential. When the exact functional is known, the above set of equations gives ground state density and energy of the system. However, the exact form of exchange-correlation term in the Kohn-Sham Hamiltonian is unknown. Different approximation methods like local density approximation (LDA) [92, 93], generalized gradient approximation (GGA) [94] have been developed to calculate this exchange-correlation term.

2.2.2 Linear muffin-tin orbital method

The linear muffin-tin orbital (LMTO) [95, 96] is one of the widely used DFT based methods of electronic structure calculations. The crystal is divided into two re-

gions: muffin-tin spheres centred around the atoms and the interstitial region. Within atomic sphere approximation (ASA) [96], the neighbourhood of the ion-cores has a spherically symmetric potential $\mathscr{V}_{\mathbf{r}}$ within each atom-centred sphere of radius S_{MT} which resembles that of a free atom and the interstitial region has a flat potential $\mathscr{V}_{MTZ}$ which is called muffin-tin zero. Inside the interstitial region, $\mathscr{V}_{MTZ}$ is just a level shifting constant and can be set to zero. The muffin-tin potential is then given by:

$$\mathscr{V}_{\mathrm{MT}}(\mathbf{r}) = \begin{cases} \mathscr{V}(|\ \mathbf{r}-\mathbf{R}|) - \mathscr{V}_{\mathrm{MTZ}} & r \leq S_{MT} \\ 0 & r \geq S_{MT} \end{cases} \tag{2.11}$$

where $\mathbf{R}$ and $\mathbf{r}$ are the position of the ion-core and an electron respectively. We need to find the solution of one-electron Schrödinger equation for this MT potential. As the potential is spherically symmetric, the solution $\phi_{\mathbf{RL}}(\epsilon, \mathbf{r})$ inside the MT sphere is separable into a radial part $\phi_{Rl}(\epsilon, r)$ and a angular component $Y_l^m(\hat{\mathbf{r}})$ where l and m are the orbital and angular quantum numbers respectively and $\mathbf{L} = \{lm\}$. The radial Schrödinger equation inside the MT sphere has the form:

$$\left[-\frac{\mathrm{d}^2}{\mathrm{d}r^2} + \frac{l(l+1)}{r^2} + \mathscr{V}_{MT}(\mathbf{r}) - \kappa^2 \right] r\phi_{Rl}(\epsilon, r) = 0 \tag{2.12}$$

where $\kappa^2 = \epsilon - \mathscr{V}_{MTZ}$. Outside the MT sphere it takes the form:

$$\left[-\frac{\mathrm{d}^2}{\mathrm{d}r^2} + \frac{l(l+1)}{r^2} - \kappa^2 \right] r\phi_{Rl}(\epsilon, r) = 0 \tag{2.13}$$

the solution of which can be represented as linear combination of the spherical Bessel function $j_l(\kappa, r)$ which are regular at the origin and the spherical Neumann function $n_l(\kappa, r)$ which are regular at the infinity. The complete wave function for a this MT

potential is given by [96, 97]:

$$\phi_{\mathbf{RL}}(\epsilon,\kappa,\mathbf{r}_R)=\iota^l Y_{\mathbf{L}}(\hat{\mathbf{r}}_R)\begin{cases}\phi_{\mathbf{R}l}(\epsilon,r_R) & r_R\le S_{MT}\\ \kappa n_l(\kappa r_R)-\kappa\cot(\eta_{\mathbf{R}l})j_l(\kappa r_R) & r_R\ge S_{MT}\end{cases} \tag{2.14}$$

where $r_R=|\mathbf{r}-\mathbf{R}|$ and ι^l is a phase factor, $\eta_{\mathbf{R}l}(\epsilon,\kappa)$ is known as the phase shift of l-th partial wave. The MT orbitals are then defined as [96, 97]:

$$\chi^{MTO}_{\mathbf{RL}}(\epsilon,\kappa,\mathbf{r}_R)=\iota^l Y_{\mathbf{L}}(\hat{\mathbf{r}}_R)\begin{cases}\phi_{\mathbf{R}l}(\epsilon,r_R)+\kappa\cot(\eta_{\mathbf{R}l})j_l(\kappa r_R) & r_R\le S_{MT}\\ \kappa n_l(\kappa r_R) & r_R\ge S_{MT}\end{cases} \tag{2.15}$$

In the KKR-ASA (KKR: Korringa-Kohn-Rostocker) formalism [98, 99], the MT orbitals are defined in terms of overlapping atomic spheres. The MTO's are defined as [97]:

$$\chi^{MTO}_{\mathbf{RL}}(\epsilon,r_R)=\iota^l Y_{\mathbf{L}}(\hat{\mathbf{r}}_R)\begin{cases}\phi_{\mathbf{R}l}(\epsilon,r_R)+P^0_{\mathbf{R}l}(\epsilon)(r_R/s_R)^l & r_R\le S_R\\ (s_R/r_R)^{l+1} & r_R\ge S_R\end{cases} \tag{2.16}$$

where s_R is the radius of atomic sphere at $\mathbf{R}$ and

$$P^0_{\mathbf{R}l}(\epsilon)=2(2l+1)\frac{D_{\mathbf{R}l}(\epsilon)+l+1}{D_{\mathbf{R}l}-l} \tag{2.17}$$

is the potential function in which

$$D_{\mathbf{R}l}(\epsilon)=\frac{s_R}{\phi_{\mathbf{R}l}(\epsilon,s_R)}\frac{\partial\phi_{\mathbf{R}l}(\epsilon,r_R)}{\partial r_R}\bigg|_{r_R=s_R} \tag{2.18}$$

By applying 'tail cancellation' argument [96], one gets the KKR-ASA secular equation:

$$\sum_{\mathbf{RL}}\left[S^0_{\mathbf{R'L'},\mathbf{RL}}-P^0_{\mathbf{R'L'}}(\epsilon)\delta_{\mathbf{R'R}}\delta_{\mathbf{L'L}}\right]c_{\mathbf{RL}}=0 \tag{2.19}$$

where c_{RL} are the expansion coefficient of the MTO's in the Bloch sum [96] and $S^0_{\mathbf{R'L'},\mathbf{RL}}$

are the bare canonical structure matrix. This KKR-ASA secular equation has non-trivial solution if:

$$\det\left|S^0_{\mathbf{R'L'},\mathbf{RL}} - P^0_{\mathbf{R'L'}}(\epsilon)\delta_{\mathbf{R'R}}\delta_{\mathbf{L'L}}\right| = 0 \tag{2.20}$$

The diagonal elements of KKR-ASA matrix in Eq. 2.20 have energy dependence which arises from the potential function $P_{\mathbf{RL}}(\epsilon)$. The MTO's are energy dependent and Anderson developed a method to bypass this energy dependence [95]. The method involves Taylor expansion of $\phi_{\mathbf{RL}}(\epsilon,\mathbf{r})$ within a sphere about some arbitrarily chosen energy $\epsilon = E_v$ [97]:

$$\phi_{\mathbf{RL}}(\epsilon,\mathbf{r}_R) = \varphi_{\mathbf{RL}}(\mathbf{r}_R) + (\epsilon - E_v)\dot{\varphi}_{\mathbf{RL}}(\mathbf{r}_R) + \mathcal{O}(\epsilon - E_v)^2 \tag{2.21}$$

where $\varphi_{\mathbf{RL}}(\mathbf{r}) = \phi_{\mathbf{RL}}(E_v,\mathbf{r})$ and $\dot{\varphi}_{\mathbf{RL}}(\mathbf{r}) = \left[\frac{\partial\phi_{\mathbf{RL}}(\epsilon,\mathbf{r})}{\partial\epsilon}\right]_{\epsilon=E_v}$. The linear basis set is obtained by truncating the Taylor series after term linear in energy. In the most tight-binding representation, the LMTO basis is given by [82]:

$$\chi^{\beta}_{\mathbf{RL}}(\mathbf{r}_R) = \varphi_{\mathbf{RL}}(\mathbf{r}_R) + \sum_{\mathbf{R'L'}} \dot{\varphi}^{\beta}_{\mathbf{R'L'}}(\mathbf{r}_{R'})h^{\beta}_{\mathbf{R'L'},\mathbf{RL}} \tag{2.22}$$

where $\dot{\varphi}^{\beta}_{\mathbf{R'L'}}(\mathbf{r}')$ is given by:

$$\dot{\varphi}^{\beta}_{\mathbf{RL}}(\mathbf{r}) = \dot{\varphi}^{\gamma}_{\mathbf{RL}}(\mathbf{r}) + \varphi_{\mathbf{RL}}(\mathbf{r})O^{\beta}_{\mathbf{RL}} \tag{2.23}$$

O^{β} is the overlap matrix, β is a screening constant and characterize the representation of MTO, and γ indicates that $\varphi_{\mathbf{RL}}$ are normalized and also orthogonal to $\dot{\varphi}_{\mathbf{RL}}$. The expansion coefficient h^{β} is given by:

$$h^{\beta}_{\mathbf{R'L'},\mathbf{RL}} = (C^{\beta}_{\mathbf{RL}} - E_v)\delta_{\mathbf{RR'}}\delta_{\mathbf{LL'}} + (\Delta^{\beta}_{\mathbf{RL}})^{1/2}S^{\beta}_{\mathbf{RL},\mathbf{R'L'}}(\Delta^{\beta}_{\mathbf{RL}})^{1/2} \tag{2.24}$$

where $C^{\beta}_{\mathbf{RL}}$ and $\Delta^{\beta}_{\mathbf{RL}}$ are the diagonal potential parameter matrices defined as:

$$C^{\beta}_{\mathbf{RL}} = E_{\nu} - \frac{P^{\beta}_{\mathbf{RL}}(E_{\nu})}{\dot{P}^{\beta}_{\mathbf{RL}}(E_{\nu})}, \ (\Delta^{\beta}_{\mathbf{RL}})^{1/2} = \frac{1}{\dot{P}^{\beta}_{\mathbf{RL}}(E_{\nu})} \tag{2.25}$$

These are respectively called band center and band width. $S^{\beta}_{\mathbf{R'L'},\mathbf{RL}}$ is the screened structure matrix which depends on the representation β and lattice geometry. The second order TB-LMTO Hamiltonian in the orthonormal sparse representation is given by:

$$\mathscr{H}^{(1)} = E_{\nu} + h - hoh + \cdots \tag{2.26}$$

where we have suppressed the summation indices $R\mathbf{L}$.

2.2.3 Theories of disordered alloys

The difficulty in devising a first-principle theory of substitutionally disordered alloy systems mainly comes from two reasons. First is the breakdown of the translational symmetry due to which Bloch theorem becomes inapplicable. This can only be restored by representing the randomness via statistical occupancy of the constituent atoms. Another problem is the large number configuration space involved in the problem due to which all the calculated properties have to be configuration averaged.

2.2.3.1 Coherent potential approximation

The underlying point of this theory is to represent the randomness of the system by replacing the original medium by a mean of an effective medium. The root of such attempt is the virtual crystal approximation in which the actual potential of a disordered system is replaced with an average potential constructed from concentration weighted potential of constituent atoms. Then effective potential of a disordered A_xB_{1-x}

alloy can be written as:

$$\mathcal{V}_{eff} = x\mathcal{V}_A + (1-x)\mathcal{V}_B \tag{2.27}$$

where $\mathcal{V}_A$ and $\mathcal{V}_B$ are the potential associated the A and B atoms. This is a crude assumption, and becomes nearly inapplicable when the constituent atoms are not similar in nature. In the multiple scattering formalism [98, 99], the coherent potential approximation (CPA) [85] is described in terms of the scattering path operators τ [87, 100]. For a binary A_xB_{1-x} system, the CPA condition is:

$$\tau_{CPA} = x\tau_A + (1-x)\tau_B \tag{2.28}$$

This condition ensures that for the replacement of A(B) atom by a B(A) atom the scattering will remain same. The scattering properties of an A(B) atom embedded in the CPA medium is represented by the component-projected scattering path operators $\tau_{A(B)}$ as:

$$\tau_{A(B)} = \tau_{CPA}\left[1 + \left(t_{A(B)}^{-1} - t_{CPA}^{-1}\right)\tau_{CPA}\right]^{-1} \tag{2.29}$$

where t's are the scattering t-matrices which represent the scattering amplitudes from a lattice site.

2.2.3.2 Augmented space recursion

The augmented space recursion (ASR) [83] is another powerful method for the calculation of configuration averaged properties of disordered systems. This technique has been developed by bringing together the recursion technique of Haydock et al. and the augmented space formalism proposed by Mookerjee. In this thesis, the ASR has been used based on TB-LMTO basis [82] for electronic structure calculation. The brief discussion of the technique has been described below.

The augmented space formalism [97, 101] maps the Hamiltonian of a disor-

dered system, which is described in Hilbert space, onto an ordered Hamiltonian in the augmented space constructed by augmenting the configuration space of the random variables of the disordered Hamiltonian together with the Hilbert space of the disordered Hamiltonian. Let us consider a A_xB_{1-x} substitutionally disordered alloy. Here the lattice site occupation variables $z_{\mathbf{R}}$ are a random variables and take values +1 when the i-th site is occupied by an A atoms and 0 when it is occupied by a B atom. The probability density of $z_{\mathbf{R}}$ can be expressed as:

$$\Pr(z_{\mathbf{R}}) = x\delta(z_{\mathbf{R}} - 1) + (1-x)\delta(z_{\mathbf{R}}) \tag{2.30}$$

Now an operator $Z_{\mathbf{R}}$ can be associated with the random variable $z_{\mathbf{R}}$ in such a way that the eigenvalues of the operator $Z_{\mathbf{R}}$ are the values taken by $z_{\mathbf{R}}$ and the spectral density of $Z_{\mathbf{R}}$ is the probability density of $z_{\mathbf{R}}$. The configuration space of $z_{\mathbf{R}}$, $\Phi_{\mathbf{R}}$, is the space spanned by the eigenvector of $Z_{\mathbf{R}}$. The full configuration space of the system for the set of random variables $\{z_{\mathbf{R}}\}$ is $\Phi = \Pi \otimes \Phi_{\mathbf{R}}$. The augmented space theorem [101] states that the configuration average of any function $f(z_{\mathbf{R}})$ can be written as:

$$\ll f(z_{\mathbf{R}}) \gg = \langle \{\emptyset\} | \tilde{f}(\{\tilde{Z}_{\mathbf{R}}\}) | \{\emptyset\} \rangle \tag{2.31}$$

where $\tilde{f}(\{\tilde{Z}_{\mathbf{R}}\})$ is the same operator function of the operators $\{\tilde{Z}_{\mathbf{R}}\}$ as $\tilde{f}(\{\tilde{z}_{\mathbf{R}}\})$ is of $\{\tilde{z}_{\mathbf{R}}\}$. All the tilded operators act on the configuration space Φ. $|\{\emptyset\}\rangle = \prod \otimes |\Phi_{\mathbf{R}}\rangle$ and $\tilde{Z}_{\mathbf{R}_i} = \mathbf{I} \otimes \cdots \mathbf{I} \otimes Z_{\mathbf{R}} \otimes \mathbf{I} \cdots \in \Phi$.

The advantage of ASR over CPA is that ASR is not a single-site approximation. Also, both diagonal and off-diagonal disorder can be treated on equal footing in this method. However, the large dimension of the augmented space is a computational burden. We used TB-LMTO Hamiltonian with ASR, because the TB-LMTO orbitals are short-ranged resulting in a sparse Hamiltonian. The most localized TB-LMTO Hamiltonian described in Sec. 2.2.2 can be written for a substitutionally disordered binary

A_xB_{1-x} alloy as [102]:

$$\mathscr{H}^{\beta}_{\mathbf{RL},\mathbf{R'L'}} = C_{\mathbf{RL}}\delta_{\mathbf{RR'}}\delta_{\mathbf{LL'}} + (\Delta_{\mathbf{RL}})^{1/2} S^{\beta}_{\mathbf{RL},\mathbf{R'L'}} (\Delta_{\mathbf{R'L'}})^{1/2} \tag{2.32}$$

where

$$C_{\mathbf{RL}} = C^{A}_{\mathbf{RL}} z_{\mathbf{R}} + C^{B}_{\mathbf{RL}}(1 - z_{\mathbf{R}}) \quad \text{and} \quad \Delta_{\mathbf{RL}} = \Delta^{A}_{\mathbf{RL}} z_{\mathbf{R}} + \Delta^{B}_{\mathbf{RL}}(1 - z_{\mathbf{R}}) \tag{2.33}$$

where $\mathbf{R}$ denotes the lattice sites, $\mathbf{L} = \{lm\}$ is the orbital index, and $z_{\mathbf{R}}$ is the local site occupation variable which takes values 1 and 0 according to whether the site is occupied by an A atom or not. The augmented space Hamiltonian $\tilde{H}$ is constructed from this TB-LMTO Hamiltonian. The details of this construction can be found in Ref. [102, 103]. Then the configuration averaged Green's function of the system can be written as:

$$\ll G_{\mathbf{RL},\mathbf{R'L'}} \gg = \langle \mathbf{RL}\{\emptyset\} | \, G(E) \, \big| \mathbf{R'L'}\{\emptyset\} \big\rangle \tag{2.34}$$

where

$$G(E) = (E\tilde{I} - \tilde{\mathscr{H}})^{-1} \in \Psi = \mathscr{H} \otimes \Phi \tag{2.35}$$

and $|\mathbf{RL}\{\emptyset\}\rangle = |\mathbf{RL}\rangle \bigotimes \{\emptyset\}$ is a particular state in augmented space Ψ. Therefore, within this augmented space formalism, the configuration averaging reduces to the evolution of ground state matrix element in the augmented space. This theoretical result is exact and the approximations will appear only in the calculation of the matrix elements. Here the recursion method of Haydock et al. [104] is used to obtain the matrix elements in the augmented space. The recursion method tridiagonalizes the system Hamiltonian via a three term recursion relations:

$$b_{n+1} |\phi_{n+1}\rangle = \mathscr{H} |\phi_n\rangle - a_n |\phi_n\rangle - b_n |\phi_{n-1}\rangle \tag{2.36}$$

where a_n and b_n are the diagonal and off-diagonal elements of the tri-diagonalized Hamiltonian. The diagonal part of the averaged Green's function can be expressed as

continued fraction given by:

$$\ll G_{\mathbf{RL},\mathbf{RL}}(E) \gg = \cfrac{1}{E - a_0 - \cfrac{b_1^2}{E - a_1 - \cfrac{b_2^2}{E - a_2 - \cfrac{b_3^2}{E - a_3 - \cfrac{b_4^2}{\ddots}}}}} \tag{2.37}$$

The averaged projected density of states is given by:

$$n_{\mathbf{RL}}(E) = -\frac{1}{\pi}\text{Im Tr}\{\langle \mathbf{RL}\{\emptyset\}|\, \tilde{G}(E + i0)\, |\mathbf{RL}\{\emptyset\}\rangle\} \tag{2.38}$$

The detailed implementation of this method can be found in Ref. [102, 103, 105–108].

2.2.3.3 Special quasi-random structure

One of the methods of handling randomness is supercell method in which a bigger cell is created out of the unit cell and the lattices are populated randomly by the constituent atoms. The underlying assumption is that it represents a random environment, however, it is always very likely to have local correlations between the constituent atomic species and consequently deviation occurs from perfect randomness. In general, how much the supercell deviates from the perfect randomness is not considered. Another problem is that the supercell needs to very large which is computationally demanding for first-principles calculations. In this direction, Zunger et al. [84] proposed the construction of special quasi-random structures through the minimization of multisite correlations functions so that the resulting supercell mimic the correlation functions to that of a substitutional alloy more closely than the standard method of randomly

populating the supercell by the constituent atoms. While both the standard supercell method and SQS are equivalent for $N \to \infty$, N being the number of sites, SQS method more closely represents the disordered environment for smaller N [84, 109]. The basic principle on which SQS method relies on for getting an accurate disordered averaged properties of the system is the assumption that the underlying interaction of the property of interest is hierarchical i.e., distant neighbors have less effect compared to close neighbors in determining the system property. So, the multisite correlation function of the structure is minimized hierarchically to mimic the disordered state in SQS.

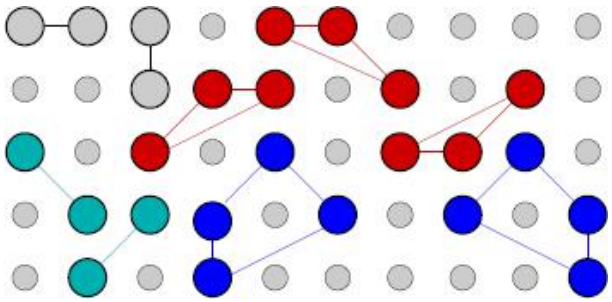

Figure 2.12: Illustration of different 'figures' showing pairs, triplets, and quadruplets in a lattice. Image source Ref. [110].

Let us consider a given arrangement Ω of A and B atoms on a lattice with N number of sites. Each sites i can be characterized by a Ising like spin variable $S_i = \pm 1$ ($+1$ if it is occupied by A and -1 if occupied by B). This arrangement can be grouped into its component figures $\mathscr{F}(N_v, k)$ of N_v vertices, where $N_v = 1, 2, 3, \cdots$ corresponds to the shape point, pairs, triplets $\cdots$ respectively, separated by k-th neighbor distance (see Fig. 2.12 for example). If there are $D_{\mathscr{F}}$ number of figures per site, the correlation function of the configuration can be written as:

$$\overline{\Pi}_{\mathscr{F}}(\Omega) = \frac{1}{N D_{\mathscr{F}}} \sum_i \Pi_{\mathscr{F}}(\mathbf{r}, \Omega) \tag{2.39}$$

where $\mathbf{r}$ represent the position of the figure $\mathscr{F}$ in the lattice. Then the ensemble average

of a physical property P over configurations can be written as:

$$< P > = \sum_{N_v,k} D_{N_v,k} < \overline{\Pi}_{N_v,k} > p_{N_v,k} \tag{2.40}$$

where the angular brackets denotes the configuration averaging, $p_{N_v,k}$ is the interaction parameter of the figure $\mathscr{F}(N_v,k)$ corresponding to the physical property P and $< \overline{\Pi}_{N_v,k} >$ is the correlation function. For a perfectly random substitutionally disordered A_xB_{1-x} alloy, $< \overline{\Pi}_{N_v,k} >_{RND} = (2x-1)^{N_v}$. The idea of SQS is, instead of approaching $< \overline{\Pi}_{N_v,k} >_{RND}$ through statistical sampling, design a structure S whose distinct correlation function $\overline{\Pi}_{N_v,k}(SQS)$ best matches to $< \overline{\Pi}_{N_v,k} >_{RND}$ by hierarchically minimizing the correlations functions [84].

The situation of short-range ordering and clustering can also be incorporated into SQS through Warren-Cowley short-range order parameter α. For the k-th pair of nearest neighbor, α_k in terms of the pair correlation function $\overline{\Pi}_{2,k}$ can be written as [111]:

$$\alpha_k = \frac{\overline{\Pi}_{2,k} - (2x-1)^2}{1-(2x-1)^2} \tag{2.41}$$

Although the SQS approach of modeling disordered alloys is an elegant systematic procedure, the difficulty of generating a desired SQS increases with increasing system size. This is because, with increasing system size, the number of possible configuration also increase: for a random binary alloy with N atoms, the number of configuration is 2^N. For low values of N one can go through all the configuration to check the correlation functions of which configuration best matches with the desired target and select that best configuration as the SQS. However, this approach becomes increasingly prohibitive due to computational workload as N increases. Another method is the Monte-Carlo simulated annealing in which one gradually minimizes the difference of correlation functions $[< \overline{\Pi}_{N_v,k} >_{RND} - \overline{\Pi}_{N_v,k}(SQS)$ [112, 113]. The SQS used in this thesis were generated in Ref. [110].

2.2.4 Calculation of magnetic exchange interaction parameters

So far the discussion of ab-initio method is on the ground state electronic and magnetic properties of the system. However, to understand the formation of magnetic phases and finite-temperature magnetic properties we need to calculate the magnetic exchange interaction parameters and analysed them using a model that describes phase formation. In this thesis this has been done within the framework of generalized perturbation method (GPM) [114] which maps the problem of magnetic ordering of a disordered alloy system to an effective Ising model. In a completely disordered state with paramagnetic phase, the magnetic moments of the atomic spheres point randomly along the quantization direction or opposite to it. For a local perturbation, the total energy of this state can be written as:

$$E = E^{(0)} + \sum_{\mathbf{R}_i} E^{(1)Q}(\mathbf{R}_i)\delta\xi^{Q}_{\mathbf{R}_i} + \frac{1}{2}\sum_{\mathbf{R}_i}\sum_{\mathbf{R}_j} E^{(2)QQ'}(\mathbf{R}_i,\mathbf{R}_j)\delta\xi^{Q}_{\mathbf{R}_i}\delta\xi^{Q'}_{\mathbf{R}_j} + \cdots \tag{2.42}$$

where Q and Q' are the constituent atomic species, $\mathbf{R}_i$ and $\mathbf{R}_j$ are respectively the position of Q and Q' and $\delta\xi^{Q}_{\mathbf{R}_i}$ is the perturbation in the occupation variable $\xi^{Q}_{\mathbf{R}_i}$ which take the values ± 1 according to whether the atomic sphere situated at the site $\mathbf{R}_i$ have magnetic moment oriented along the quantization direction or opposite to it. $E^{(0)}$ is the energy of the unperturbed disordered paramagnetic state, $E^{(1)Q}$ is the configuration averaged total energy in which the site $\mathbf{R}_i$ is occupied by Q atom and other sites are randomly occupied with randomly oriented magnetic moments. These two terms plays no role in the emergence of ordering in the bulk. $E^{(2)QQ'}$ is the pair interaction energy which is the dominant term in determining the magnetic ordering of the system. This term can be written as:

$$J^{QQ'}(\mathbf{R}_i,\mathbf{R}_j) = E^{(2)QQ'}(\mathbf{R}_i,\mathbf{R}_j) = \sum_{\xi^{Q}_{\mathbf{R}_i}}\sum_{\xi^{Q'}_{\mathbf{R}_j}} (2\delta_{\xi^{Q}_{\mathbf{R}_i},\xi^{Q'}_{\mathbf{R}_j}} - 1) E^{Q\xi^{Q}_{\mathbf{R}_i},Q'\xi^{Q'}_{\mathbf{R}_j}}_{\mathbf{R}_i,\mathbf{R}_j} \tag{2.43}$$

where $E_{\mathbf{R}_i,\mathbf{R}_j}^{Q\xi^Q_{\mathbf{R}_i},Q'\xi^{Q'}_{\mathbf{R}_j}}$ is the total energy of a paramagnetic background with the sites $\mathbf{R}_i$ and $\mathbf{R}_j$ respectively occupied by Q and Q' with alignments of magnetic moments in their respective atomic sphere as $\xi^Q_{\mathbf{R}_i}$ and $\xi^{Q'}_{\mathbf{R}_j}$. The energy terms $E_{\mathbf{R}_i,\mathbf{R}_j}^{Q\xi^Q_{\mathbf{R}_i},Q'\xi^{Q'}_{\mathbf{R}_j}}$ are large ($\sim 10^3$ Ry) whereas $E^{(2)QQ'}(\mathbf{R}_i,\mathbf{R}_j)$ is a very small ($\sim$ mRy) energy difference among $E_{\mathbf{R}_i,\mathbf{R}_j}^{Q\xi^Q_{\mathbf{R}_i},Q'\xi^{Q'}_{\mathbf{R}_j}}$. Therefore a separate calculations of each $E_{\mathbf{R}_i,\mathbf{R}_j}^{Q\xi^Q_{\mathbf{R}_i},Q'\xi^{Q'}_{\mathbf{R}_j}}$ will produce errors larger than the small difference themselves and consequently mask $E^{(2)QQ'}(\mathbf{R}_i,\mathbf{R}_j)$. Therefore, $E^{(2)QQ'}(\mathbf{R}_i,\mathbf{R}_j)$ has been calculated directly using two different formalisms namely Liechtenstein formula and orbital peeling method.

The pair interaction term is related to the change in configuration averaged local density of states as [106, 107, 115]:

$$E^{(2)QQ'}(\mathbf{R}_i,\mathbf{R}_j) = \int_{-\infty}^{E_F} \mathrm{d}E(E-E_F)\Delta \ll n(E) \gg \tag{2.44}$$

where E_F is the Fermi energy and

$$\Delta \ll n(E) \gg = -\frac{1}{\pi}\mathrm{Im}\sum_{\xi^Q_{\mathbf{R}_i},\xi^{Q'}_{\mathbf{R}_j}} (2\delta_{\xi^Q_{\mathbf{R}_i},\xi^{Q'}_{\mathbf{R}_j}} - 1)\mathrm{Tr} \ll (E\mathbf{I} - \mathscr{H}^{Q\xi^Q_{\mathbf{R}_i},Q'\xi^{Q'}_{\mathbf{R}_j}})^{-1} \gg \tag{2.45}$$

where $\mathscr{H}^{Q\xi^Q_{\mathbf{R}_i},Q'\xi^{Q'}_{\mathbf{R}_j}}$ is the Hamiltonian of the system for Q and Q' occupying the sites $\mathbf{R}_i$ and $\mathbf{R}_j$ and all other sites are randomly occupied. Now the change in averaged local density of states can be related to the generalized phase shift $\eta(E)$ through the relation:

$$\Delta \ll n(E) \gg = \frac{\mathrm{d}\eta(E)}{\mathrm{d}E} = \frac{\mathrm{d}}{\mathrm{d}E}\left[\log\left(\frac{\det \ll G^{Q\xi^Q_{\mathbf{R}_i},Q\xi^Q_{\mathbf{R}_j}}(E) \gg \det \ll G^{Q'\xi^{Q'}_{\mathbf{R}_i},Q'\xi^{Q'}_{\mathbf{R}_j}}(E) \gg}{\det \ll G^{Q\xi^Q_{\mathbf{R}_i},Q'\xi^{Q'}_{\mathbf{R}_j}}(E) \gg \det \ll G^{Q'\xi^{Q'}_{\mathbf{R}_i},Q\xi^Q_{\mathbf{R}_j}} \gg}\right)\right] \tag{2.46}$$

where $\ll G^{Q\xi^Q_{\mathbf{R}_i},Q'\xi^{Q'}_{\mathbf{R}_j}}(E) \gg$ is the configuration averaged resolvent of the Hamiltonian $\mathscr{H}^{Q\xi^Q_{\mathbf{R}_i},Q'\xi^{Q'}_{\mathbf{R}_j}}$. The integral is complicated and also the multivalued nature of $G^{Q\xi^Q_{\mathbf{R}_i},Q'\xi^{Q'}_{\mathbf{R}_j}}$ makes it difficult to compute it in standard method. The alternative method is the orbital peeling as suggested by Burke [116]. Here the pair energy interaction term can

be written as [115]:

$$E^{(2)QQ'}(\mathbf{R}_i,\mathbf{R}_j)=\sum_{Q,Q'}\sum_{l=1}^{l_{max}}\left[\sum_{k=1}^{z^{l,QQ'}}Z_k^{l,QQ'}-\sum_{k=1}^{p^{l,QQ'}}P_k^{l,QQ'}+\left(p^{l,QQ'}-z^{l,QQ'}\right)E_F\right] \tag{2.47}$$

where l is the orbital index, $Z^{l,QQ'}$ and $P^{l,QQ'}$ are the zeros and poles of the configuration averaged Green function $\ll G^{Q\xi^Q_{\mathbf{R}_i},Q'\xi^{Q'}_{\mathbf{R}_j}}(E)\gg$ and $z^{l,QQ'}$ and $p^{l,QQ'}$ are number of such zeros and poles below E_F. The zeros and poles are obtained directly from the recursion coefficients for the averaged resolvent calculated from the TB-LMTO-ASR. The detailed implementation of this method can be found in the Ref. [106, 107, 115].

In the Liechtenstein method [117, 118] of magnetic exchange interaction calculation, the magnetic system is perturbed by giving a small rotations to the local magnetic moments and the magnetic exchange interaction parameters are calculated from the resulting change in total energy employing force theorem. In the Green function method with TB-LMTO basis and under coherent potential approximation, the pair exchange energy can be expressed as:

$$J^{QQ'}(\mathbf{R}_i,\mathbf{R}_j)=\frac{1}{4\pi}\int_{-\infty}^{E_F}\mathrm{d}E\ \mathrm{Im\ Tr}\left\{\Delta^Q_{\mathbf{R}_i}T^{Q\uparrow Q'\uparrow}(\mathbf{R}_i-\mathbf{R}_j)\Delta^{Q'}_{\mathbf{R}_j}T^{Q\downarrow Q'\downarrow}(\mathbf{R}_j-\mathbf{R}_i)\right\} \tag{2.48}$$

where Q and Q' are the constituent atoms, $\Delta_{\mathbf{R}}=t^{-1}_{\mathbf{R},Q}-t^{-1}_{\mathbf{R},Q'}$ in which t is the scattering t-matrix and $T^{Q\downarrow Q'\downarrow}(\mathbf{R}_j-\mathbf{R}_i)$ is the scattering path operator related to the off-diagonal element of the Green's function. This Liechtenstein formula can also be used to calculate the magnetic exchange interaction parameters [119–121].

The GPM method maps the problem of magnetic ordering of an alloy system onto an effective Ising model given by:

$$\mathscr{H}=-\frac{1}{2}\sum_{\vec{R}_i}\sum_{\vec{R}_j}J^{QQ'}\left(|\vec{R}_i-\vec{R}_j|\right)S_{\vec{R}_i}S_{\vec{R}_j} \tag{2.49}$$

where $J^{QQ'}\left(|\vec{R}_i - \vec{R}_j|\right)$ is the magnetic exchange interaction between the constituent atomic species Q and Q' situated at the sites $\vec{R}_i$ and $\vec{R}_j$, $S_{\vec{R}_i}$ takes the values ±1 according to whether the moment situated at the site $\vec{R}_i$ is oriented along the global quantization direction or opposite to it. Monte-Carlo simulations have been carried out with this Hamiltonian and the calculated magnetic exchange interaction parameters. The implementation of the Monte-Carlo code used in this thesis can be found in Ref. [110].

3 Magnetic Properties of Disordered Fe:Al Alloy: Effects of Short-Range Ordering

3.1 Introduction

Magnetic properties of FeAl alloy at the equiatomic composition have been investigated extensively over the years, however still a universally accepted understanding is lacking. The equiatomic FeAl alloy crystallizes into a CsCl-type cubic B2 structure (space group number and symbols are 221 and $Pm\bar{3}m$, respectively) in thermodynamic equilibrium [42–45]. The B2 structure is an ordered atomic arrangement comprising two interpenetrating simple cubic lattices of Fe and Al. A pictorial depiction of the B2 structure is shown in Fig. 1.1(b) in Chapter 1. Experimental studies indicate that this B2 Fe:Al is a Curie-Weiss paramagnet with a very small Fe magnetic moment $\mu_{Fe} \approx 0.3\mu_B$ [122, 123]. However, electronic structure calculations within first-principles density functional theory (DFT) predict a ferromagnetic ground state with $\mu_{Fe} \approx 0.7\mu_B$ [123–132]. Although the energy difference between the ferromagnetic and the non-magnetic ground states found in those calculations was very small, the ferromagnetic ground state is persistent in all the calculations irrespective of the differences, such as the orbital basis set or the exchange-correlation functional, in the DFT codes. Mohn et al. [133] became successful in producing paramagnetic ground state through DFT + U calculations for a range of U values between 3.7 eV and 5 eV. However, this behavior is in contradiction to the common perception that DFT + U promotes magnetism. This contradictory role of U and the origin of such a strong electron correlation in Fe:Al are

still not properly understood. Recent DFT + DMFT (DMFT: Dynamical Mean-Field Theory) calculation by Galler et al. [134] suggests that the temporal quantum fluctuations of the magnetic moments result in the paramagnetic behavior.

Magnetic moments of the Fe atoms in FeAl alloys strongly depend on their local atomic environments. Studies have shown that the Fe atoms are magnetic only when they are surrounded by four or more number of nearest neighbor Fe atoms [46–50, 130, 135, 136]. B2 phase of the FeAl alloys is susceptible [122, 127, 137–144] to antisite or triple defects [145] in which the antisite Fe atoms are surrounded by eight nearest neighbor Fe atoms. This antisite Fe atoms have large local magnetic moments and polarize other non-magnetic Fe atoms situated on their regular sites [122–127, 135, 143, 144, 146, 147]. The ordered B2 Fe:Al can be transformed into a disordered body centered cubic A2 structure (the space group number and symbol are 229 and $Im\bar{3}m$, respectively, and a depiction of the structure is shown in Fig. 1.2(b)) by a variety of methods such as ball milling [47], rapid quenching from high temperatures [46, 48], cold working [136], plastic deformation [148] etc. Disorder in this A2 phase is of substitutional type, and Fe and Al atoms have equal probability to occupy any of the lattice sites (i.e., occupational probabilities for both Fe and Al atoms is 0.5 for any lattice sites). As the number of nearest neighbor is eight in the A2 structure, Fe atoms are surrounded by four nearest neighbor Fe atoms on average and therefore retain a local magnetic moment. DFT based electronic structure calculations [124, 129, 132] indicate that Fe atoms are magnetic in this A2 phase in accordance with this expectation. However, experimental results vary among various groups on how these Fe moments order at low temperature. While some studies indicated that the low temperature state was ferromagnetic, others suggested a spin glass state. The possibility of a noncollinear magnetic state has also been suggested [123, 149]. Experimental reports [46–48, 135, 136, 149] also vary on the transition temperature, magnetic moment and effective internal field of A2 Fe:Al alloy.

It is important to note that as the ordered B2 structure is the thermodynamical equilibrium phase of the Fe:Al alloy, short-range ordered structure tends to form in the disordered background of A2 phase [135, 136, 150]. Because of the strong dependence of Fe moment on their local atomic environment, the presence of such short-range ordering affects the magnetic properties of the disordered A2 phase. In short, magnetic properties around this equiatomic concentration region are extremely sensitive to the structural phases present in the sample and the nature of atomic ordering in the structure. This chapter is devoted to the study of magnetic properties of Fe:Al alloy and the effects of short-range ordering. First, the experimental data are presented, and then they have been analyzed with DFT based electronic structure calculations and Monte-Carlo simulations.

3.2 Sample preparation and compositional characterization

A polycrystalline ingot of Fe:Al was prepared by arc-melting appropriate amounts of high purity ($\geq$ 99.9%) constituent elements and was annealed at 1000 °C for seven days. The annealing was followed by quenching of the ingot into liquid nitrogen to arrest the high temperature disordered phase. The average composition of the ingot obtained from EPMA analysis was $Fe_{51.3\pm0.2}Al_{48.7\pm0.2}$ which is close to the target composition with good compositional homogeneity.

3.3 Structural characterization

XRD pattern was collected at room temperature using powdered specimens in the powder diffractometer with Mo-Kα X-ray source and is shown in Fig. 3.1. (h k l)

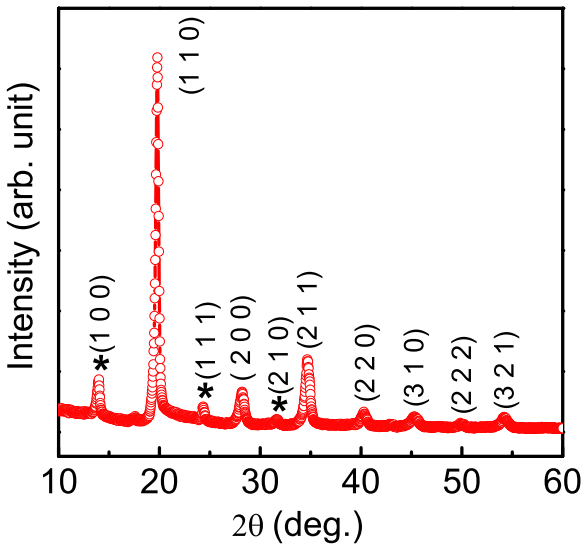

Figure 3.1: XRD pattern of Fe:Al alloy collected using Mo-Kα X-ray source.

indices of all peaks are marked in the graph. Except for the * marked peaks, all others correspond to BCC structure and confirm the formation of the A2 FeAl alloy. The * marked peaks at $2\theta = 14°$, 24.35°, and 31.61° are the superlattice (1 0 0), (1 1 1), and (2 1 0) peaks, respectively, from the B2 phase. The presence of these peaks from the B2 phase indicates the formation of minute amount of ordered domains along with the disordered (A2) phase. The formation of such ordered domains in the disordered background results in inhomogeneity in the sample and has been reported in earlier studies also [136]. Therefore, we assume that our sample is largely disordered, with islands of ordered phase scattered in the disordered background.

3.4 Magnetic properties

3.4.1 DC magnetization

ZFC and FC magnetizations were measured in a SQUID magnetometer. Temperature variations of ZFC and FC magnetizations, measured at $H = 25$ Oe and $H =$

100 Oe, are shown in Fig. 3.2. A rounded peak appeared around temperature T_{sg} in both ZFC and FC magnetizations. ZFC and FC magnetizations, measured at $H = 25$ Oe, started bifurcating at around 250 K, far above the peak temperature T_{sg} . However, there was no such bifurcation between ZFC and FC magnetizations above T_{sg} when measurements were carried out at a higher applied field, $H = 100$ Oe. The presence of bifurcation between ZFC and FC magnetizations at such high temperature and low field reflects the inhomogeneous nature of the sample, which is also evident in the XRD study. Below T_{sg}, ZFC magnetizations, measured at $H = 25$ Oe and $H = 100$ Oe, started to decrease and a further significant bifurcation between ZFC and FC magnetizations appeared similar to those of spin glass systems [26–29]. The values of T_{sg} at $H = 25$ Oe and $H = 100$ Oe are ≈ 55 K and ≈ 35.5 K, respectively. This drastic shift of T_{sg} with H at such low field depicts the sensitivity of the peak to applied magnetic field and is also typical of a spin glass system [26–29].

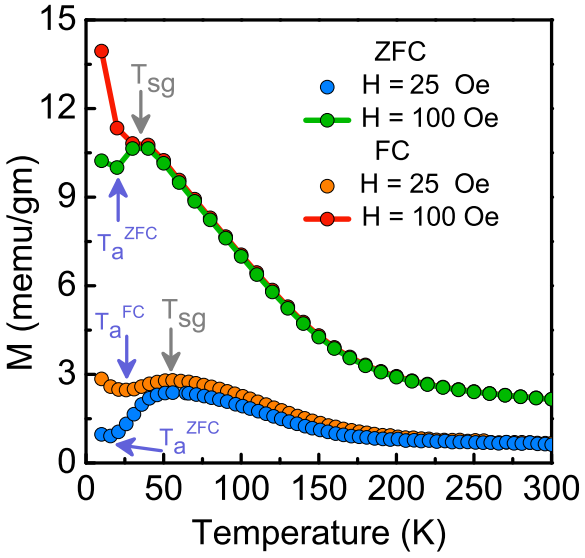

Figure 3.2: Temperature variations of ZFC and FC magnetizations of Fe:Al alloy measured at $H = 25$ Oe and $H = 100$ Oe.

As the temperature was lowered further below T_{sg}, magnetization showed a dip around temperature T_a followed by an upturn. The values of T_a for ZFC and FC magnetizations measured at $H = 25$ Oe are $T_a^{ZFC} \approx 16$ K and $T_a^{FC} \approx 25$ K, respectively.

When H was increased from 25 Oe to 100 Oe, the temperature variations of ZFC and FC magnetizations retained the same characteristic behaviour. Value of T_a^{ZFC} at H = 100 Oe is ≈ 20 K which shows that T_a increases with the strength of applied magnetic field. However, T_a^{FC} at H = 100 Oe was not resolved due to the fact that T_a increases, whereas T_{sg} decreases as H increases, which result in decreasing the gap between them, and thereby brings out the unresolved magnetization behaviour in the region.

3.4.2 AC susceptibility

Temperature variation of ac susceptibility was measured at an excitation field of H_{ac} = 10 Oe in a PPMS® system and data were recorded for several different frequencies. AC susceptibility, shown in Fig. 3.3, depicts a rounded peak at T_{sg}. The value of T_{sg} at f = 100 Hz is ≈ 53.5 K which is in agreement to the value of T_{sg}^{ZFC} at H = 25 Oe. T_{sg} was found to be sensitive to the frequency of excitation field and shifted towards higher temperatures with increasing frequency. Such a frequency dependence is a typical behavior of spin glass system [26–29]. In such a system, a quantitative measure

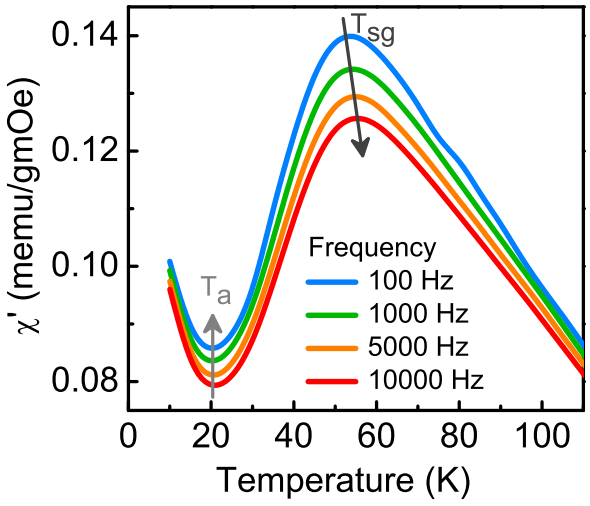

Figure 3.3: Temperature variation and frequency dependence of ac susceptibility of Fe:Al alloy.

of the shift of T_{sg} with frequency is expressed as $\phi = \Delta T_{sg}/(T_{sg}\Delta \log f)$, where f is the measuring frequency. The value of ϕ, calculated using the above formula was found to be 0.005, similar to those of canonical metallic spin glass systems [26].

Unlike T_{sg}, T_a does not show any such sensitivity to the frequency of excitation field which further confirms the change in dominant magnetic phase of the system across T_a as discussed in Sec. 3.4.1.

The presence of superlattice peaks from the B2 phase in the XRD pattern shown in Fig. 3.1 showed the formation of ordered phase of FeAl in the disordered background and the resulting inhomogeneity in the sample. As a consequence, the total magnetization of the sample comprised contributions from both the ordered clusters and the disordered background corresponding to the respective B2 and A2 phases. The A2 phase turned into a spin glass below T_{sg} because of magnetic frustrations resulting from competing magnetic exchange interactions present in the system. The descriptions of magnetic exchange interaction parameters calculated from first-principles theories are given in later sections of this chapter. Therefore, the magnetization of the A2 phase decreased with lowering of temperature below T_{sg} due to gradual freezing of spin clusters [26]. The magnetic response of the ordered clusters corresponding to the B2 phase, on the other hand, was paramagnetic with *1/T* (Curie) magnetization dependence which continued to increase with lowering of temperature and became the dominant contribution at low enough temperatures resulting in the upturn in magnetization. When the strength of applied magnetic field is increased, the spin freezing temperature, T_{sg}, of a spin glass phase is known to shift towards lower temperatures, whereas the paramagnetic contribution becomes stronger and pushes T_a towards higher temperatures region. The opposite movements of T_{sg} and T_a with applied magnetic field eventually destroyed the peak and dip structure in the magnetizations when measured at a higher value of H.

3.5 Theoretical analysis

The observed magnetic behavior of inhomogeneously disordered Fe:Al alloy has been modeled in this section using a density functional based ab-initio electronic structure calculation supplemented with Monte-Carlo simulation for getting a better understanding of the magnetic properties of such systems.

3.5.1 Density of states

Electronic structure of Fe:Al was calculated using self-consistent ASR within TB-LMTO. A brief description of the underlying theories has been outlined in Sec. 2.2.3.2. The choice of TB-LMTO [82] as a base methodology stemmed from the fact that the disorder fluctuations in the alloys are local and a tight-binding basis is most suitable in describing such disorder. The disorder in the system was realized using ASR [83] which goes beyond single-site mean field approximations like CPA in describing local fluctuations such as short-range ordering and clustering relevant to the present case.

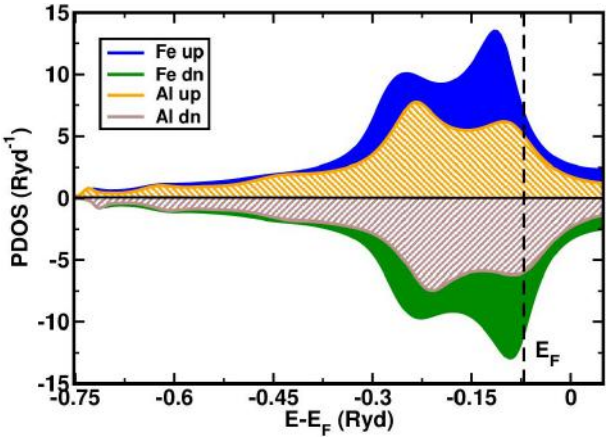

Figure 3.4: The spin-projected density of states of disordered Fe:Al alloy, projected on the Fe and Al atoms (up: spin-up DOS, dn: spin-down DOS).

The calculated spin-projected densities of states of Fe and Al atoms in disor-

dered Fe:Al alloy are shown in Fig. 3.4. Unlike ordered alloys, the DOS is rather smooth because of disorder scattering. The relatively localized *d*-electrons of Fe dominate the DOS near Fermi level whereas the more itinerant *p*-electrons of Al contribute to the base. Considerable overlap between Fe-*d* and Al-*p* bands reflects the hybridization of Fe and Al states. As can be seen from the DOS, the alloy is magnetic. Magnetic moment forms out of the itinerant electron charge density by an exchange splitting of the majority and minority spin-projected DOS, and the magnetization density integrated over the atomic spheres provides the moments associated with each sphere.

3.5.2 Magnetic exchange interaction parameters

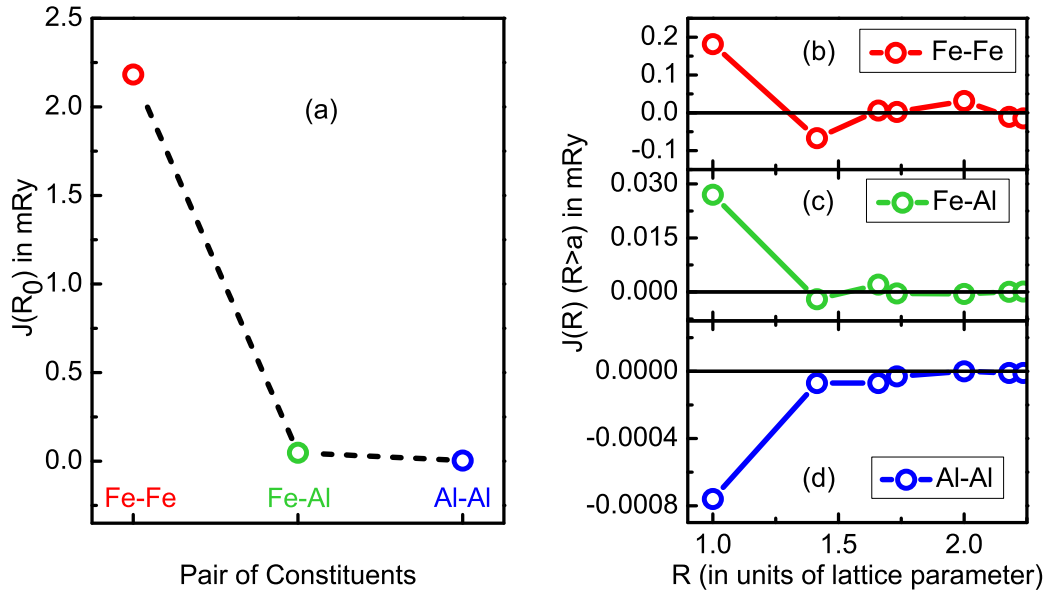

Figure 3.5: (a) The magnetic exchange energies of Fe-Fe, Fe-Al and Al-Al pairs for the dominant nearest neighbors and (b)–(d) for other neighbors in disordered Fe:Al alloy.

Magnetic exchange interactions between the constituent atomic species, Fe and Al, were calculated using the orbital peeling method [116]. The underlying theory of orbital peeling method has been discussed in Sec. 2.2.4. Nearest neighbor exchange interactions between different pairs are shown in Fig. 3.5(a) which displays the dominance of Fe-Fe exchange interaction over Fe-Al and Al-Al pairs. Figs.3.5 (b)–(d) depict

the variation of exchange energies with distance. As can be seen from the figures, these exchange interactions are rather long ranged and oscillatory which demonstrate the RKKY nature of these interactions. Magnetic Fe atoms immersed in the valance electron cloud polarize it and provide the oscillatory interaction which rapidly decays with distance due to disorder scattering. Magnetic frustration arises from such an oscillatory exchange interaction which subsequently results in a low-temperature spin glass phase.

3.5.3 Magnetization from Monte-Carlo simulation

Monte-Carlo (MC) simulation was carried out to investigate the temperature dependent magnetic behaviors of disordered Fe:Al alloy and the effects of short-range ordering. The MC simulation was carried on the Ising Hamiltonian onto which the GPM model [114] maps the problem of magnetic ordering of an alloy system:

$$\mathscr{H} = -\frac{1}{2}\sum_{\mathbf{R}_i}\sum_{\mathbf{R}_j} J^{QQ'}\big(|\mathbf{R}_i - \mathbf{R}_j|\big) S_{\mathbf{R}_i} S_{\mathbf{R}_j} \tag{3.1}$$

where $J^{QQ'}\big(|\mathbf{R}_i - \mathbf{R}_j|\big)$ is the magnetic exchange interaction between the constituent atomic species Q and Q' situated at the sites $\mathbf{R}_i$ and $\mathbf{R}_j$, $S_{\mathbf{R}_i}$ takes the values ± 1 according to whether the moment situated at the site $\mathbf{R}_i$ is oriented along the global quantization direction or opposite to it. The magnetic exchange interaction parameters obtained from the first-principles theories and described in the previous section were used as the input parameters in the MC simulation. Metropolis algorithm [151] with single spin flip dynamics was used to perform MC simulation. First 25000 steps were discarded to thermally stabilize the system and measurements were performed in the next 250000 steps. MC simulations were carried out on a BCC lattice of volume $[(L-1)a]^3$ where a and L are respectively the inter-atomic distance along the cube sides and length of the cube sides.

The special quasi-random structure (SQS) [84], described in Sec. 2.2.3.3, was

used to represent the disordered phase of A2 Fe:Al in MC simulation. The SQS method of structure generation is more capable of dealing with the inhomogeneities like short-range ordering and clustering than the standard method of randomly distributing atoms on the lattice sites and averaging over multiple configurations (we will designate this method as RS). However, before proceeding with SQS, the results obtained from SQS were tested against the results of standard RS method for the homogeneous disordered case to check the applicability of SQS.

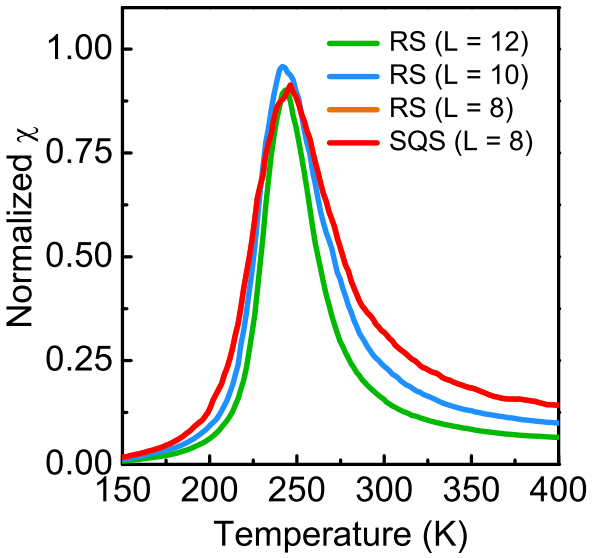

Figure 3.6: Temperature variations of magnetic susceptibilities of disordered Fe:Al alloy obtained from MC simulations using RS and SQS.

Magnetic susceptibilities of A2 Fe:Al, obtained from MC simulations using SQS and RS, are shown in Fig. 3.6 which depicts a fairly well agreement between the two methods. In a disordered alloy, MC simulation using SQS is computationally cheaper than with standard RS for which the required time or computational resource scales with the number of configurations considered in the simulation. In addition, a desired structure like inhomogeneously disordered alloy with short-range ordering and clustering can be generated by optimizing the multisite correlation functions in SQS. Therefore, if not otherwise mentioned, both homogeneously and inhomogeneously disordered Fe:Al alloys were represented by SQS ($L = 8$) in the MC simulations presented

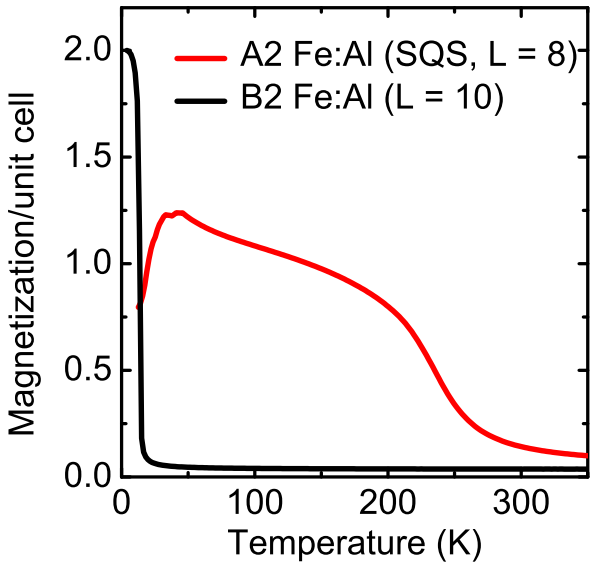

Figure 3.7: MC simulated temperature variation of magnetization of A2 and B2 Fe:Al alloys.

in remaining part of this chapter.

MC simulated temperature variations of magnetization of A2 and B2 Fe:Al are shown in Fig. 3.7. The B2 Fe:Al alloy was found to be paramagnetic as predicted by first-principles density functional theories [123, 128, 132] and a ferromagnetic transition occurred only at a very low temperature $\approx T_a^{ZFC}$, the temperature where the anomalous upturn was found in the ZFC magnetization measured at $H = 25$ Oe. Temperature variation of magnetization of A2 Fe:Al showed a paramagnetic to ferromagnetic transition at $T_C \approx 250$ K (which can be seen from the peak in the magnetic susceptibilities shown in Fig. 3.6).

The XRD pattern shown in Fig. 3.1 showed the presence of short-range ordering in our experimentally prepared specimen of disordered Fe:Al and the formation of such inhomogeneities have been reported in earlier studies also [135, 136, 150]. Therefore, the effects of such inhomogeneities on the magnetic transition temperature and the temperature dependent magnetization behavior are investigated next. First, we took a rather crude approach where it was assumed that there is no correlation between the

precipitated ordered clusters and the disordered background. The total magnetization of an inhomogeneously disordered alloy in such a scenario is a proportional mixture of the two phases:

$$M_{\text{total}} = yM_{\text{ord}} + (1-y)M_{\text{disord}} \tag{3.2}$$

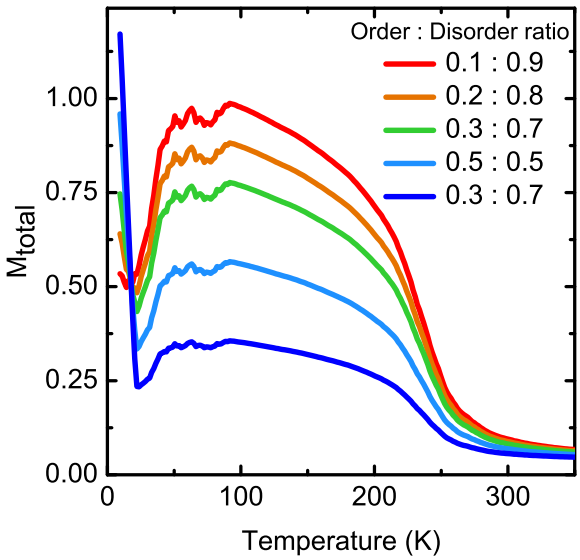

Figure 3.8: Temperature variation of total magnetization M_{total} at different mixing ratios for the independent mixture of ordered and disordered phases of Fe:Al alloy.

where y is the fraction of ordered phase. Fig. 3.8 shows the variation of M_{total} with temperature. The characteristic behaviors of M_{total} in the region between T_C and T_{sg} matched well with the experimentally observed magnetization behavior. The upturn in magnetization at low temperatures increased with the increase of the fraction of ordered phase which substantiates that magnetic response of the ordered clusters is the reason behind the observed upturn in experimentally measured magnetization below T_a. However, surprisingly T_C was not significantly affected by the variation of the ratio of ordered and disordered phases. This drawback of the model primarily arises from the fact there is a lack of correlation between the magnetization of ordered and disordered phases, and hence one does not affect the behavior of other. T_C is the property of the disordered phase and consequently remained unaffected by the increase of the fraction

of ordered phase.

For a more accurate description of the effects short-range ordering and clustering on the magnetic properties of Fe:Al alloy, MC simulation was carried out with SQS containing a desired type and amount of inhomogeneity. Inhomogeneities like short-range ordering and clustering can be incorporated into SQS in a controlled fashion by optimizing the multisite correlation functions of the structure to the desired target. Warren-Cowley short-range order parameter α [8, 9] describes the nature of inhomogeneities present in a system and can be expressed in terms of pair correlation function as described in the Sec. 2.2.3.3. SQS with *negative* value of α (i.e., $\alpha < 0$) indicates that short-range ordering is present in the structure and SQS with *positive* value of α (i.e., $\alpha > 0$) have clusters of like atoms built into them.

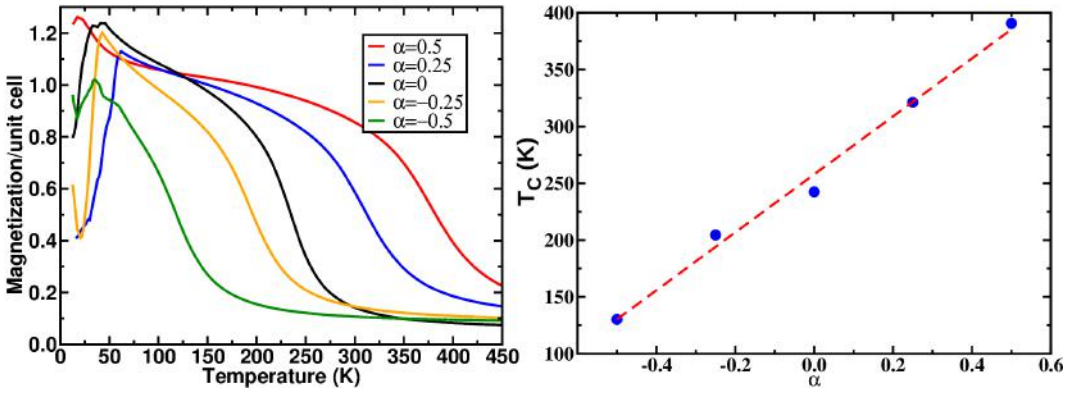

Figure 3.9: (Left panel) MC simulated temperature variation of magnetization of Fe:Al alloy for different values of short-range order parameter α. (Right panel) Variation of paramagnetic to ferromagnetic transition temperature T_C with α. The dashed line is given as guide to the eye for a straight line.

MC simulated temperature variation of magnetization of A2 Fe:Al for different values of α is shown in Fig. 3.9(Left panel) which displays a good agreement with experimentally observed magnetization behavior. The variation of T_C with α is shown in Fig. 3.9(Right panel) which depicts that T_C varies almost linearly with α. T_C gradually decreases as the system moves from the state of clustering to the state of short-range ordering through a perfectly disordered state. Although, magnetization decreased below T_{sg} in both homogeneously and inhomogeneously disordered structures, low temper-

ature upturn in magnetization was present only in the structures with *negative* values of α. This confirms that while the spin glass behavior is a property of the disordered background, arising from magnetic frustrations due to the presence of competing magnetic exchange interactions in the system, the upturn in low temperature magnetization originates from the ordered clusters present in the system.

The experimental results presented in Sec. 3.4.1 have indicated that magnetization behaviour of Fe:Al changes drastically with the variation of the strength of applied magnetic field. Therefore, MC simulation was carried out to investigate the effect of applied magnetic field. In presence of an applied magnetic field h, the Hamiltonian of Eq. 3.1 takes the form:

$$\mathscr{H} = -\frac{1}{2}\sum_{\mathbf{R}_i}\sum_{\mathbf{R}_j} J^{QQ'}(|\mathbf{R}_i - \mathbf{R}_j|)S_{\mathbf{R}_i}S_{\mathbf{R}_j} - h\sum_{\mathbf{R}_i} S_{\mathbf{R}_i} \tag{3.3}$$

MC simulation was carried out for the B2 Fe:Al and for homogeneously and inhomogeneously disordered A2 Fe:Al. Temperature variation of magnetization of these structures for different values of α and h are shown in Fig. 3.10. The magnetization of B2 Fe:Al increased with the applied magnetic field as more and more spins get oriented along the field direction. In the homogeneously and inhomogeneously disordered A2 Fe:Al

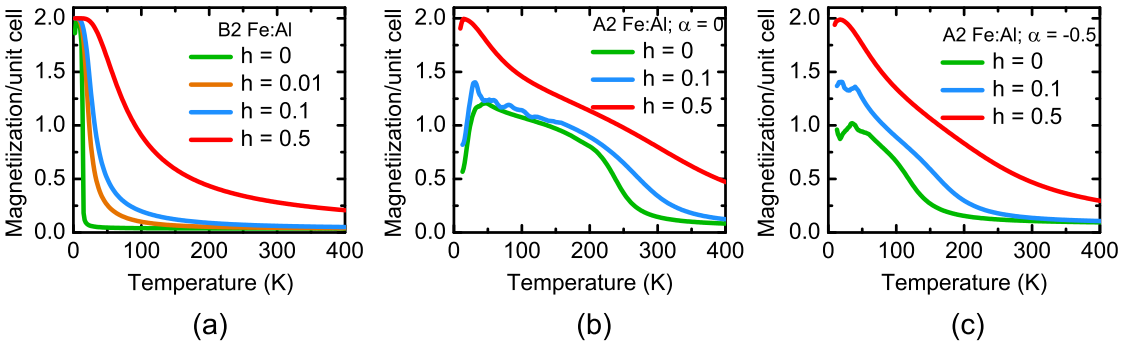

Figure 3.10: MC simulated temperature variation of magnetization of (a) an ordered B2 structure, (b) a homogeneously disordered structure ($\alpha = 0$), and (c) a sample with short-range ordering ($\alpha = -0.5$).

alloys (i.e., structures corresponding to α = 0 and α = -0.5, respectively), along with increasing the magnetization, external magnetic field drove T_{sg} towards lower temperatures similar to our experimental observation. The spin freezing temperature (T_{sg}) gradually decreased with increasing h similar to a canonical metallic spin glass and at high enough magnetic field completely suppresses the spin glass phase. The magnetic states around T_{sg} and T_a are complex due to the interplay between the paramagnetic response of the B2 Fe:Al phase and the spin glass phase originating from the A2 Fe:Al.

3.6 Conclusions

In this chapter, magnetic properties of inhomogeneously disordered Fe:Al alloy has been discussed. Experimentally observed magnetization behavior has been analyzed by modeling the inhomogeneous disorder using SQS and calculating the magnetic properties using Monte-Carlo simulation. Experimental and theoretical investigations showed that while a spin glass phase arises from the disordered background, the presence of short-range ordering gives rise to a very low temperature magnetically ordered phase. Magnetic transition temperatures of the system are also found to be strongly affected by the presence of short-range ordering in the sample. The sensitivity of the magnetic behavior to the local inhomogeneities, which depend on the preparation conditions of the specimens, results in interesting magnetic behavior and is the reason behind the discrepancies among the experimental results quoted by different groups.

4 Magnetic and Transport Properties of Disordered $Fe_{1-x}Al_x$ Alloys

4.1 Introduction

In the previous chapter, we have discussed the magnetic properties of disordered equiatomic Fe:Al alloy and how the presence of short-range ordering affects its magnetic behaviors. As we have discussed earlier, the disordered phase of Fe:Al alloy has cubic A2 structure, while the ordered phase has cubic B2 structure. The ordered B2 phase is the lowest energy structure forms in the thermodynamic equilibrium conditions and the disordered A2 phase can be obtained by various disordering procedures of the ordered B2 phase like rapid quenching from high temperatures and high-energy ball milling. In the $Fe_{1-x}Al_x$ phase diagram [42–45] cubic structures form up to $x \approx 0.60$. Pure iron at room temperature has A2 phase. As one mixes Al into Fe, the A2 phase of Fe extends up to $x \approx 0.23$. With further increase of Al concentration, this disordered BCC solid solution changes to ordered arrangements of the constituent atoms. When the alloys up to $x \approx 0.35$ are annealed at low temperature (below ≈ 800 K), cubic DO_3 phase forms. However, when annealed at higher temperatures cubic B2 phase forms. Above $x \approx 0.35$ and below $x \approx 0.60$, the B2 phase is the lowest energy structure in thermodynamic equilibrium conditions. Similar to the equiatomic concentration, the disordered A2 phase can be obtained by disordering the ordered phases at other concentrations also [46–49, 136, 152–164]. One intriguing property of this system in the disordered A2 phase is the dilution behavior of Fe moment as one increases the Al concentration

[46–50, 136]. With increasing Al concentration, hybridization between Fe and Al electronic states increases resulting in a gradual dilution of Fe moment [125, 129], and the dilution behavior follows a simple law $d\mu_{Fe}/dx = \text{Const.}$ i.e., Fe moment falls linearly with increasing Al concentration. However, this simple dilution law exits only below $x \approx 0.25$ beyond which μ_{Fe} falls faster. In addition, the variation of μ_{Fe} as well as the magnetic transition temperature (paramagnetic to ferromagnetic transition) reported by various researchers vary widely in the Al compositions above $x \approx 0.25$. [46, 47]. The variation of lattice parameter reported in earlier studies also showed anomalous behaviour [46–50, 132, 136, 150, 158]: the lattice parameter first increased linearly with Al concentration up to $x \approx 0.25$ and with further increase of Al concentration, lattice parameter increment deviated from linearity and in some studies it was found that lattice parameter even decreased with increasing Al concentration. In addition, similar to μ_{Fe}, the lattice parameter values also varies widely among various reports.

The point to note here is that these anomalous behaviors of μ_{Fe} and lattice parameter occur above $x \approx 0.25$ where one can obtain the disordered A2 phase only via disordering of the ordered structures by non-equilibrium procedures. In these disordering procedures, complete destruction of the ordered structure is very difficult and the short-range orderings are very likely to be present in the samples. In the previous chapter, we have shown that the presence of such short-range ordered structure strongly influences the magnetic behavior of the disordered phase at equiatomic concentration. Therefore, in this chapter we have investigated whether the presence of short-range ordering or the amount of disordering of the sample is also connected to the various anomalous behavior reported as a function of Al concentration in this alloy system.

4.2 Sample preparation and composition analysis

The preparation and annealing of the polycrystalline ingot of the composition $x = 0.5$ in the series $Fe_{1-x}Al_x$ ($0.25 \leq x \leq 0.55$) has been already described in Sec. 3.2. The polycrystalline ingots of other compositions in the series were prepared in the same fashion. The compositions of the prepared polycrystalline ingots obtained from EPMA analysis are listed in Table 4.1 which shows that the prepared ingots have compositions close to the target value with good homogeneity.

Table 4.1: Compositions of the prepared polycrystalline ingots of $Fe_{1-x}Al_x$ obtained from EPMA analysis

x	Obtained concentrations (at%)	
	Fe	Al
0.25	76.1(5)	23.9(5)
0.30	71.7(4)	28.3(4)
0.35	66.0(4)	34.0(4)
0.40	61.9(6)	38.1(6)
0.45	55.1(6)	44.9(6)
0.50	51.3(2)	48.7(2)
0.55	48.2(7)	51.8(7)

4.3 Crystal structure

Room temperature XRD patterns measured using powdered specimens in a PANalytical X'pert PRO^{TM} powder diffractometer with Mo-Kα X-ray source (wavelength $\lambda = 0.71$ Å) are shown in Fig. 4.1. (h k l) indices of all peaks are also listed in the graph. As discussed in the previous chapter for the $x = 0.5$ composition, (1 0 0), (1 1 1) and (2 1 0) are the superlattice reflections from the ordered B2 phase and all other peaks correspond to a BCC structure which confirms the formation of the disordered

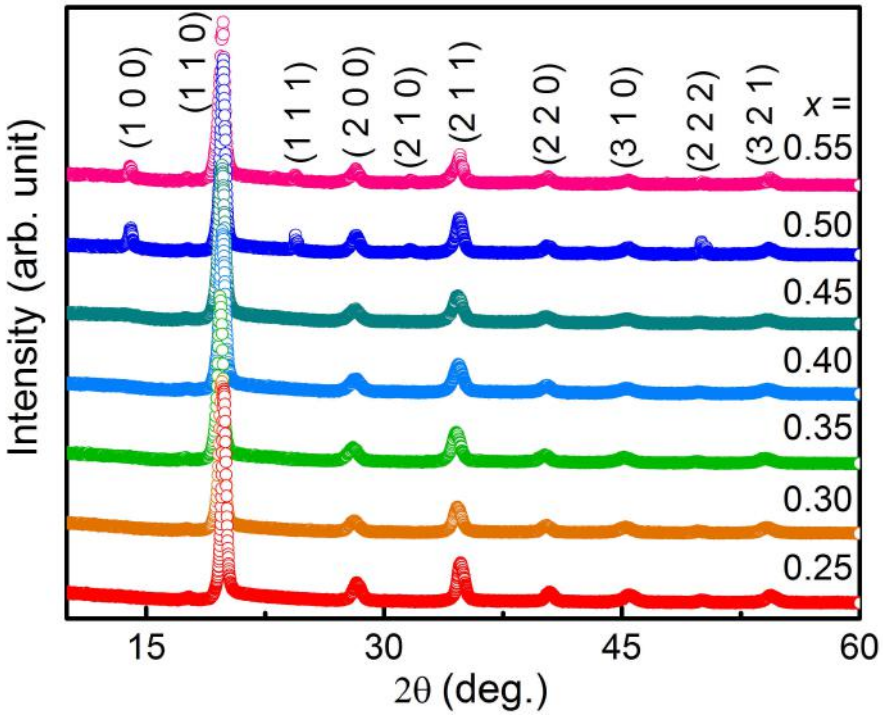

Figure 4.1: Room temperature XRD patterns of $Fe_{1-x}Al_x$ alloys measured using Mo-Kα X-ray source.

A2 phase. The superlattice reflections are visible only in the compositions $x = 0.5$ and $x = 0.55$ which indicate that the higher Al compositions tend to have more short-range ordering. In the Fe-rich compositions, from $x = 0.25$ to $x = 0.45$, no such superlattice peaks are visible which indicates that only the A2 phase was formed in these alloys.

Fits of the XRD patterns obtained from Rietveld refinements are shown in Figs. 4.2(a)–(g) and the obtained parameters are listed in Table 4.2. Fig. 4.3 shows the variation of lattice parameter with Al concentration. As the Al concentration increases, lattice parameter increases up to $x = 0.35$. However, with further increase of Al concentration, lattice parameter decreases. The anomalous variation of lattice parameter with Al concentration has been reported in earlier studies also [46–50, 132, 136, 150, 158]. Combining resistivity studies, plausible explanation of this anomalous behavior has been given in the later sections of this chapter.

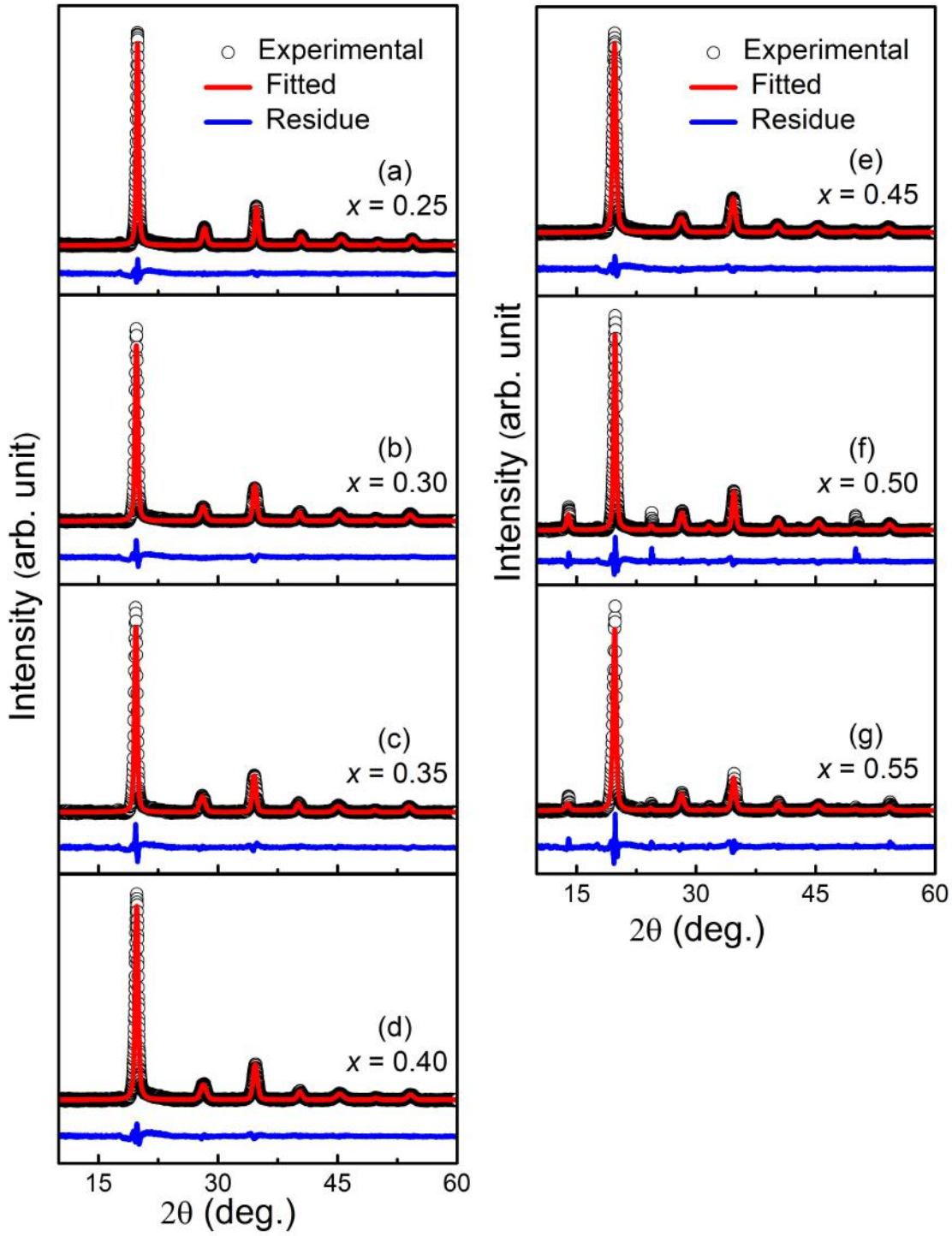

Figure 4.2: (a)–(g) Rietveld refinement fits of the room temperature XRD patterns of $Fe_{1-x}Al_x$.

Table 4.2: Rietveld refinement result of the XRD patterns of $Fe_{1-x}Al_x$ alloys. U_{iso} is the isotropic thermal parameter.

Al concentration (x)	a (Å)	U_{iso} (Å^2)	χ^2
0.25	2.90606(7)	0.0112(2)	4.9
0.30	2.9222(1)	0.0093(3)	3.3
0.35	2.9291(1)	0.0119(3)	3.3
0.40	2.91991(8)	0.0145(2)	3.0
0.45	2.92126(8)	0.0160(2)	2.6
0.50	2.91226(8)	0.0132(3)	4.8
0.55	2.9134(1)	0.0214(5)	4.0

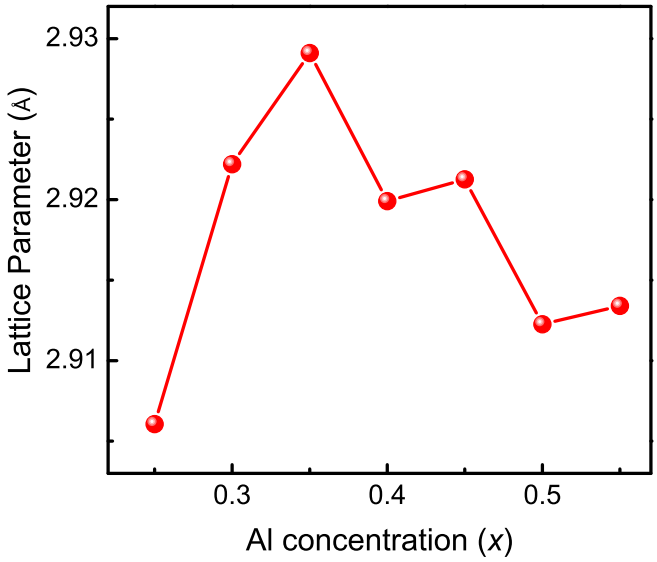

Figure 4.3: Variation of lattice parameter of $Fe_{1-x}Al_x$ with Al concentration.

4.4 Resistivity

Temperature variations of resistivities of $Fe_{1-x}Al_x$ alloys in the form $\rho(T)/\rho(T = 300\ \text{K})$ are shown in Fig. 4.4. The values of $\rho(T = 300\ \text{K})$ are listed in Table 4.3. Although metallic behaviour is evident for the entire composition range studied here, the resistivity values and temperature dependences of resistivity show intriguing behaviour as a function of composition and are discussed below.

At high temperature, electron-phonon scattering contribution to the resistivity

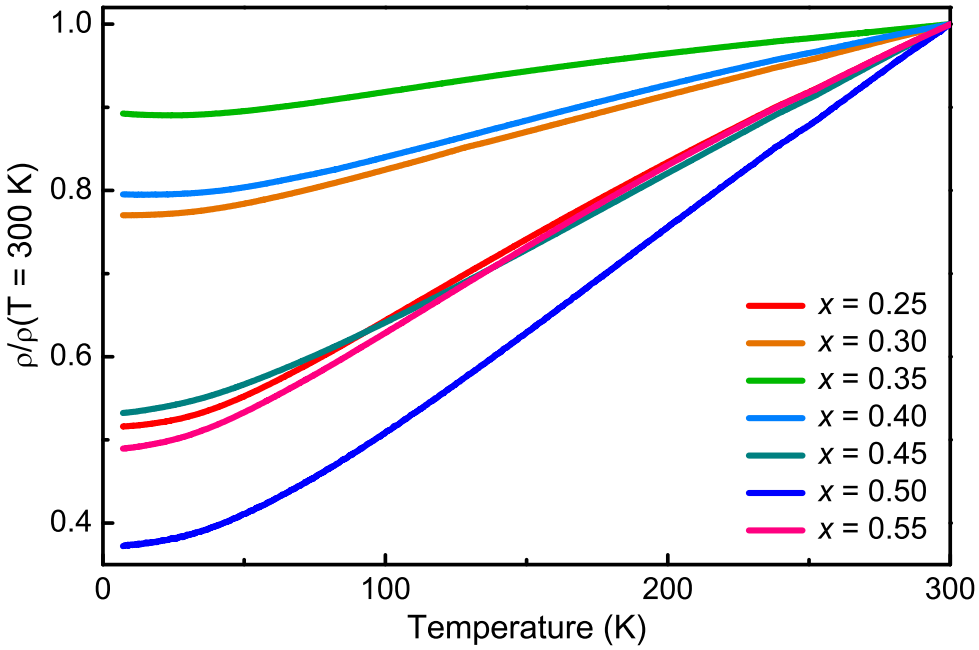

Figure 4.4: Electrical resistivities of $Fe_{1-x}Al_x$ alloys as a function of temperature.

Table 4.3: Resistivity values of $Fe_{1-x}Al_x$ at $T = 300$ K.

Al concentration (x)	$\rho(T = 300\text{K})$ ($\mu\Omega$-cm)
0.25	197(7)
0.30	213(7)
0.35	320(11)
0.40	274(8)
0.45	172(5)
0.50	127(4)
0.55	149(4)

is the dominant term for which resistivity is expected to increase linearly with temperature. However, resistivities of $Fe_{1-x}Al_x$ deviates from linearity at high temperature. This tendency towards saturation is typical for highly resistive alloys. Correspondingly, as can be seen from Table. 4.3, the resistivities of $Fe_{1-x}Al_x$ alloys are very high which is also an indication of the highly disorder nature of the samples. The $x = 0.35$ composition has the highest resistivity and its temperature dependence deviates from linearity roughly above 150 K. As the resistivity of the alloys decreases, the temperature at which the temperature dependence deviates from linearity also increase. The $x = 0.50$ compo-

sition has the lowest resistivity and it shows linear temperature dependence up to 300 K.

The variation of resistivity as a function of Al concentration shows very interesting behavior. The resistivity values $\rho(T = 10\ \text{K})$, $\rho(T = 300\ \text{K})$ and the residual resistivity ratio (RRR) $\rho(T = 10\ \text{K})/\rho(T = 300\ \text{K})$ as a function of Al concentration are shown in Fig. 4.5. At very low temperature, inelastic scatterings of electrons die out, and resistivity of metals and alloys becomes nearly temperature independent with resistivity value determined by the disorder present in the system. The larger the disorder, larger is the value of temperature independent part of the resistivity. Residual resistivity ratio (RRR) is also a measure of disorder in the system: as the disorder in the system increases, RRR decreases. Therefore, both $\rho(T = 10\ \text{K})$ and RRR indicate the amount of disordering of the samples. We found that initially with increasing Al concentration they increase up to $x = 0.35$ and with further increase of Al concentration they decrease. This behavior indicates that the composition $x = 0.35$ has the highest

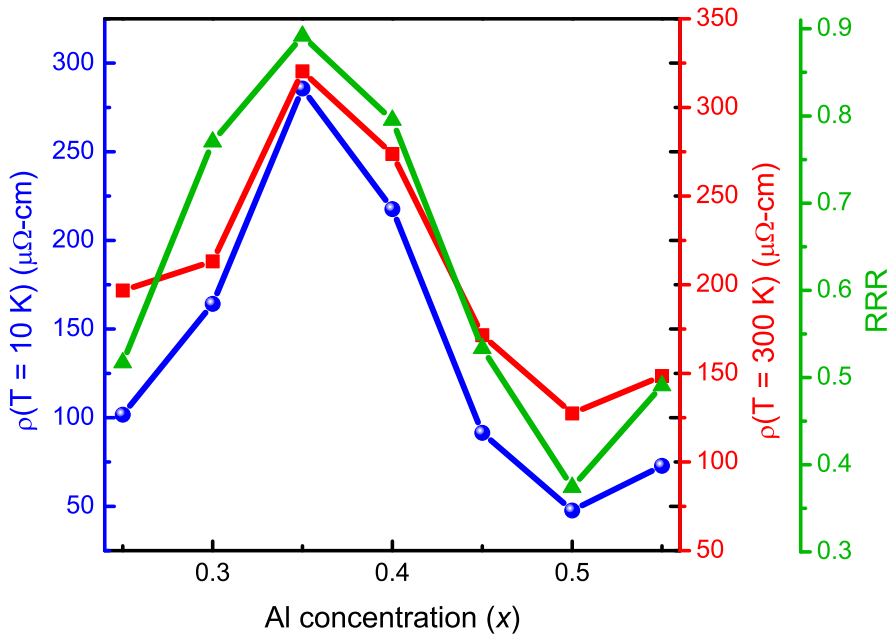

Figure 4.5: Resistivity values of $Fe_{1-x}Al_x$ alloys at $T = 300$ K and $T = 10$ K and residual resistivity ratio (RRR) at $T = 10$ K as a function of Al concentration.

amount of disorder and as one moves away from this composition ordering tendency increases. This ordering tendency of $Fe_{1-x}Al-x$ alloys as one moves away from the $x = 0.35$ composition is also clearly indicated by the presence of superlattice reflections, which evidence the formation of short-range ordering, in the XRD patterns of the composition $x = 0.50$ and 0.55. This is surprising because one expects that for BCC A2 structure with two sites per unit cell disordering should be maximum at the equiatomic composition where both Fe and Al atoms have equal occupational probabilities. One might argue that the low temperature upturn of the resistivity (shown in Fig. 4.6) of the compositions $x = 0.30, 0.35$ and 0.40 causes the observed behaviour of $\rho(T = 10$ K) and RRR as a function of Al concentration. However, the upturn is maximum in the composition $x = 0.35$ and the difference between resistivities at the minimum and at $T = 10$ K is less that 1 μΩ-cm whereas the difference of resistivity values as a function of Al concentration is even larger than 50 μΩ-cm.

The enlarged view of the low temperature part of $\rho - T$ curves of the compositions $x = 0.30, 0.35$ and 0.40 are shown in Figs. 4.6(a)–(c). The inset graphs show the temperature variation of the temperature coefficient of resistivity (TCR) defined as $\frac{1}{\rho(T=300\text{K})}\frac{d\rho}{dT}$. As can be seen from the figure, a resistivity minimum appears in these compositions and consequently, TCR also goes to zero. This is another indication of highly

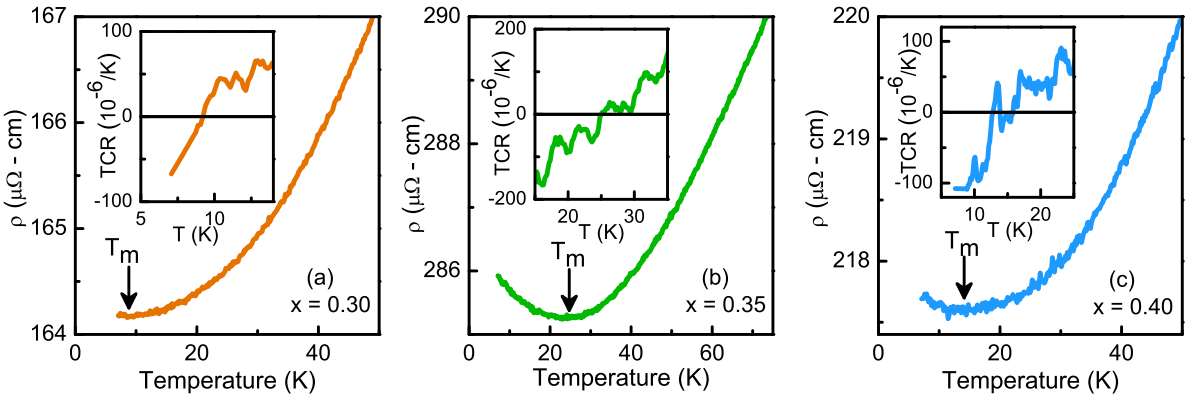

Figure 4.6: Enlarged view of the temperature variation of resistivity of $Fe_{1-x}Al_x$ in the low temperature region. The insets show the variation of TCR $\left(= \frac{1}{\rho(T=300\text{ K})}\frac{d\rho}{dT}\right)$ with temperature.

disorder nature of these samples. As discussed in Sec. 1.3.2, in highly disordered materials resistivity minimum appears due to quantum corrections in resistivity (due to weak localization (WL) and enhanced electron-electron (EEI) interactions). The temperature T_m at which resistivity minimum appears is the highest in the composition $x = 0.35$ ($\approx$ 25 K). T_m decreases as we vary the composition from $x = 0.35$: values of T_m at $x = 0.30$ and 0.40 are $\approx$ 9 K and $\approx$ 15 K, respectively. Other compositions do not show this resistivity minima in our measured temperature range 4 – 300 K. These observations also confirm that the composition $x = 0.35$ has the highest amount of disorder and disordering decreases on both sides of this composition.

Another striking observation is the similarity of the variation of lattice parameter (shown in Fig. 4.3) with resistivity values $\rho(T = 10\text{ K})$, $\rho(T = 300\text{ K})$) and residual resistivity ratio (RRR) (shown in Fig. 4.5). This can be understood in the following way. Previous reports indicated that disordering of the ordered B2 structure causes the increase of lattice parameter [129, 152, 153, 155–157, 162], for example, the disordered A2 structure has almost 1% larger lattice parameter than the ordered B2 structure at $x = 0.40$ [156, 162]. We found from the variations of $\rho(T = 10\text{ K})$ and RRR with Al concentration (shown in Fig. 4.5) that with increase of Al concentration disordering increases up to the composition $x = 0.35$. However, with further increase of Al concentration disordering decreases and the presence of short-range order increases. Therefore, one can see that the nature of variation of the lattice parameter with Al concentration is directly correlated with the amount of disorder present in the sample. According to the resistivity measurements, disordering increases up to the composition $x = 0.35$ and as the disordered phase has higher lattice parameter than the ordered phase, lattice parameter increases. Above the composition $x = 0.35$, disordering gradually decreases and so the lattice parameter also decreases.

The variation of the lattice parameters obtained from the Rietveld analysis of the XRD patterns with Al concentration is shown in Fig. 4.7 along with the lattice

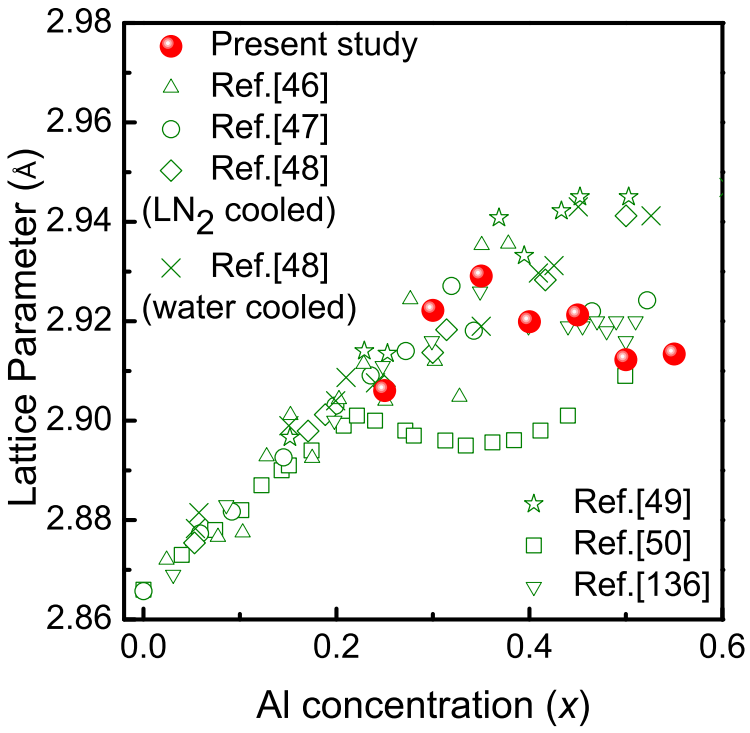

Figure 4.7: Variation of lattice parameter of $Fe_{1-x}Al_x$ alloys with Al concentration. The filled circles are the lattice parameters we obtained from the Rietveld analysis of XRD patterns and others are data reported in earlier studies by various researcher.

parameters reported in earlier studies. It can be seen from the figure that lattice parameter in all the reports increases steadily up to $x \approx 0.25$ and above that reported lattice parameter values varies widely among the different reports. Incidentally, the disordered A2 structure is the lowest energy configuration for $Fe_{1-x}Al_x$ up to $x \approx 0.23$ and above this concentration, crystal structure heavily depends on the heat treatments and preparation procedures [42–45]. Above $x \approx 0.23$, ordered DO_3 structure (Fe_3Al; space group number and symbol are 225 and $Fm\bar{3}m$, respectively) forms when the alloys are annealed at temperatures below $\approx$ 800 K and ordered B2 structure forms when they are annealed at temperatures higher than $\approx$ 800 K. Above the Al concentration $x \approx 0.23$, the disordered A2 structure can only be obtained through non-equilibrium preparation procedure like cold working, high-energy ion-irradiation, rapid quenching from high temperature, high-energy ball milling, plastic deformations etc. [46–49, 136, 152–164]. However, as the thermodynamical equilibrium phase has ordered structure,

the disordering or the presence of ordered structure in the disordered background depends on the disordering route taken. Various disordering procedures cause the varying amounts of disordering, thus accounting for different lattice parameters as seen in Fig. 4.7.

The temperature variations of resistivities of $Fe_{1-x}Al_x$ were fitted with contributions from ρ_0, ρ_{ph}, and ρ_{mag}: $\rho(T) = \rho_0 + \rho_{ph}(T) + \rho_{mag}(T)$. ρ_0 is the temperature independent part of the resistivity that arises because of the scattering of electrons from defects and disorder as discussed above. ρ_{ph} is the temperature dependent resistivity due to the inelastic electron-phonon scattering of electrons. The temperature variation of ρ_{ph} for $3d$ transition metals and alloys is given by Bloch-Wilson formula [165, 166]:

$$\rho_{ph}(T) = A_{ph}\left(\frac{T}{\theta_D}\right)^3 \int_0^{\theta_D/T} \frac{x^3}{(e^x-1)(1-e^{-x})}\mathrm{d}x \tag{4.1}$$

where A_{ph} is the strength of conduction electron scattering by phonons and θ_D is the Debye temperature. The magnetic part ρ_{mag} arises due to the exchange interaction between the conduction electrons and more localized $3d$ electrons. The temperature dependence of ρ_{mag} depends on the nature of the low temperature magnetic state. For a ferromagnetic (FM) system, the spin wave description gives [167]:

$$\rho_{mag}(T) = A_{mag}^{FM} T^2 \tag{4.2}$$

where A_{mag}^{FM} is the strength of conduction electron scattering by spin-wave disorder. For a spin glass system, below the spin freezing temperature T_{sg}, ρ_{mag} is given by [26, 27, 168]

$$\rho_{mag}(T) = A_{mag}^{sg} T^{3/2} \tag{4.3}$$

where A_{mag}^{sg} is the strength of diffusive spin excitations.

At lower temperatures, the electron-phonon scattering becomes less and con-

sequently ρ_{ph} is also very small. Then, the magnetic part ρ_{mag} is the dominant contribution at lower temperatures. Assuming this dominance of ρ_{mag} over ρ_{ph}, the resistivity data below 25 K were fitted considering ρ_{mag} only. As ρ_{mag} has different temperature dependence for ferromagnetic and spin glass state, this analysis can be used to infer information about the low temperature magnetic state of the samples. To check whether the specimens have ferromagnetic or spin glass phase or a mixture of ferromagnetic and spin glass phase (which is the case for the composition $x = 0.50$ as found in the previous chapter), the low temperature resistivity data below 25 K were fitted with following equations:

$$\rho(T) = \rho_0 + A^{FM}_{mag} T^2 \tag{4.4}$$

$$\rho(T) = \rho_0 + A^{sg}_{mag} T^{3/2} \tag{4.5}$$

and

$$\rho(T) = \rho_0 + A^{FM}_{mag} T^2 + A^{sg}_{mag} T^{3/2} \tag{4.6}$$

In the compositions $x = 0.30, 0.35$ and 0.40, a resistivity minimum appears at low temperatures (shown in Fig. 4.6) due to quantum corrections in resistivity as described in Sec. 1.3.2. However, after assuming these corrections, we were not able to get a clear indication of whether the low temperature magnetic states of these alloys are of ferromagnetic or spin glass characters. For other compositions, fits of resistivity data below 25 K with Eq. 4.4 and Eq. 4.5 are shown in Figs. 4.8(a)–(j). When none of equations Eq. 4.4 and Eq. 4.5 give a good fit, such as for the composition $x = 0.55$ whose low temperature magnetic state mixture is a mixture of ferromagnetic and spin glass character, Eq. 4.6 was used for fitting. In the best fit cases, the percentage fit errors are randomly scattered on both sides of the *zero*-line, while in other cases they are concave in either *positive* or *negative* sides of the *zero*-line. As can be seen from the figures, Eq. 4.4 best fits the data of Fe-rich composition $x = 0.25$ indicating its ferromagnetic character at low temperature while Eq. 4.5 best fits the composition $x = 0.45$ and substantiates that

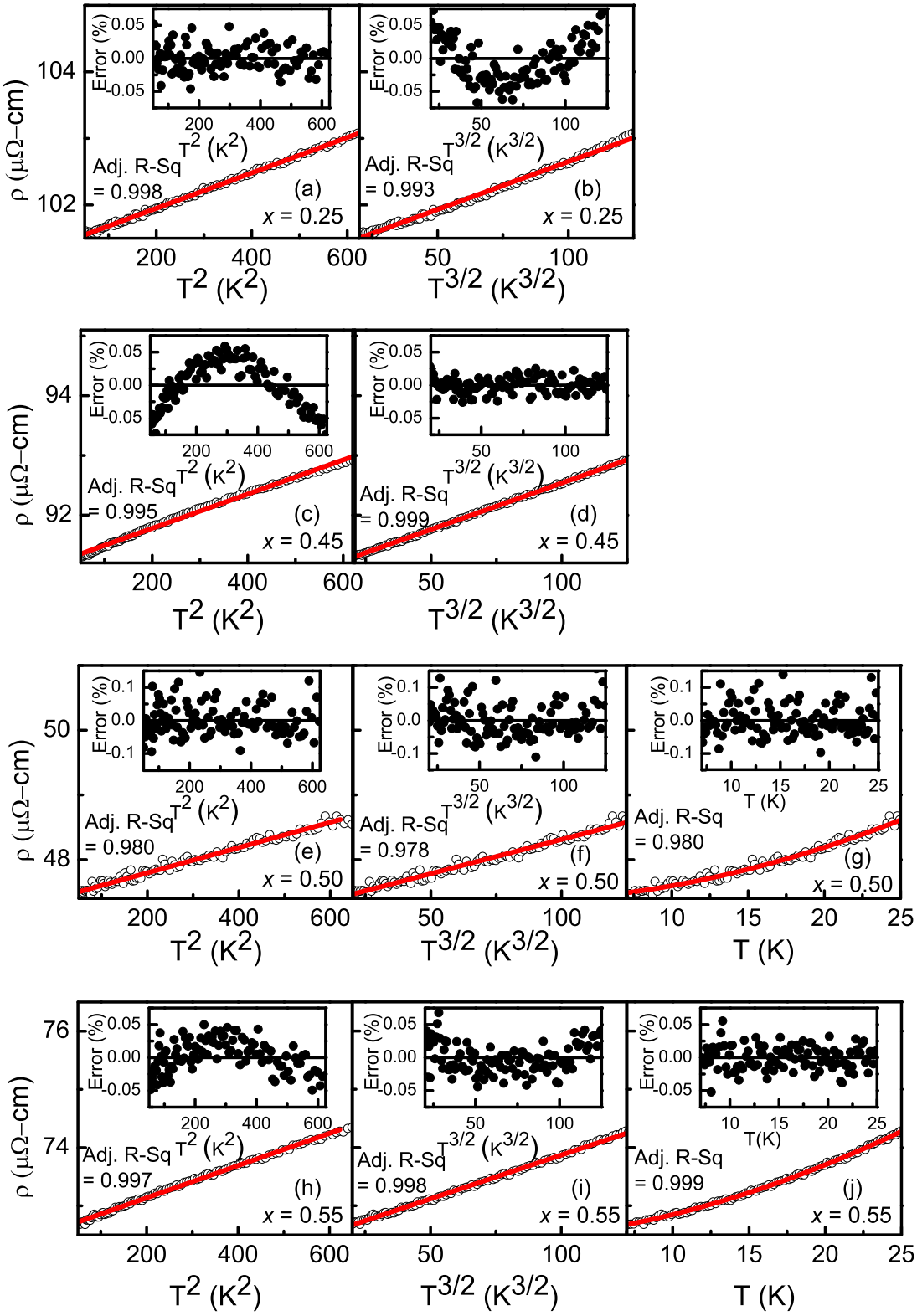

Figure 4.8: Fits of resistivity data of $Fe_{1-x}Al_x$ below 25 K with Eq. 4.4, Eq. 4.5, and Eq. 4.6.

this composition has a spin glass state at low temperature. In the composition $x = 0.55$, the percentage fit errors are concave in *positive*-side of the *zero*-line when fitted with Eq. 4.4 while concave in *negative*-side of the *zero*-line. Best fitting, i.e. random scattering of the percentage fit error on both sides of the *zero*-line, is obtained when fitted with Eq. 4.6 which indicates that the magnetic phase is a mixture of ferromagnetic and spin glass characters. As discussed in the previous chapter for the composition $x = 0.50$, this mixed magnetic phase arises due to the presence of short-range ordered clusters in the disordered background. From the XRD patterns shown in Fig. 4.1, one can see that the $x = 0.55$ composition indeed have such a inhomogeneous disorder character. Although exact judgment cannot be made about the low temperature magnetic state of the composition $x = 0.50$ from the fits due to larger scattering of data points, its mixed magnetic phase character was described from other measurements and MC simulations in the previous chapter. The $x = 0.55$ composition with similar mixed magnetic state best fits with Eq. 4.6 and therefore the low temperature resistivity data of the composition $x = 0.50$ is also expected to be best described by the same equation. The fit parameters for the best fit cases are listed in Table 4.4.

Table 4.4: Fit parameters ρ_0, A_{mag}^{FM}, and A_{mag}^{sg} obtained from the fitting of resistivity data of $Fe_{1-x}Al_x$ alloys at temperatures below 25 K. Details of the fitting are described in the text.

Al concentration (x)	ρ_0 (μΩ-cm)	A_{mag}^{FM} (μΩ-cm/K^2)	A_{mag}^{sg} (μΩ-cm/K$^{3/2}$)
0.25	101.418(4)	0.00266(1)	–
0.45	90.983(3)	–	0.01555(4)
0.50	47.36(3)	0.0014(4)	0.0030(2)
0.55	72.46(1)	0.0012(1)	0.0085(8)

Now at higher temperatures, resistivity contribution from electron-phonon scattering ρ_{ph} becomes the dominant contribution over all other contributions. Thus, resistivity data in the range between 30 K and 100 K were fitted with Bloch-Wilson formula

for phonon contribution in $3d$ metals and alloys:

$$\rho(T) = \rho_0 + A_{ph}\left(\frac{T}{\theta_D}\right)^3 \int_0^{\theta_D/T} \frac{x^3}{(e^x-1)(1-e^{-x})}\mathrm{d}x \tag{4.7}$$

Table 4.5: Fit parameters ρ_0, A_{ph}, and Debye temperature θ_D obtained from the fitting of resistivity data of $Fe_{1-x}A_x$ with Bloch-Wilson formula.

Al concentration (x)	ρ_0 (μΩ-cm)	A_{ph} (μΩ-cm/K^3)	θ_D (K)
0.25	102.40(1)	184.4(6)	282.5(6)
0.30	164.292(6)	97.8(3)	301.9(6)
0.35	284.800(7)	97.3(4)	338.6(9)
0.40	217.350(9)	137.0(8)	350(1)
0.45	92.58(2)	127.3(6)	276(1)
0.50	48.29(2)	141.2(9)	304(1)
0.55	73.70(1)	132.3(5)	260.8(8)

The fits are shown in Figs. 4.9(a)–(g) and the fit parameters are listed in Table 4.5. The obtained ρ_0 values, which are measures of amount of disorder present the samples, vary as a function of Al concentration similar to $\rho(T = 10\ \mathrm{K})$ and RRR shown in Fig. 4.5 giving further support to the scenario we discussed before that the composition $x = 0.35$ has highest amount of disorder. The value of A_{ph} has the lowest values in the composition $x = 0.35$ which is in accordance to lowest value of RRR in that composition.

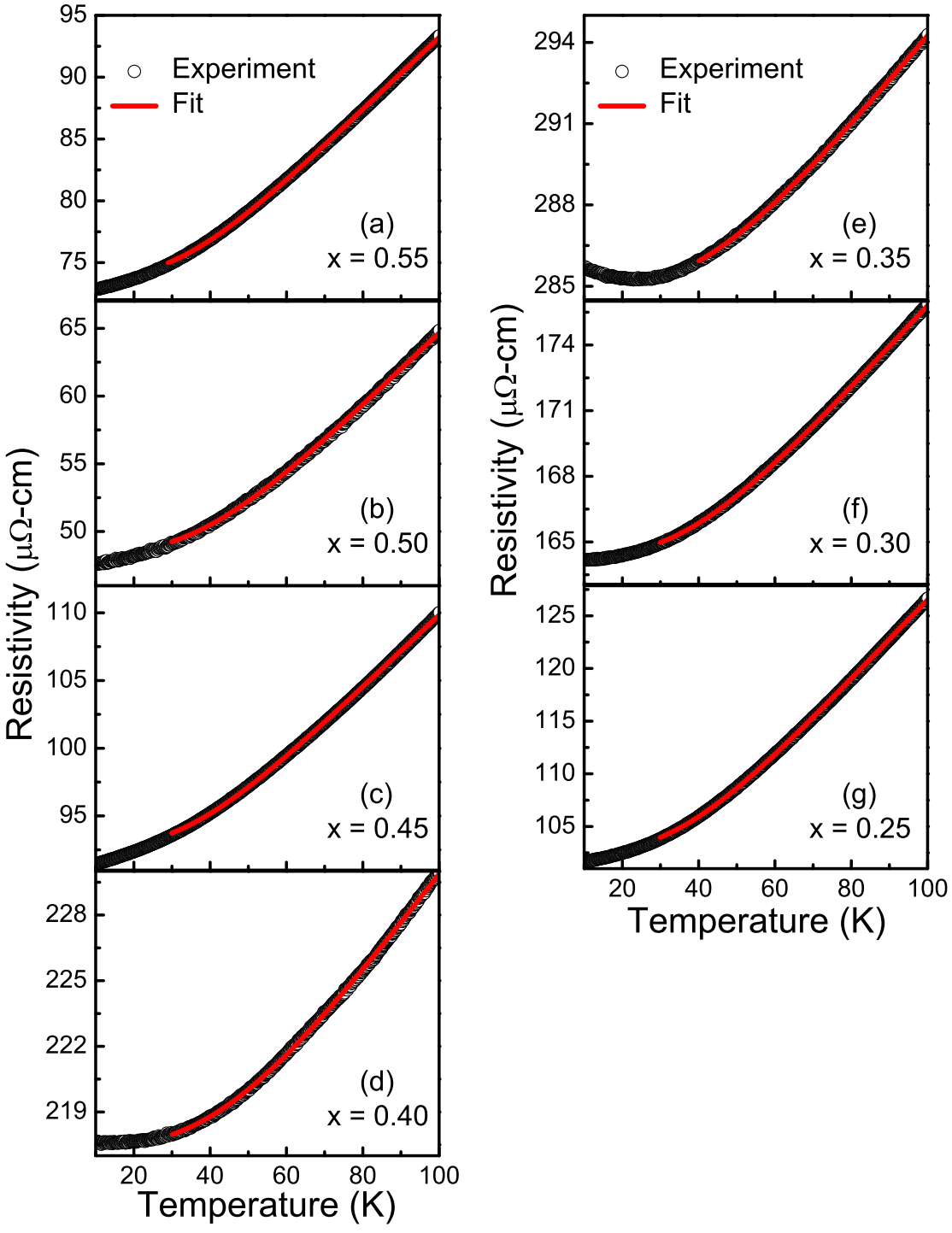

Figure 4.9: (a)–(g) Fits of resistivity data of $Fe_{1-x}Al_x$ with Bloch-Wilson formula.

4.5 Magnetic properties

Temperature dependences of magnetizations of $Fe_{1-x}Al_x$ alloys were measured using VSM and SQUID. VSM was used to measure magnetizations above room temperature while SQUID was used for measurements below room temperature. The temperature variations of magnetizations are shown in Figs. 4.10(a)–(c). The higher Al compositions, $x = 0.50$ and 0.55, were paramagnetic at room temperature, while the others, the Fe-rich compositions, were ferromagnetic at room temperature. With increasing Al concentration paramagnetic to ferromagnetic transition temperature T_C decreased gradually. Variation of T_C with Al concentrations is shown in Fig. 4.11.

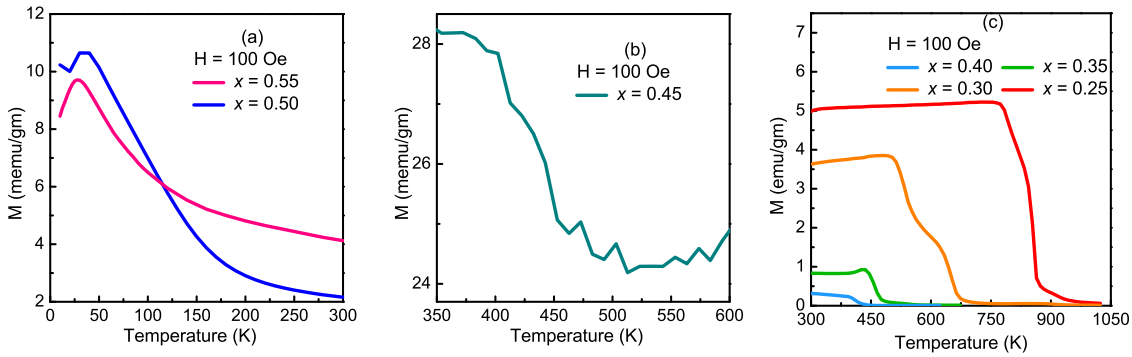

Figure 4.10: (a)–(c) Temperature variation of magnetization of $Fe_{1-x}Al_x$ alloys.

By analyzing the resistivity behaviors of the $Fe_{1-x}Al_X$ alloys in Sec. 4.4 we reached at the following conclusions about their low temperature magnetic state: (i) the Fe-rich composition $x = 0.25$ has ferromagnetic phase, (ii) the intermediate composition $x = 0.45$ has spin glass phase, and (iii) the higher Al compositions $x = 0.50$ and 0.55 have mixed phases of ferromagnetic and spin glass characters. In the previous chapter, we have shown that spin glass phase in the composition $x = 0.50$ arises due to the presence of competing magnetic exchange interactions in the disordered A2 phase while the ordered B2 phase gives rise to a very low temperature magnetically ordered state. Similar to the composition $x = 0.50$, the composition $x = 0.55$ also have short-range

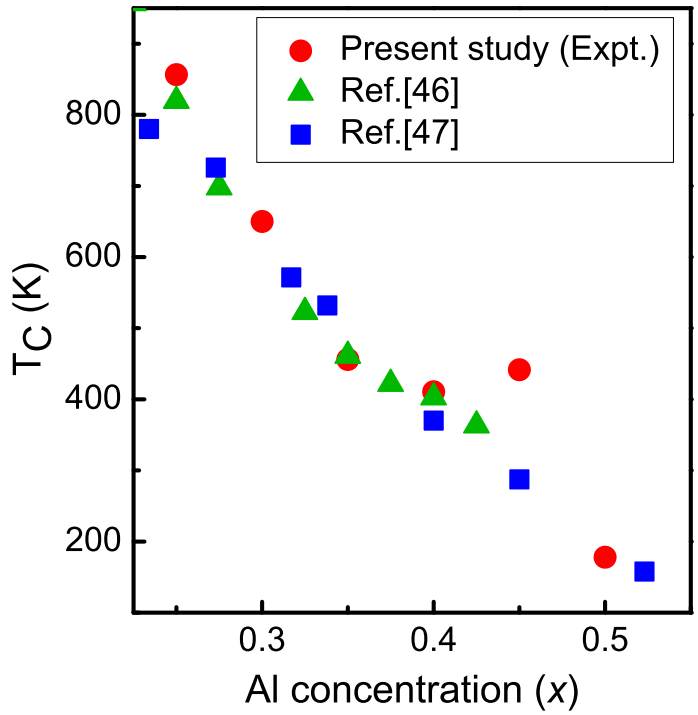

Figure 4.11: Variation of the paramagnetic to ferromagnetic transition temperature T_C of $Fe_{1-x}Al_x$ with Al concentration.

ordered clusters in the disordered background which can be seen from the XRD patterns shown in Fig. 4.1 and therefore it's low temperature magnetic state is also expected to be a mixture of ferromagnetic and spin glass phase. The superlattice reflections are clearly visible in the XRD patterns of the higher Al compositions $x = 0.50$ and 0.55 indicating the presence of short-range ordering. While no such superlattice reflections are visible in the Fe-rich compositions up to $x = 0.45$, the analysis of resistivity and XRD patterns showed that the amount of disorder increased up to the composition $x = 0.35$ and with further increase of Al concentration disordering decreased. These observations indicate that with increasing Al concentration the low temperature magnetic phase of the disordered A2 phase of $Fe_{1-x}Al_x$ evolves from ferromagnetic to a spin glass state and the evolution is independent of the amounts of disorder present in the sample, rather a intrinsic property of the disordered phase as a function of Al concentration.

To confirm the nature of the magnetic states of $Fe_{1-x}Al_x$ inferred from resistivity

analysis, temperature variations of ZFC and FC magnetizations and magnetization–field isotherms (M–H) at 10 K were measured for the compositions $x = 0.25, 0.30, 0.45, 0.50,$ and 0.55. Temperature variations of ZFC and FC magnetizations are shown in Figs. 4.12(a)–(e) and M–H curves are shown in Figs. 4.13(a)–(e). In the compositions $x = 0.45, 0.50$ and 0.55, a bifurcation between ZFC and FC magnetizations was present at low temperature and the M–H curves were S-type without any sign of saturation in our measured field range up to 70 kOe which are typical characteristics of a spin glass system and are in accordance with the conclusion drawn from resistivity analysis. The composition $x = 0.25$ did not show any bifurcation between the ZFC and FC magnetizations and its temperature dependence of magnetic behavior is clearly in accordance to that of a ferromagnetic material. The M–H curve also resembles the ferromagnetic behavior with a saturating behavior and a very small coercivity. Surprisingly, a bifurcation was also present at low temperature between ZFC and FC magnetizations in the composition $x = 0.30$ indicating glassy behavior in contrast to the ferromagnetic character we found in resistivity analysis. However, the nature of the bifurcation between ZFC and FC magnetizations here in the composition $x = 0.30$ was quite different from the typical cusp like behaviors observed for a spin glass system as well as different from the bifurcations present in the higher Al compositions $x = 0.45, 0.50$ and 0.55. The M–H curve of the composition $x = 0.30$, similar to a ferromagnetic material, quickly reached towards saturation with increasing magnetic field, however, saturation was not achieved till the highest applied field of 50 kOe. In higher magnetic fields, a very slow but steady increase of magnetization was present. This indicates that there is a small amount of competing magnetic interaction is present in the system. This is likely to be due to the presence of a small amount of DO_3 phase, undetectable in XRD study. The DO_3 phase has a low temperature spin glass phase [169, 170] and is likely to occur in this composition range as it is the thermodynamically most favorable structure.

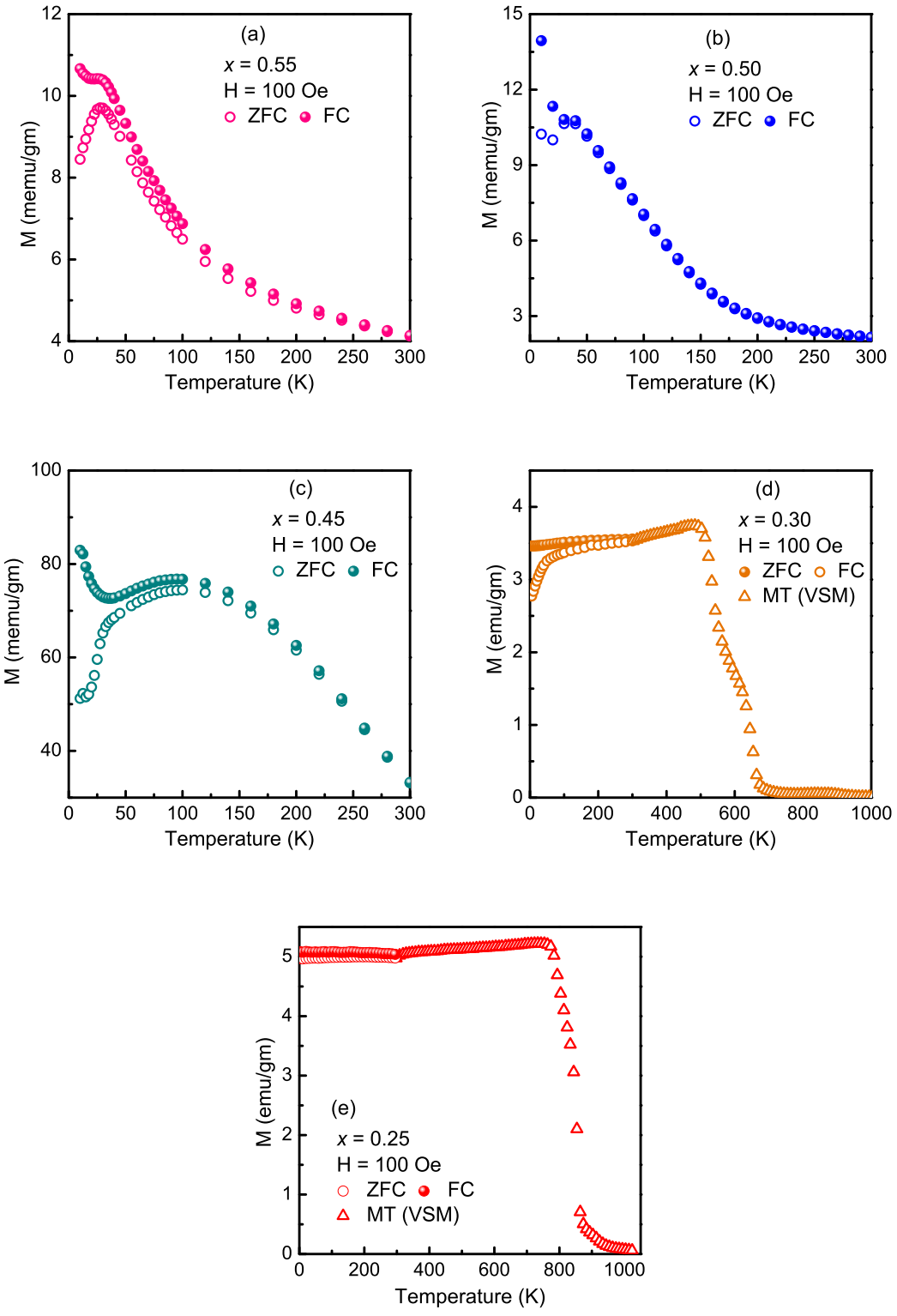

Figure 4.12: (a)–(e) Temperature variations of ZFC and FC magnetizations of $Fe_{1-x}Al_x$.

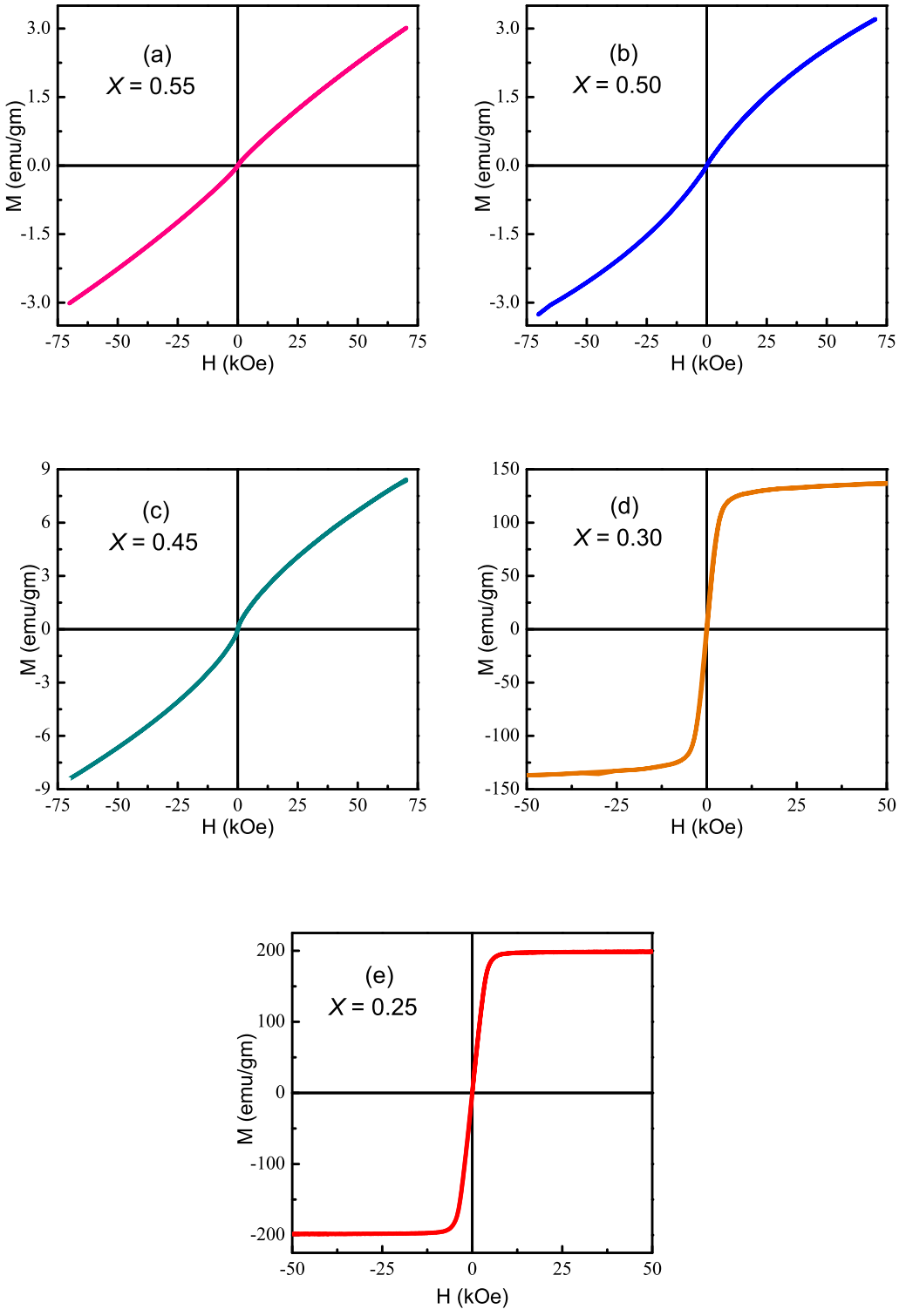

Figure 4.13: (a)–(e) Magnetization–field isotherms of $Fe_{1-x}Al_x$ at $T = 10$ K.

4.6 Theoretical analysis

4.6.1 Magnetic exchange interaction parameters

Magnetic exchange interaction parameters of the $x = 0.50$ composition, calculated using orbital peeling method, were presented in Sec. 3.5.2. This section describes

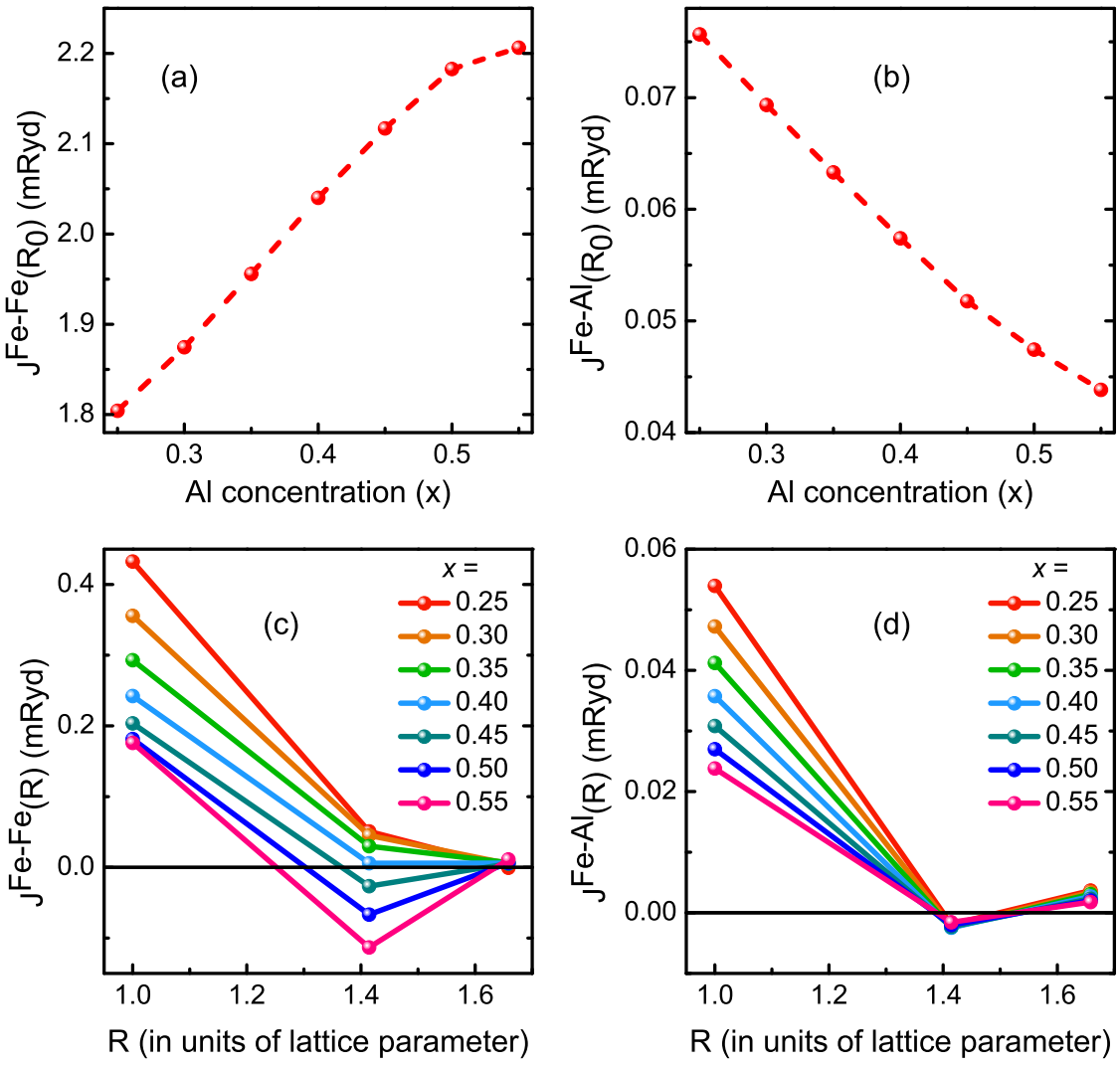

Figure 4.14: Variation with Al concentration of the nearest neighbor magnetic exchange interaction parameters between (a) Fe-Fe and (b) Al-Al pairs in $Fe_{1-x}Al_x$. Variation of magnetic exchange interaction parameters between (c) Fe-Fe and (d) Al-Al pairs with distance at different compositions of $Fe_{1-x}Al_x$.

the variation of the magnetic exchange interaction parameters of $Fe_{1-x}Al_x$ with composition. Figs. 4.14(a)–(d) show the variation of magnetic exchange interaction parameters between the constituent atomic pairs with distance and alloy composition. Magnetic exchange interactions between the Al-Al pairs are negligible owing to their non-magnetic character. Fig. 4.14(a) depicts that the nearest neighbor Fe-Fe interaction decreases with increasing Al concentration. However, as can be seen from the Fig. 4.14(b), the nearest neighbor Fe-Al interaction increases as the Al concentration increases. This observation is in contradiction to earlier reports [171–180] where only the Fe-Fe interaction or an effective magnetic interaction was considered and the interaction was found to be increasing, linearly or following some empirical formula, with an increase in Fe concentration. Although the decrease in nearest neighbor Fe-Fe interaction with increasing Fe concentration appears to be counter-intuitive, this phenomenon is common to many alloys where a magnetic constituent is mixed with a non-magnetic one. As the concentration of Al increases, the picture becomes closer to Fe clusters immersed in a sea of Al. Such a cluster magnetic impurity has higher exchange energy and larger moment as compared with greater Fe compositions.

The nearest neighbor Fe-Al interaction (shown in Fig. 4.14(d)) is much smaller than the nearest neighbor Fe-Fe interaction, and even smaller than the interaction between next nearest neighbor Fe-Fe atoms. However, the number of Fe-Al pair increases with increasing Al concentration, and accordingly, the significance of this Fe-Al interaction term to the effective magnetic interaction of the system increases with Al concentration. However, in earlier studies, magnetic interactions between Fe and Al atoms were never considered separately.

We found that the next nearest neighbor Fe-Fe interactions are ferromagnetic in our studied composition range (shown in Fig. 4.14(c)). Although earlier Plascak et al. [173] found that the next nearest neighbor Fe-Fe interaction is antiferromagnetic for the range of Al concentration between $x = 0.35$ to $x = 0.75$, their recent study [176]

based on effective field theory is in agreement with our observations that first and second nearest neighbor Fe-Fe interactions are ferromagnetic for the entire composition range studied here $0.25 \leq x \leq 0.55$. However, the third nearest neighbor Fe-Fe interaction drops below zero and becomes antiferromagnetic in the higher Al compositions $x \geq 0.45$ alloys. From resistivity analysis, we have seen that the low temperature magnetic state evolves from ferromagnetic type to spin glass phase with increasing Al concentration and this transition occurs around the Al concentration $x = 0.40$. Therefore, the antiferromagnetic third nearest neighbor Fe-Fe interaction in the higher Al compositions creates a competing magnetic environment in the system which causes magnetic frustrations and consequently spin glass phase appears at the higher Al compositions.

4.6.2 Magnetic phase diagram

Magnetic properties of the composition $x = 0.50$ were explored using Monte-Carlo (MC) simulation with the Ising Hamiltonian and the calculated exchange interactions from first-principles theories are presented in Sec. 3.5.3. This section describes the magnetic properties obtained from MC simulation, carried out in the same fashion, for the entire composition range $0.25 \leq x \leq 0.55$. The only difference is that here we used RS to generate the random occupation of the constituent atoms corresponding to the disordered A2 phase. This is because although SQS is superior to RS, as one moves away from simple fractions, finding structures with desirable correlation parameters becomes increasingly difficult as well as computationally expensive. Thus, SQS losses it's attractiveness for non-stoichiometric compositions. Variation of paramagnetic to ferromagnetic transition temperature T_C, obtained from the MC simulations, with Al concentration is shown in Fig. 4.15. Earlier reported experimental values and the values obtained from our magnetization measurements are also shown in the same figure for comparison. The T_C values obtained from MC simulation agree well with experimental data near the equiatomic composition. However, as we move away from the equiatomic

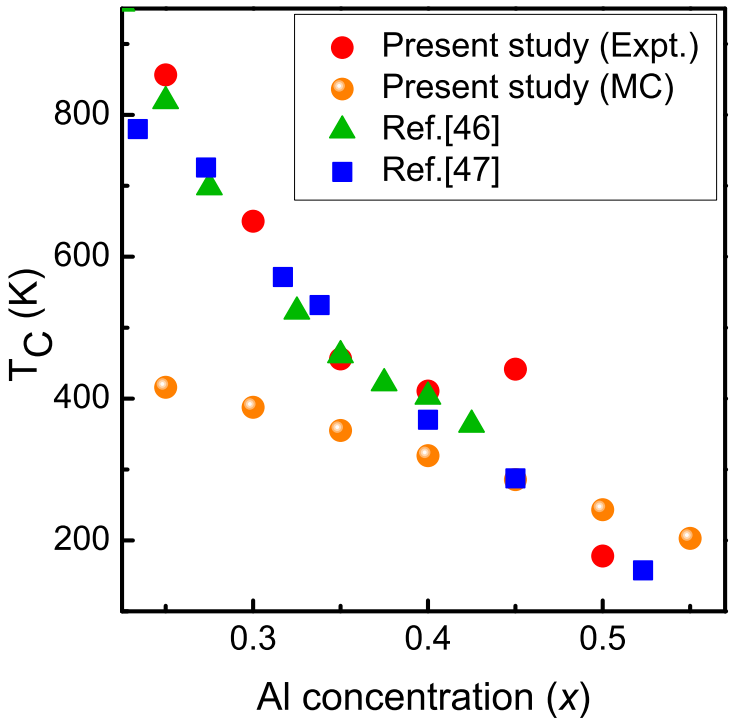

Figure 4.15: Variation of the paramagnetic to ferromagnetic transition temperature T_C of $Fe_{1-x}Al_x$ with Al concentration.

composition towards the Fe-rich region, the obtained T_C values from MC simulations deviate from experimental data. This is primarily because as one deviates from the equiatomic composition for this A2 phase, more number of Fe atoms goes to the anti-site position where they are surrounded by a larger number of Fe atoms than average and consequently have a larger moment and higher magnetic exchange energy. This situation is difficult to simulate and our method is not very efficient in describing this situation leading to the observed deviations of the MC simulated T_C from experimental data.

4.6.3 Effect of short-range ordering

To complete the investigation, we have also studied the effects of the presence of short-range ordering on the magnetic transition temperature using MC simulation.

MC simulations were carried in identical ways to the previous section. Although SQS is a better choice for this type of situations involving inhomogeneous disorder, they are difficult and computationally very expensive to generate for non-stoichiometric compositions and for these type of inhomogeneous disorder in non-stoichiometric compositions it is nearly impossible to get a good SQS. Here the short-range ordering is simulated in a different way. The crystal structure of the A2 and B2 phase can be decomposed into two interpenetrating simple cubic structures. In the A2 phase, Fe and Al atoms randomly occupy the lattice sites in both the simple cubic sublattices and the probability of occupancy at any lattice sites in both the simple cubic sublattices of Fe or Al atoms is equal to their atomic percentage in the alloy composition. However, when this system orders (i.e., is in the B2 phase) Fe atoms preferentially occupy one of the two simple cubic sublattices while the Al atoms occupy the other one. To incorporate the ordered B2 phase into the disordered lattice of A2 phase, first we fixed the ordering fraction of ordered to disordered phase in the lattice. We considered a pair of lattice sites, one from each of the two simple cubic sublattices and generated a random number between 0 and 1 for this pair of lattice sites. If the random number was greater than the value of the ordering fraction, the pair of sites were filled up according to the disordered configuration, otherwise the pair of sites were populated according to ordered configuration.

Fig. 4.16 depicts the variation of T_C with ordering fraction at different alloy compositions. Similar to the effect of short-range ordering on T_C found earlier for the composition $x = 0.50$ (in Sec. 3.5.3), T_C decreased with increasing ordering fraction in all the studied compositions. For low values of ordering fraction, up to 0.2, the decrease of T_C was almost linear after which it fell faster. This behavior was particularly noticeable in the Fe-rich compositions.

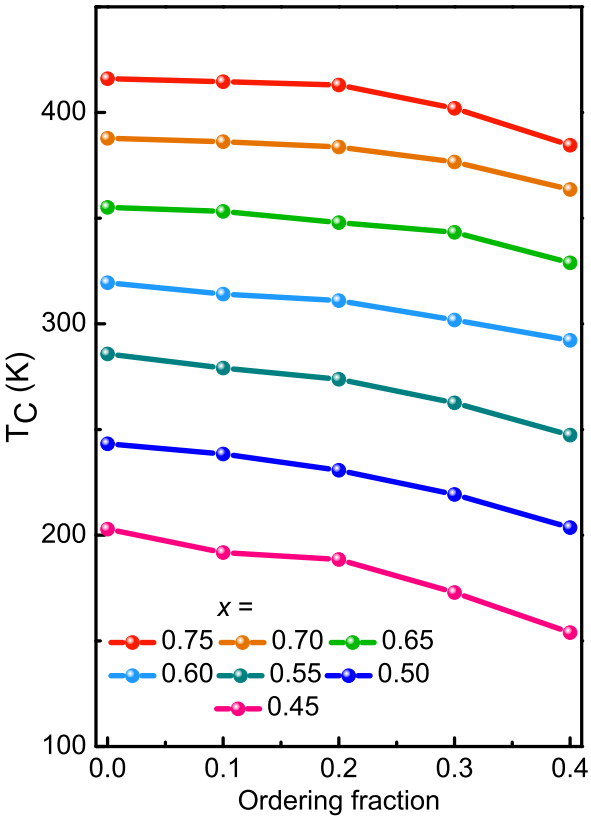

Figure 4.16: Variation of T_C with ordering fraction at different compositions of $Fe_{1-x}Al_x$.

4.7 Conclusions

Structural, magnetic and transport properties of $Fe_{1-x}Al_x$ ($0.25 \leq x \leq 0.55$) have been described in this chapter. The experimental results are further supplemented with the first-principles calculations and MC simulations. These studies showed that the disorder in these alloys increased with Al concentration up to $x = 0.35$ and with further increase of Al concentration the presence of short-range ordered clusters increased which was most clearly visible from the occurrence of superlattice reflections in the XRD patterns of the higher Al concentration alloys $x = 0.50$ and 0.55. The analysis of low temperature resistivity data and magnetization measurements showed that while the A2 phase on the Fe-rich compositions has ferromagnetic low temperature state, higher Al concentrations have a spin glass phase. The presence of short-range ordered clus-

ters causes a mixed magnetic phase of ferromagnetic and spin glass character for the compositions $x = 0.50$ and 0.55. The calculations of magnetic exchange interaction parameters from first-principles theories further confirmed the conclusions about magnetic phases drawn from experimental investigations. The Fe-Fe magnetic exchange interaction parameters, which is the dominant one in these alloys, have ferromagnetic character up to fourth nearest neighbor for Al compositions up to $x = 0.40$. However, the third nearest neighbor Fe-Fe magnetic exchange interaction drops below zero on higher Al compositions beyond $x = 0.45$ which consequently causes a competing magnetic environment in the system and drives the system towards a spin glass state. In these alloys disordering induces magnetism and this is further seen in MC simulations which showed that paramagnetic to ferromagnetic transition temperature T_C decreases with increasing ordering in the system.

5 Structural, Magnetic and Transport Properties of $FeAl_{2-x}Ga_x$ Alloys

5.1 Introduction

In the previous two chapters, we have described disordered cubic Fe-Al alloys which form on the low and intermediate ranges of Al concentration [42–45]. We have shown that structural, magnetic and transport properties of the alloys in those concentration regions are strongly influenced by the competition between different structural phases along with the presence of disorder in the system. In the Al-rich part of the phase diagram, the intermetallic compound $FeAl_2$ forms [44, 45, 53, 54] which is a substitutional type disordered alloy. Previous investigations reported various intriguing structural, magnetic and transport properties of this intermetallic compound and we intend to study this system closely.

$FeAl_2$ crystallizes into a triclinic structure [54] comprising 19 atoms in the unit cell as shown in Fig. 5.1. The space group number and Pearson symbol of the structure are 2 and aP19, respectively. DFT based electronic structure calculations [53, 59, 60] indicate that a $MoSi_2$-type tetragonal structure is energetically more favorable than the triclinic aP19 phase. However, this hypothetical tetragonal structure has not been found so far in any experimental investigations. The atomic density in the unit cell of the aP19 structure is very low which is the primary reason behind its stability over the theoretically anticipated tetragonal structure [53]. All the lattice sites are fully occupied by either Fe or Al atoms except two sites corresponding to a Wyckoff position

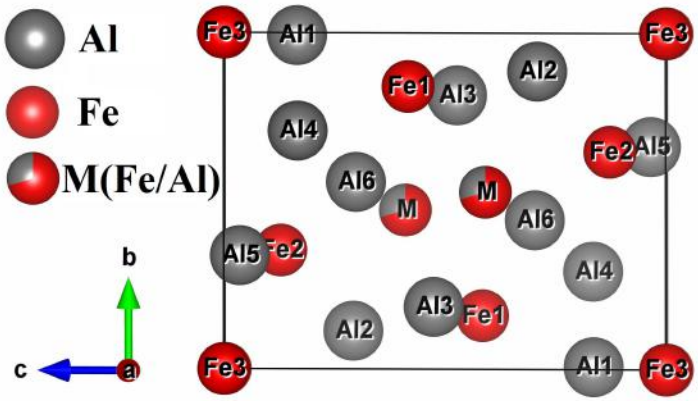

Figure 5.1: Arrangement of Fe and Al atoms in the aP19 unit cell of $FeAl_2$.

of multiplicity two (shown in the mixed color of gray and red in Fig. 5.1) which could be occupied by either of the two atoms [54]. According to Chumak et al. [54], occupancy probabilities of Fe and Al atoms at these mixed occupancy sites are 0.705 and 0.295, respectively. This statistical occupancy of Fe and Al atoms creates substitutional disorder in the aP19 phase of $FeAl_2$.

Magnetic properties of $FeAl_2$ have been explored through various measurements like dc magnetization, ac susceptibility, NMR, neutron diffraction, Mössbauer etc. by different researchers [55–58]. These measurements revealed that Fe atoms interact among themselves antiferromagnetically. The presence of substitutional disorder, combined with the antiferromagnetic interactions among the Fe atoms, results in a low-temperature spin glass state ($T_{sg} \sim 12$ K). Above the spin glass transition temperature another magnetic transition appears whose nature, whether the transition is spin glass or antiferromagnetic type, as well as the value of the transition temperature is highly controversial. From Mössbauer and NMR measurements Chi et al. [56] concluded that the Fe moments are partially localized which is also surprising for a Fe-based 3*d* intermetallic alloy system.

In the resistivity study of $FeAl_2$, Lue et al. [55] found that the temperature variation of resistivity depicts a minimum and $\rho(T) \sim \sqrt{T}$ at temperatures below the

resistivity minimum. Such a temperature dependence of resistivity is generally observed in disordered bulk alloys where enhanced electron-electron interaction (EEI) gives rise to the resistivity minimum in competition with the inelastic scattering processes as discussed in Sec. 1.3.2. However, this aspect was not explored in earlier studies. In this chapter, we have systematically investigated the structural, magnetic and transport properties of $FeAl_2$ and the effects of the replacement of Al atoms by iso-electronic Ga atoms.

5.2 Sample preparation and compositional characterization

Polycrystalline ingots of $FeAl_{2-x}Ga_x$ ($0 \leq x \leq 0.5$) were prepared by arc melting appropriate amounts of high ($\geq$ 99.9%) purity constituent elements and annealed at 1173 K for six days. The compositions obtained from EDX analysis are listed in Table 5.1 which shows the good compositional homogeneity of the prepared ingots with the average composition close to the target value.

Table 5.1: Compositions of the prepared polycrystalline ingots of $FeAl_{2-x}Ga_x$ as obtained from EDX measurements.

x	Obtained concentrations (at%)		
	Fe	Al	Ga
0.000	30.3(3)	69.7(3)	–
0.125	32.9(8)	62.4(6)	4.7(4)
0.250	32.0(5)	59.8(7)	8.2(4)
0.375	31.8(8)	56.2(4)	12.0(6)
0.500	31.2(8)	51.7(8)	17.1(7)

5.3 Crystal structure

XRD patterns of $FeAl_{2-x}Ga_x$ ($0 \leq x \leq 0.5$) were collected with Cu-Kα X-ray source and are shown in Figs. 5.2(a)–(e). All peaks present in the XRD patterns correspond to the triclinic aP19 phase. The Rietveld refinements of the XRD patterns considering the aP19 phase of the unit cell are shown in Figs. 5.2 (a)–(e) which show a good agreement in all compositions. The crystal structure parameters and atomic occupancies obtained from the refinements are respectively listed in Table 5.2 and Table 5.3. As can be seen from Figs. 5.2(a)–(e), the aP19 phase persisted up to the highest Ga composition studied here and the theoretically anticipated tetragonal structure was not found in any of the compositions. This indicates that the triclinic aP19 phase is highly stable against the formation of the theoretically predicted tetragonal phase. The crystal structure parameters of $FeAl_2$ agree well that reported earlier by Chumak et al. [54]. The relative change in unit cell volume as a function of Ga concentration is shown in Fig. 5.2(f) in the form $\frac{\Delta V}{V_0} \times 100$ where V_0 is the unit cell volume at the Ga concentration $x = 0$ and ΔV is the change in unit cell volume relative to $x = 0$. As can be seen from this figure, the unit cell volume increases with increasing Ga concentration. As the unit cell volume increases, hybridization between Fe and Al electronic states decreases and consequently influences the magnetic properties that will be shown in the following sections.

The atomic occupancies of Fe and Al atoms at the Wyckoff site Fe4A/Al4B, where the mixed occupancies of Fe and Al atoms occur, in $FeAl_2$ obtained from the Rietveld refinement were 0.583 ± 7 and 0.417 ± 7, respectively. The obtained atomic occupancies agree well with that reported earlier by Chumak et al. [54]. The Rietveld refinements of the XRD patterns of the $x \neq 0$ compositions reveal that Ga atoms prefer the Al sites and as can be seen from the Table 5.3, atomic occupancies of Ga atoms at the Al sites increase with increasing Ga concentration. The Fe4A/Al4B Wyckoff site also

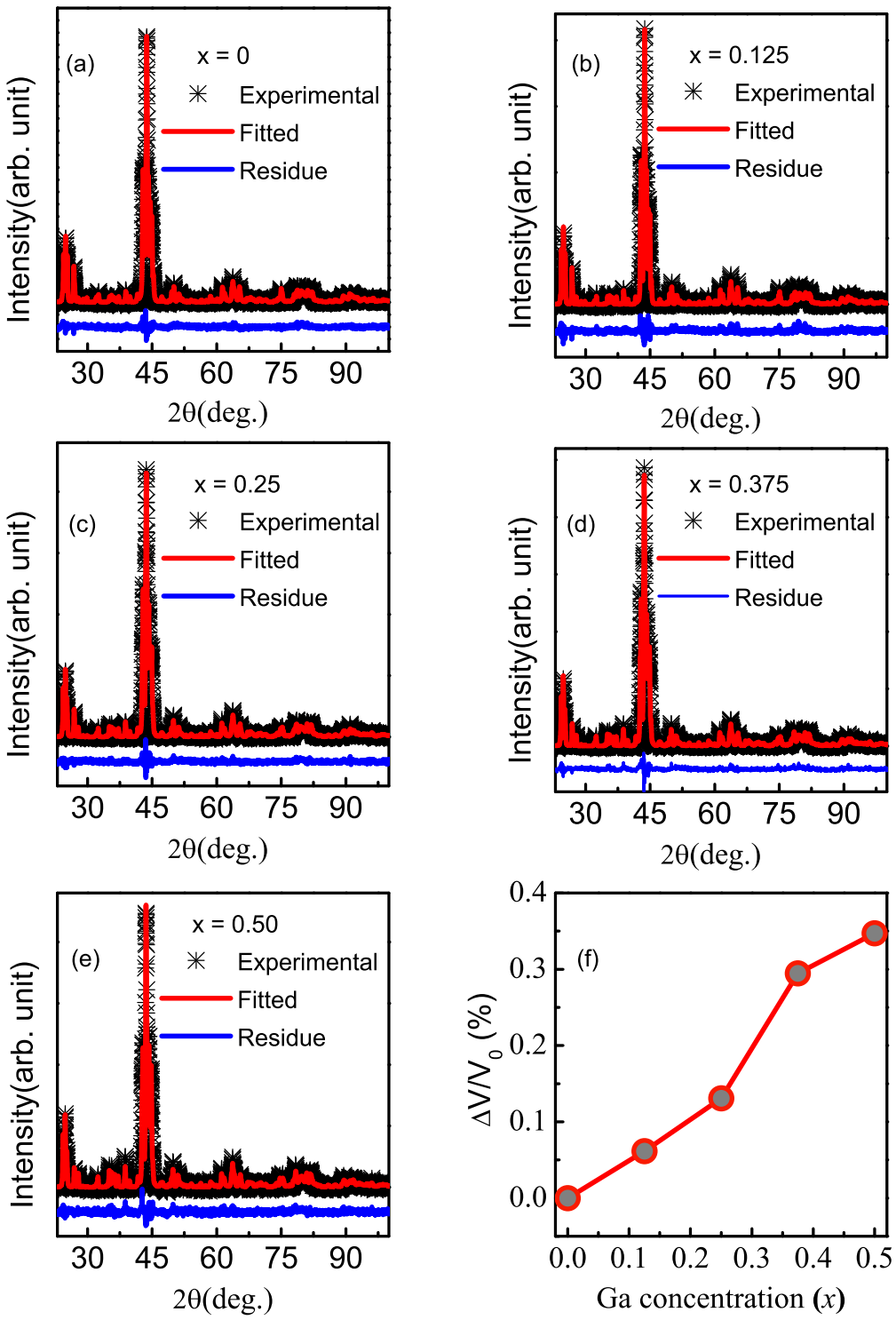

Figure 5.2: (a)–(e) Experimental XRD patterns of $FeAl_{2-x}Ga_x$ measured using Cu Kα X-ray source and the Rietveld refinement fits. (f) Relative change in unit cell volume of $FeAl_{2-x}Ga_x$ ($0 \leq x \leq 0.5$) as a function of Ga concentration.

Table 5.2: Lattice parameters of $FeAl_{2-x}Ga_x$ obtained from the Rietveld refinements of XRD patterns.

Ga concentration (x)	a (Å)	b (Å)	c (Å)	α (deg.)	β (deg.)	γ (deg.)	χ^2
0.000	4.86403 (9)	6.4493 (1)	8.7354 (2)	87.983 (2)	74.445 (1)	83.109 (1)	1.92
0.125	4.86656 (9)	6.4482 (1)	8.7386 (2)	87.979 (2)	74.387 (1)	83.196 (1)	3.26
0.250	4.86577 (8)	6.4422 (1)	8.7545 (1)	87.855 (1)	74.346 (1)	83.283 (1)	2.04
0.375	4.87104 (9)	6.4440 (1)	8.7584 (1)	87.874 (1)	74.286 (1)	83.342 (1)	2.70
0.500	4.8727 (1)	6.4400 (1)	8.7665 (1)	87.856 (2)	74.226 (2)	83.431 (2)	4.12

have a finite probability of occupation for Ga atom along with the Fe and Al atoms in the $x \neq 0$ compositions. With our present X-ray diffraction data measured in a laboratory diffractometer, determination of occupancies of three different atomic species at a single Wyckoff site is not possible with reasonable accuracy. However, Al concentration in the structure is always much higher than that of Ga for the composition range explored here and therefore, in principle, the probability of occupancy of Al atoms should be higher than that of Ga atoms. In addition, Rietveld refinement of Al atoms together with Fe instead of Ga often actually lead to poor fit quality compared to when Ga atoms were put together with Fe ones. Therefore, the occupancies of Fe and Al atoms at the Fe4A/Al4B site were kept fixed to their ideal values for $FeAl_2$ during Rietveld refinements of the $x > 0$ compositions. As can be seen from Table 5.3, occupancies of Ga atoms at the Al sites increases with increasing Ga concentration as expected. In addition to the substitutional disorder present in the host $FeAl_2$ due to the mixed occupancy of Fe and Al atoms, the mixed occupancy of Al and Ga atoms at the Al sites creates further substitutional disorder which increases with increasing Ga concentration.

Table 5.3: Atomic occupancies in the lattice sites of $FeAl_{2-x}Ga_x$ obtained from Rietveld refinements of XRD patterns. *x1*, *x2*, *x3*, *x4* and *x5* correspond to the Ga concentration (x) 0, 0.125, 0.25, 0.375 and 0.50, respectively. * For more information about the site labels please see Ref. [54].

Site label*	Atomic occupancies														
	Fe					Al					Ga				
	x_1	x_2	x_3	x_4	x_5	x_1	x_2	x_3	x_4	x_5	x_1	x_2	x_3	x_4	x_5
Fe1	1	1	1	1	1	0	0	0	0	0	0	0	0	0	0
Fe2	1	1	1	1	1	0	0	0	0	0	0	0	0	0	0
Fe3	1	1	1	1	1	0	0	0	0	0	0	0	0	0	0
Fe4A/ Al4B	0.583 (7)	0.67	0.67	0.67	0.67	0.417 (7)	0.33	0.33	0.33	0.33	0	0	0	0	0
Al1	0	0	0	0	0	1	0.983 (7)	0.810 (5)	0.773 (6)	0.660 (8)	0	0.017 (7)	0.190 (5)	0.227 (6)	0.340 (8)
Al2	0	0	0	0	0	1	0.980 (6)	0.882 (4)	0.827 (5)	0.770 (7)	0	0.020 (6)	0.118 (4)	0.173 (5)	0.230 (7)
Al3	0	0	0	0	0	1	1	1	0.958 (9)	0.93 (1)	0	0	0	0.042 (9)	0.07 (1)
Al4	0	0	0	0	0	1	1	0.965 (6)	0.953 (8)	0.93 (1)	0	0	0.035 (6)	0.047 (8)	0.07 (1)
Al5	0	0	0	0	0	1	0.949 (7)	0.916 (5)	0.948 (8)	0.90 (1)	0	0.051 (7)	0.084 (5)	0.052 (8)	0.10 (1)
Al6	0	0	0	0	0	1	0.849 (6)	0.767 (4)	0.701 (5)	0.587 (6)	0	0.151 (6)	0.233 (4)	0.299 (5)	0.413 (6)

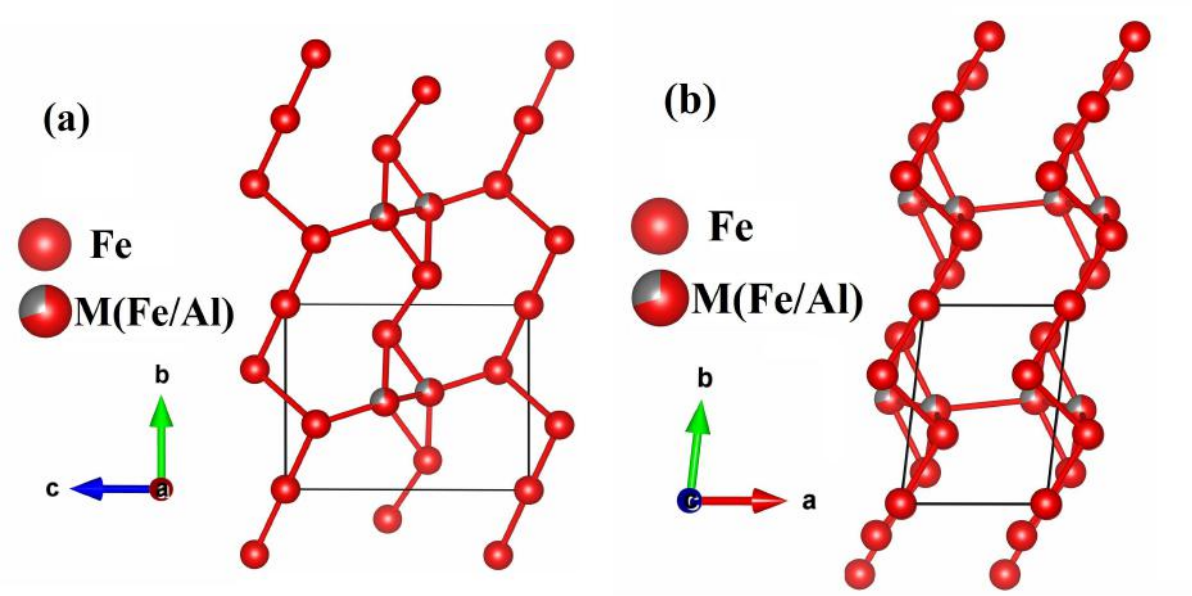

Figure 5.3: Views of the arrangement of Fe atoms in the aP19 crystal structure of $FeAl_2$: (a) in the *bc*-plane and (b) in the *ab*-plane.

Another aspect of the aP19 structure is shown in Figs. 5.3(a)–(b) in which bondings between Fe-Fe pairs are shown up to a distance of 3.5 Å. As can be seen from the figure, Fe-Fe pairs are mostly connected in the crystallographic *bc*-plane which in turn suggests that the interactions among the Fe atoms mostly lie on the crystallographic *bc*-plane. The interplaner Fe-Fe magnetic interaction along the crystallographic *a*-axis occurs only through a single Fe-Fe pair. Along with such low-dimensional character, the magnetic structure is frustrated as can be seen from the base sharing triangle at the center of the *bc*-plane.

5.4 Magnetic properties

5.4.1 DC magnetization

Temperature variations of ZFC and FC magnetizations of $FeAl_{2-x}Ga_x$ ($0 \leq x \leq 0.5$) alloys, measured at an applied magnetic field of $H = 1$ kOe, are shown in Fig.

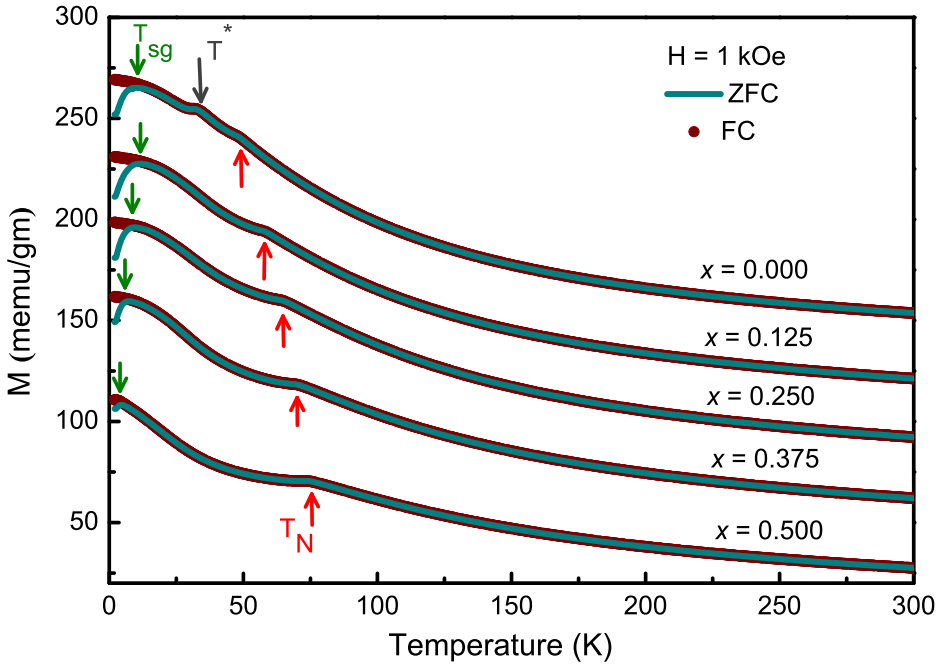

Figure 5.4: Temperature variations of ZFC and FC magnetizations of $FeAl_{2-x}Ga_x$ measured at $H = 1$ kOe. Graphs are successively shifted upward from the $x = 0.5$ composition data by 30 on the Y-scale for clarity.

5.4. Characteristic behaviors of the ZFC and FC magnetizations were identical in all compositions except for $x = 0$. Previous studies reported a low-temperature spin glass state of $FeAl_2$ at $T_{sg} \sim 12$ K [55–58]. Consistent with that, we also found a rounded peak at $T \sim 12$ K in the ZFC magnetization of $FeAl_2$ below which a bifurcation appeared between the ZFC and FC magnetizations. As discussed in Sec. 1.3.3, the presence of this type of peak in ZFC magnetization along with a bifurcation between ZFC and FC magnetization at temperatures below the peak are typical signatures of a spin glass transition. Similar rounded peak in the ZFC magnetizations at low temperatures and bifurcation between ZFC and FC magnetizations were present in all compositions which substantiate that the spin glass state of $FeAl_2$ persisted up to the highest Ga compositions studied here. As can be seen from Fig. 5.4, the spin glass transition shifted to lower temperatures with increasing Ga concentration.

Above T_{sg}, another transition (shown with vertical red arrows in Fig. 5.4) appeared at temperature T_N ($T_N > T_{sg}$) in all compositions. This transition at T_N appeared

as a small hump in the composition $x = 0$ and gradually evolved into a prominent peak as the Ga concentration was increased. T_N shifted to higher temperatures with increasing Ga concentration. ZFC and FC magnetizations did not show any irreversibility on passing through T_N which substantiates that this transition was not a gradual spin freezing one like the one present at temperature T_{sg}. Magnetization value also decreased as the Ga concentration was increased. This decrease in magnetization value, combined with the increase of T_N and the decrease of T_{sg} with increasing Ga concentration, indicates the gradual relieving of magnetic frustration of the system.

While only T_{sg} and T_N were present in the $x \neq 0$ compositions, the $x = 0$ composition had another magnetic transition at T^* (shown with a black downward arrow in Fig. 5.4) in between T_{sg} and T_N ($T_{sg} < T^* < T_N$). A bifurcation between ZFC and FC magnetizations (shown in Fig. 5.5) was also present at temperatures near T^*. Generally, bifurcation between ZFC and FC magnetizations progressively increases on lower-

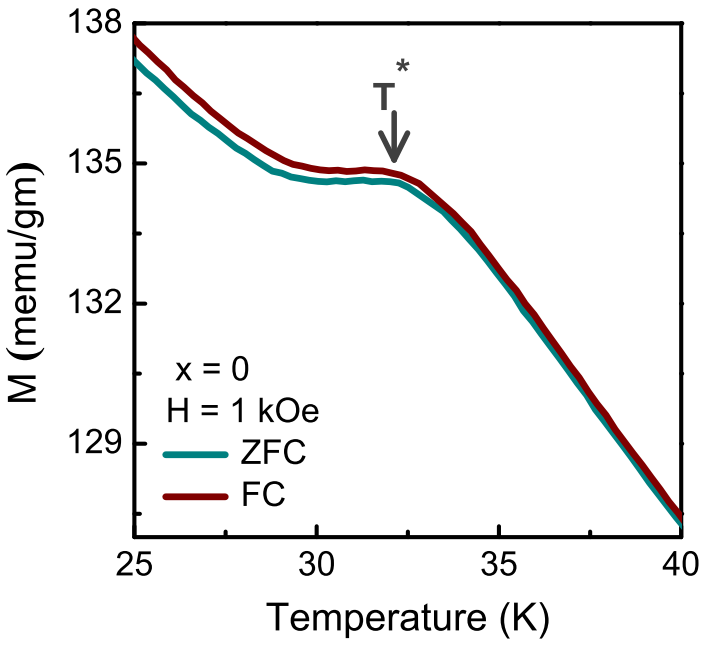

Figure 5.5: Temperature variations of ZFC and FC magnetizations of $FeAl_2$ ($x = 0$) around the magnetic transition at T^*.

ing temperature below T_{sg} for a spin glass transition. However, the bifurcation between ZFC and FC magnetizations below T^* remained almost constant down to T_{sg}. Similar observation was also made by Jagličić et al. [58] which indicates that the magnetic transition at T^* is different from a spin glass transition. Earlier studies of Mössbauer and neutron diffraction indicated antiferromagnetic nature of this transition although the value of T_N did not agree among them [56, 57]. Our magnetization measurements indicate that two successive magnetic transitions were present at T^* and T_N in $FeAl_2$, whereas those previous studies reported only one magnetic transition. From the above discussions we can infer that the previous studies detected either of these transitions (i.e., at T* or T_N) which resulted in the disagreement between reported values of T_N. We therefore further explored the characteristic behaviour of the magnetic transition at T^* in $FeAl_2$ ($x = 0$) through ac susceptibility, M-H curves and field dependence of T^* in dc magnetization.

The paramagnetic region of the ZFC magnetization curves of $FeAl_{2-x}Ga_x$ measured at $H = 1$ kOe were fitted with Curie-Weiss law:

$$\chi(T) = \chi_0 + \frac{C}{T - \theta} \tag{5.1}$$

where χ_0 is the temperature independent part of the susceptibility, C is the Curie-Weiss constant and θ is the Curie-Weiss temperature which indicates the nature of magnetic

Table 5.4: Values of χ_0, μ_{Fe} and θ obtained from the fitting of $M_{ZFC}(T)$ of $FeAl_{2-x}Ga_x$ measured at $H = 1$ kOe with Curie-Weiss law.

Ga concentration (x)	χ_0 (emu gm^{-1} Oe^{-1})	μ_{Fe} (μ_B)	θ (K)
0.000	$6.67(1) \times 10^{-6}$	2.756(1)	-20.07(7)
0.125	$2.50(2) \times 10^{-6}$	2.956(1)	-30.15(8)
0.250	$2.08(3) \times 10^{-6}$	3.103(2)	-31.3(1)
0.375	$1.77(2) \times 10^{-6}$	3.241(1)	-44.97(8)
0.500	$5.6(2) \times 10^{-7}$	3.180(1)	-57.5(1)

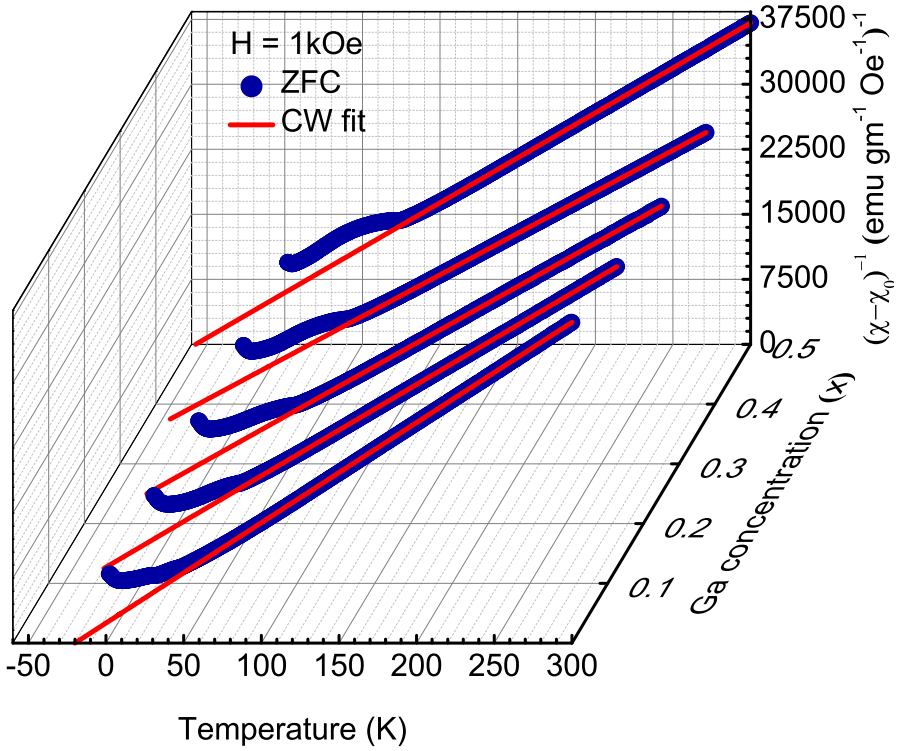

Figure 5.6: Curie-Weiss (CW) fit of ZFC magnetizations of $FeAl_{2-x}Ga_x$ measured at $H = 1$ kOe.

interactions in the system. While a *positive* value of θ indicates ferromagnetic interaction, *negative* value indicates antiferromagnetic interaction. The Curie-Weiss fits of the ZFC magnetizations ($H = 1$ kOe) are shown in Fig. 5.6 and the fit parameters are listed in Table 5.4. We found that the value of θ is *negative* in all compositions suggesting antiferromagnetic nature of the spin interaction which is consistent with the earlier reports of $FeAl_2$ [55–58]. As can be seen from Table 5.4, $|\theta|$ steadily increases with Ga concentration which indicates the enhancement of antiferromagnetic interaction as more and more Ga replaces Al. The value Fe magnetic moment, μ_{Fe}, in the composition $x = 0$ agrees well with the previous reports [55–58]. The increase of μ_{Fe} with increasing Ga concentration is due to the increase of unit cell volume which decreases the overlap between Fe and Al electronic states and thereby enhances the effective Fe magnetic

moment.

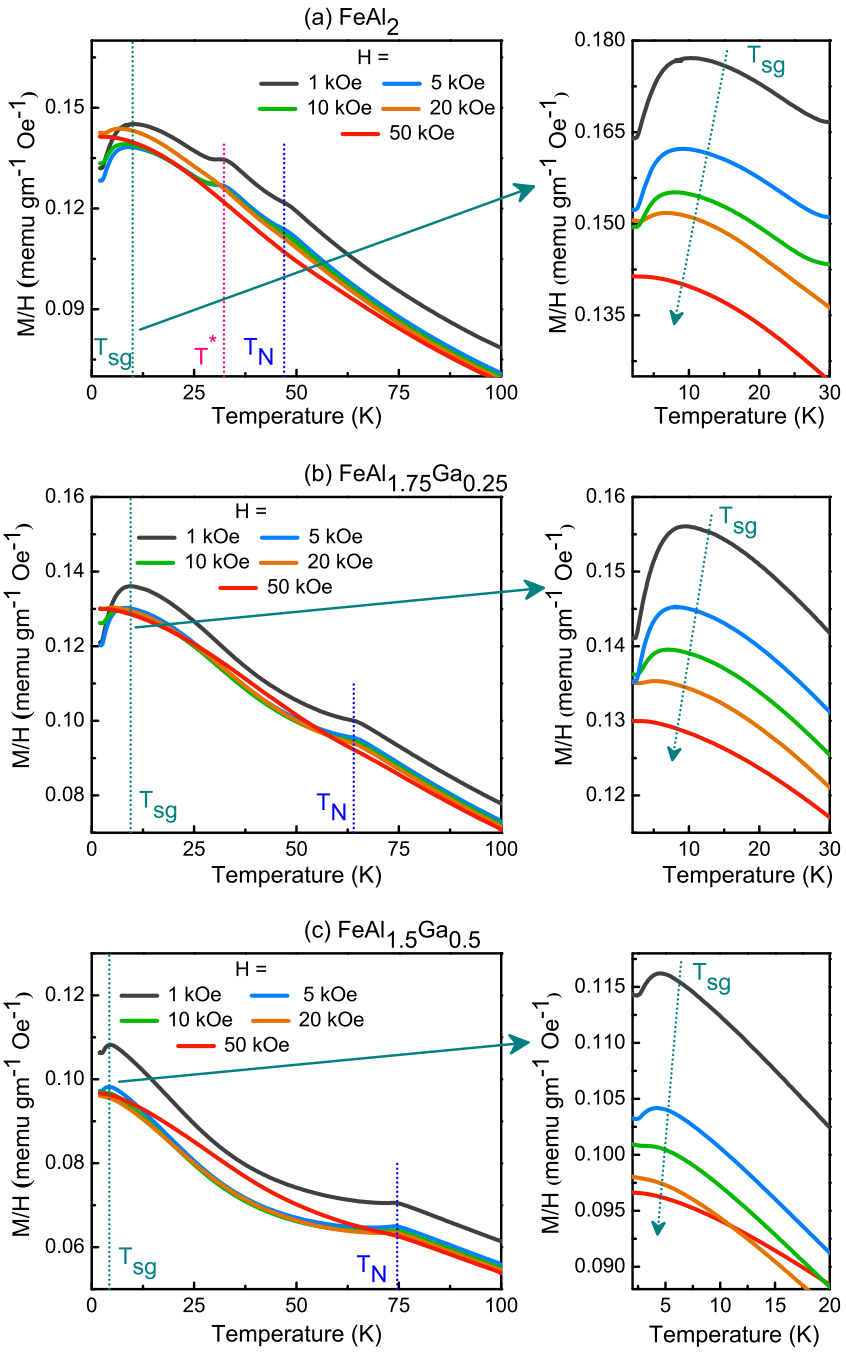

Figure 5.7: (a)–(c) Temperature dependences of the ZFC dc magnetic susceptibilities of $FeAl_{2-x}Ga_x$ measured at different applied fields. In the enlarged views of the figures (a), (b) and (c) around T_{sg}, the graphs are shifted upward on the Y-scale successively from the $H = 1$ kOe data by 0.008, 0.005, and 0.002, respectively, for clarity.

Temperature variations of ZFC dc magnetic susceptibilities of $FeAl_{2-x}Ga_x$ for different applied field strengths are shown in Figs. 5.7(a)–(c). The enlarged views

around T_{sg} are shown in the inset graph of Figs. 5.7(a)–(c) which show that the spin freezing temperature T_{sg} shifts to lower temperatures along with a gradual destruction of the peak as the external field increases. This smearing of the spin glass peak and gradual destruction with increasing magnetic field are also typical of a spin glass system.

Field dependence of spin freezing temperature T_{sg} can be expressed as [28, 181–183]:

$$H \propto \left(1 - \frac{T_{sg}(H)}{T_{sg}(0)}\right)^{n} \tag{5.2}$$

The value of the exponent n differentiates two different scenarios. For Ising type spin glass, $n = \frac{3}{2}$ and the critical line is called Almeida-Thouless (AT) line [182]. This separates an infinite range Ising spin glass in temperature and field from a paramagnetic phase. For isotropic Heisenberg spin glass, $n = \frac{1}{2}$ separates the freezing of transverse degrees of freedom in temperature and field, and the critical line is called Gabay-Thouless (GT) line [183]. The variation of T_{sg} of $FeAl_{2-x}Ga_x$ with field and the fitting with Eq. 5.2 is shown in Figs. 5.8(a)–(b). We found that variation of T_{sg} with H best fits with $n = \frac{3}{2}$ indicating the collinear nature of SG.

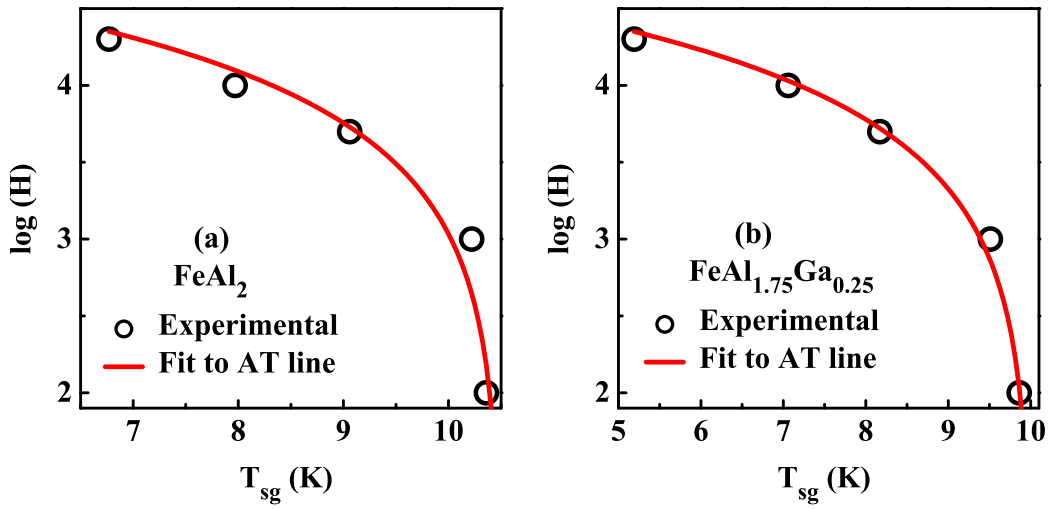

Figure 5.8: (a)–(b) Magnetic field dependences of the spin glass transition temperature T_{sg} of $FeAl_{2-x}Ga_x$.

The enlarged view of the temperature dependences of the ZFC dc magnetic

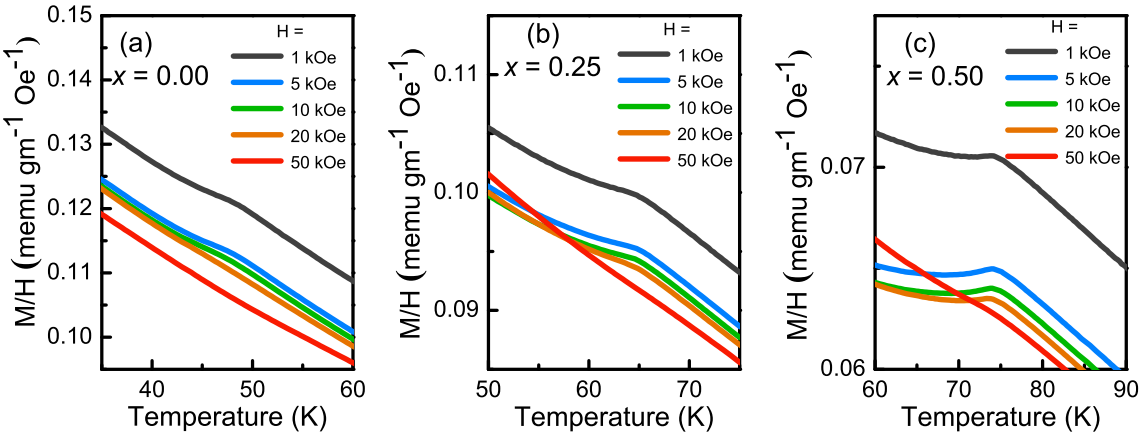

Figure 5.9: (a)–(c) The enlarged view of the temperature dependence of the ZFC dc magnetic susceptibilities of $FeAl_{2-x}Ga_x$ at different magnetic fields around the antiferromagnetic transition.

susceptibilities at different applied field strengths around the antiferromagnetic transition are shown in Figs. 5.9(a)–(c). As the applied field increased, the antiferromagnetic transitions got gradually suppressed and at $H = 5$ T, they nearly disappeared in all compositions. This destruction of the antiferromagnetic phase at this comparatively low field manifests the weak nature of the antiferromagnetic ordering in $FeAl_{2-x}Ga_x$.

Fig. 5.10 shows the variation of ZFC dc magnetic susceptibility of $FeAl_2$ with temperature at different applied field strength around the temperature T^*. With increasing applied field strength, the peak was gradually suppressed and at $H = 5$T, got nearly destroyed. This variation of T^* with applied field strength is similar to the one observed at T_N and demonstrates the similarity of T^* with T_N, rather than with T_{sg}.

Magnetization–field (M–H) isotherms of $FeAl_{2-x}Ga_x$ measured at $T = 2$ K in the field range -50 kOe to +50 kOe are shown in Fig. 5.11(a). Fig. 5.11(b) shows the enlarged view of the M–H curves around the origin. M–H curves did not saturate even in the highest applied field of 50 kOe. $FeAl_{2-x}Ga_x$ alloys have spin glass phase at temperatures where these M–H curves were measured. In the spin glass phase, local anisotropy prevents the frozen-in moments from aligning along the applied field direction and thereby makes the saturation of M–H curve very difficult to attain. Therefore,

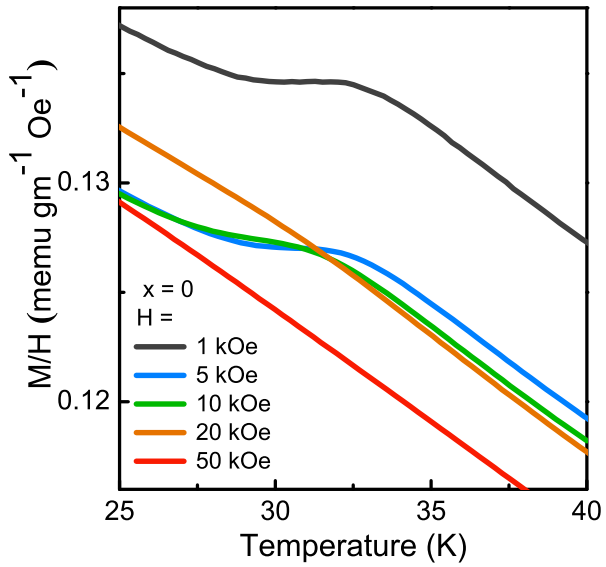

Figure 5.10: Temperature variation of ZFC dc magnetic susceptibility of $FeAl_2$ ($x = 0$) at different applied field around T^*.

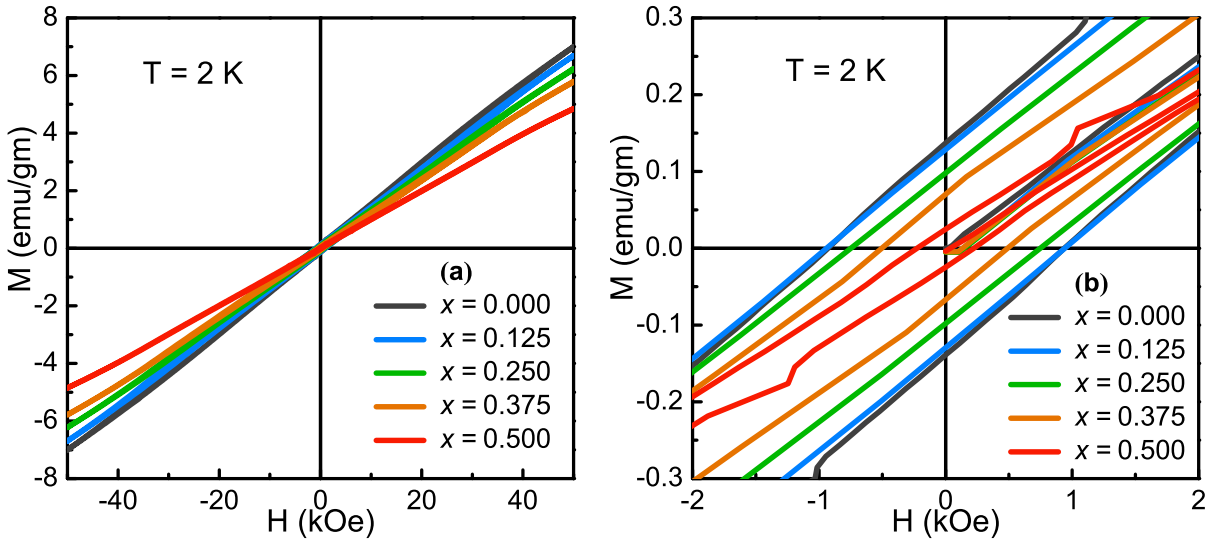

Figure 5.11: (a) M–H curves of $FeAl_{2-x}Ga_x$ measured at $T = 2$ K and (b) enlarged view of the M–H curves near the origin.

the non-saturating behavior of the observed M–H curves of $FeAl_{2-x}Ga_x$ at T = 2 K are consistent with the properties of a spin glass phase. A small hysteresis is also present in all the compositions which is also typical of a spin glass system and arises from the time dependence of the isothermal remanent magnetization. Magnetization value, as

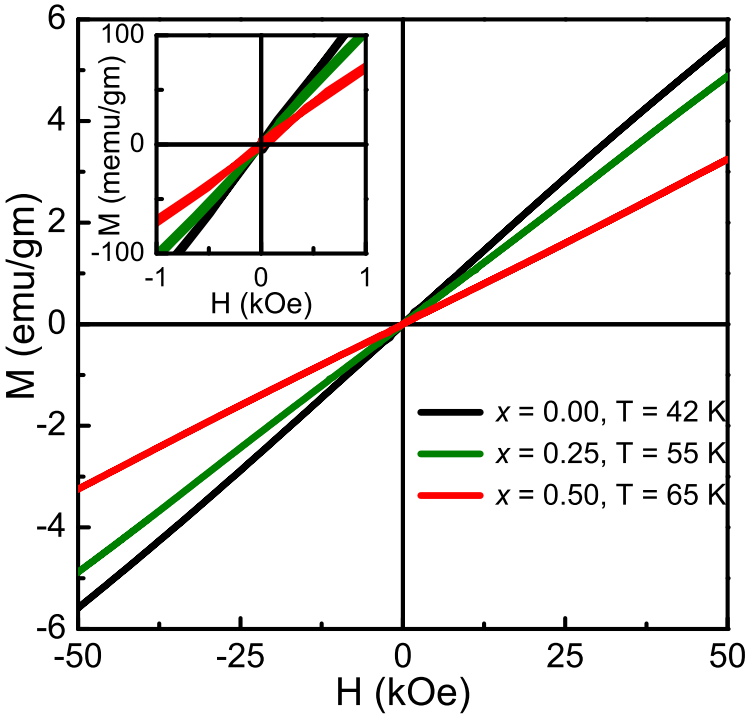

Figure 5.12: M–H curves of $FeAl_{2-x}Ga_x$ measured at temperatures below T_N. Inset show the enlarged view of the M–H curves near the origin.

well as the coercive field, decreases with increasing Ga concentration which manifests the growing antiferromagnetic character of the alloys as Ga concentration increases.

Fig. 5.12 shows the M–H curves of $FeAl_{2-x}Ga_x$ below the antiferromagnetic transition. These curves also did not saturate even to the highest applied field of 50 kOe and were linear up to the highest applied field. In addition, as can be seen from the inset figure, hysteresis behavior was absent in all compositions. Such linear-like M–H curves are the characteristic behavior of an antiferromagnetic system. The absence of hysteresis behavior also demonstrates the absence of uncompensated antiferromagnetic moments, the presence of spin impurities and the presence of ferromagnetic coupling at this temperature range.

Fig. 5.13 shows the M–H behaviour of $FeAl_2$ around the magnetic transition at T^*. As can be seen, the M–H behavior below T^* is identical with that below T_N. M–H curve remained linear up to the highest applied field of 50 kOe and no hysteresis was

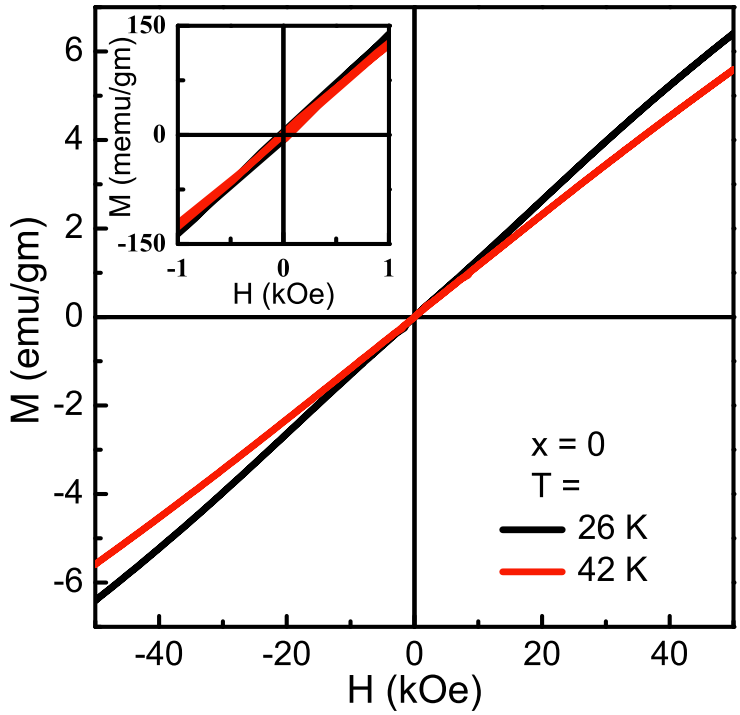

Figure 5.13: (a) M–H curve of $FeAl_2$ ($x = 0$) measured around T^*. Inset show the enlarged view of the M–H curves near the origin

present as can be seen from the inset graph. These behaviors further confirm that the similarity between T^* and T_{sg}.

5.4.2 AC susceptibility

Temperature and frequency dependences of ac susceptibilities of $FeAl_{2-x}Ga_x$ are shown in Figs. 5.14(a)–(c). As can be seen from the figures, characteristic behaviors of the ac susceptibilities are similar to the dc magnetizations shown in Fig. 5.4 and the transition temperatures T_N and T_{sg} are also clearly identifiable.

The enlarged view of the ac susceptibilities around T_{sg} are shown in separate inset graphs in Figs. 5.14(a)–(c). The cusp like behavior of ac susceptibility expected for a spin glass transition is present in all compositions. The cusp also shifts to higher temperatures with increasing frequency of ac field in all cases which is also a typical

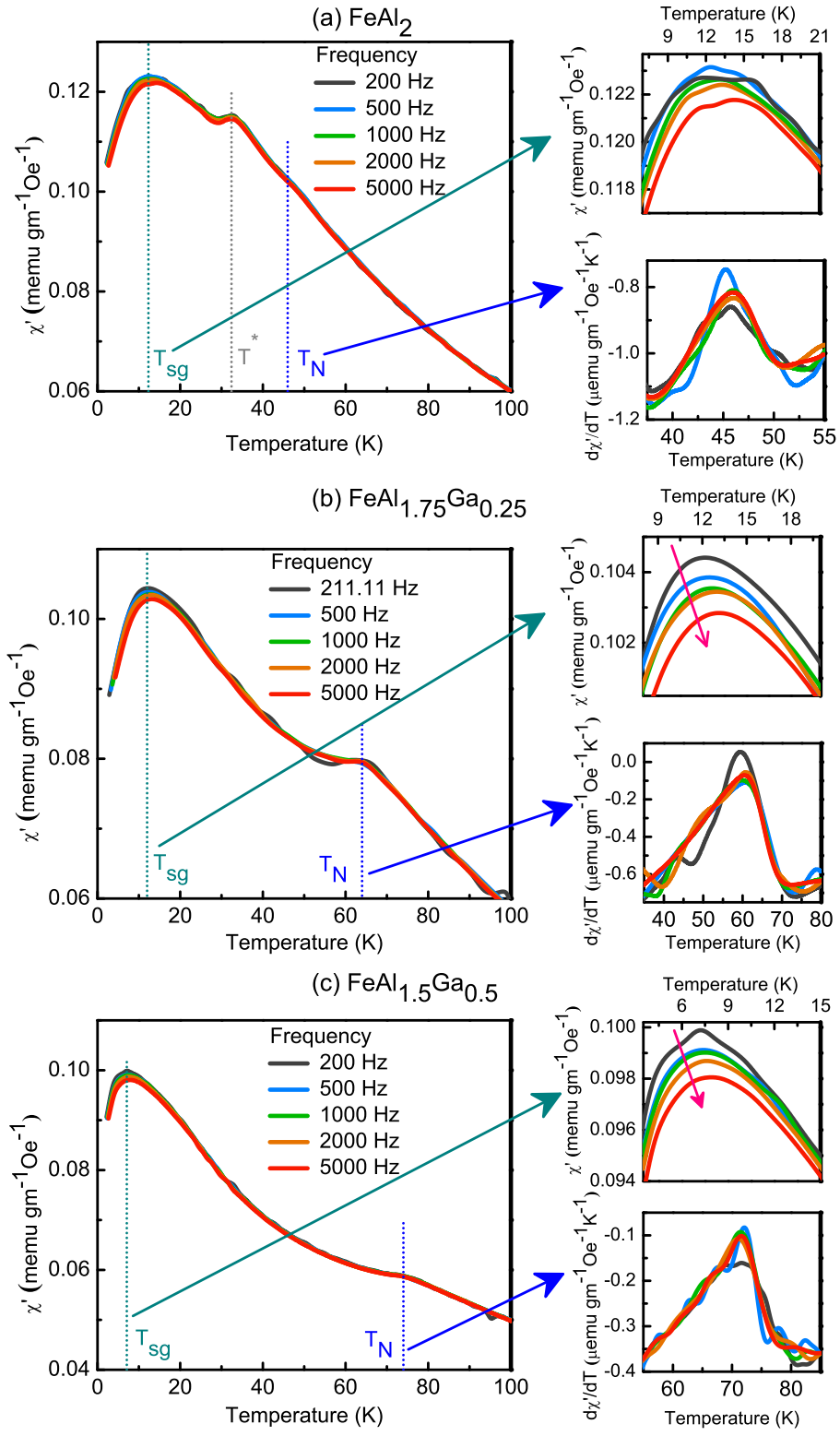

Figure 5.14: (a)–(c) Temperature and frequency dependences of the real part (χ') of ac susceptibility of $FeAl_{2-x}Ga_x$. Insets of (a), (b), and (c) show the frequency dependence of χ' around the spin glass transition T_{sg} and $d\chi'/dT$ around the antiferromagnetic transition T_N.

characteristic of a spin glass system. The values of ϕ $(= \Delta T_{sg}/(T_{sg} \log f))$, which is a quantitative measure of the shift of T_{sg} with frequency f, were found to be 0.079, 0.061 and 0.068 for the compositions $x = 0.00, 0.25$ and 0.50, respectively. These values of ϕ are similar to those of localized moment spin glass systems [26]. In a previous study Chi et al. [56] concluded that Fe moments in $FeAl_2$ are partially localized. Therefore, the values of ϕ we obtained indicating the localized nature of Fe magnetic moments in these alloys are in accordance with the previous studies.

AC susceptibilities did not show any sharp maximum around T_N similar to dc magnetizations. Only a broad hump or inflection point could be visible in this region. Frequency dependence of the corresponding magnetic transition at T_N could not be determined in the absence of a clear local maximum. However, $d\chi'/dT$ shows maximum at T_N. $d\chi'/dT$ of $FeAl_{2-x}Ga_x$ around T_N at different frequencies are shown in separate inset graphs in Figs. 5.14(a)–(c). As can be seen from these figures, the maximum in $d\chi'/dT$ does not show any frequency dependent shift in temperature in any of the compositions and further confirms the antiferromagnetic nature of this transition at T_N.

In addition, similar to dc magnetizations, a hump at T^* is present in the ac

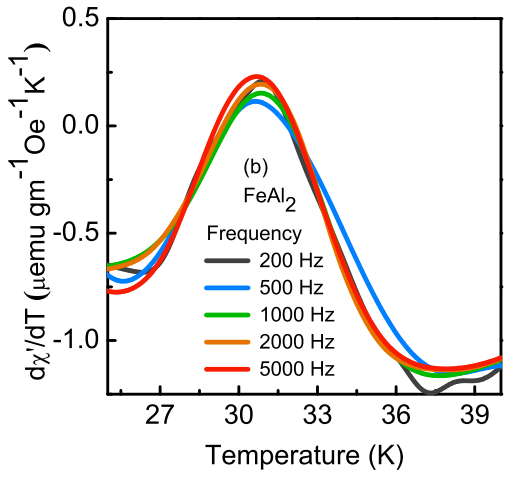

Figure 5.15: Frequency dependence of $d\chi'/dT$ in $FeAl_2$ $(x = 0)$ around the magnetic transition at T^*.

susceptibilities of the composition $x = 0$ (i.e., $FeAl_2$). $d\chi'/dT$ around T^* at different frequencies are shown in Fig. 5.15. Similar to the behaviour of $d\chi'/dT$ around T_N, $d\chi'/dT$ around T^* does not show any frequency dependent shift of T^* and indicate the identical nature of the magnetic transitions at T_N and T^*.

5.5 Specific heat

Temperature variation of specific heat C_P is shown in Fig. 5.16 that shows a small hump at the antiferromagnetic transition temperature T_N in all compositions.

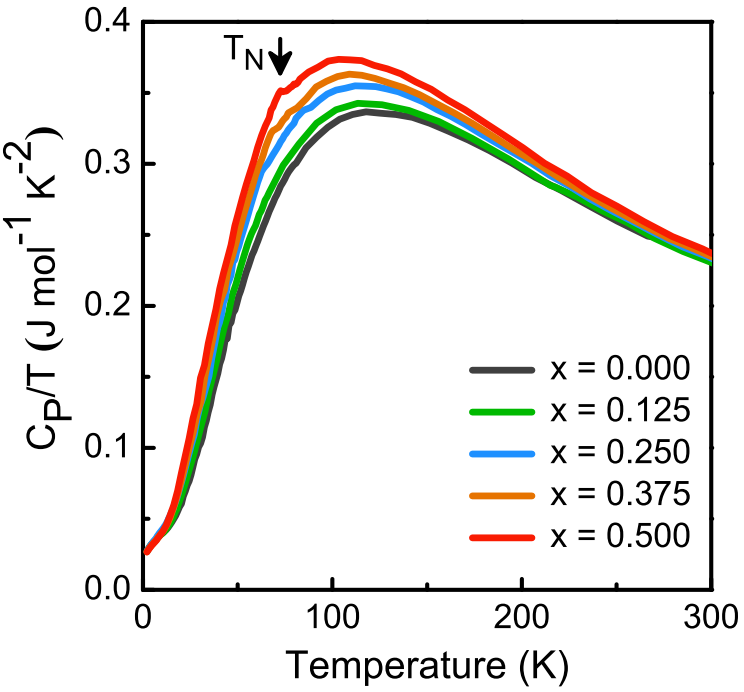

Figure 5.16: Temperature variations of C_P/T of $FeAl_{2-x}Ga_x$.

In normal metallic systems, the total specific heat (C_P) comprises contributions of electronic specific heat (C_{elec}) from conduction electrons of the system and lattice specific heat (C_{lat}) from atomic vibrations. At low temperature, $C_{elec} = \gamma T$, where γ is related to electronic density of states at Fermi level $D(E_F)$ as $\gamma = \frac{\pi^2 k_B^2 D(E_F)}{3}$, constitutes a

significant portion of C_P. The temperature dependence of C_{lat} is given by Debye model:

$$C_{lat} = 9Nk_B\left(\frac{T}{\theta_D}\right)^3 \int_0^{\theta_D/T} \frac{x^4 e^x}{(e^x-1)^2} dx \tag{5.3}$$

where N is the number of atoms in the solid, k_B is the Boltzmann constant and θ_D is the Debye temperature. At low temperature $T \ll \theta_D$, Eq. 5.3 can be written as:

$$C_{lat} = \frac{12Nk_B\pi^4}{5}\left(\frac{T}{\theta_D}\right)^3 \tag{5.4}$$

Therefore, at low temperature $T \ll \theta_D$, the total specific heat C_P can be expressed as:

$$C_P(T) = \gamma T + \beta T^3 \tag{5.5}$$

where $\beta = \frac{12Nk_B\pi^4}{5\theta_D^3}$.

In addition to C_{elec} and C_{lat}, C_P also contains the magnetic contribution C_{mag} which changes when the system goes through a magnetic phase transition. From the magnetic properties discussed in Sec. 5.4, it is now clear that the magnetic states of the $FeAl_{2-x}Ga_x$ ($0 \leq x \leq 0.5$) alloys are spin glass at low temperature and they are anti-ferromagneic in the intermediate temperature range. The magnetic part of the specific heat, C_{mag}, can be extracted by subtracting C_{lat} and C_{elec} from C_P. We fitted the specific heat data of $FeAl_{2-x}Ga_x$ above T_{sg} but below 25 K with Eq. 5.5 to estimate C_{elec} and

Table 5.5: Values of γ and θ_D obtained from the fitting of specific heat data of $FeAl_{2-x}Ga_x$ with Eq. 5.5.

Ga concentration (x)	γ (mJ mol^{-1} K^{-2})	θ_D (K)
0.000	27.5(9)	412(3)
0.125	25.7(3)	389(1)
0.250	28.0(3)	369.7(7)
0.375	24.9(4)	358.6(8)
0.500	22(1)	344(2)

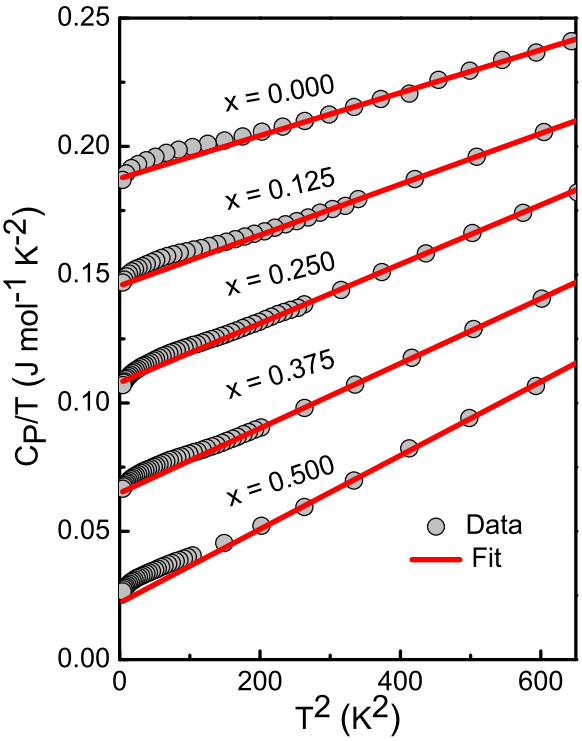

Figure 5.17: C_p/T vs. T of $FeAl_{2-x}Ga_x$ at low temperatures and fit with Eq. 5.5.

C_{lat}. The fits are shown in Fig. 5.17 and the obtained parameters are listed in Table 5.5. The obtained value of $\theta_D = 412$ K for the composition $x = 0$ (i.e. $FeAl_2$) agrees well with the value reported earlier by Chi et al. from NMR measurement. The estimated values of C_{elec} and C_{lat} were then subtracted from the specific heat data to obtain C_{mag} at low temperature. The temperature variations of so obtained C_{mag} are shown in Figs. 5.18(a)–(e). A broad maximum is present around T_{sg} in all compositions. The presence of this broad maximum in C_{mag} around T_{sg} is a characteristic feature of spin glass systems.

The antiferromagnetic transitions in $FeAl_{2-x}Ga_x$ are at a considerably higher temperature where C_P contains a sizable non-linear contribution. The values of C_{elec} and C_{lat} obtained from the fit of low temperatures specific heat data with Eq. 5.5 cannot be used to extract C_{mag} around T_N. An alternate procedure of extracting C_{mag} is to compare C_P data to that of a non-magnetic reference substance of identical crystal structure. However, to the best of our knowledge, no such non-magnetic analog of

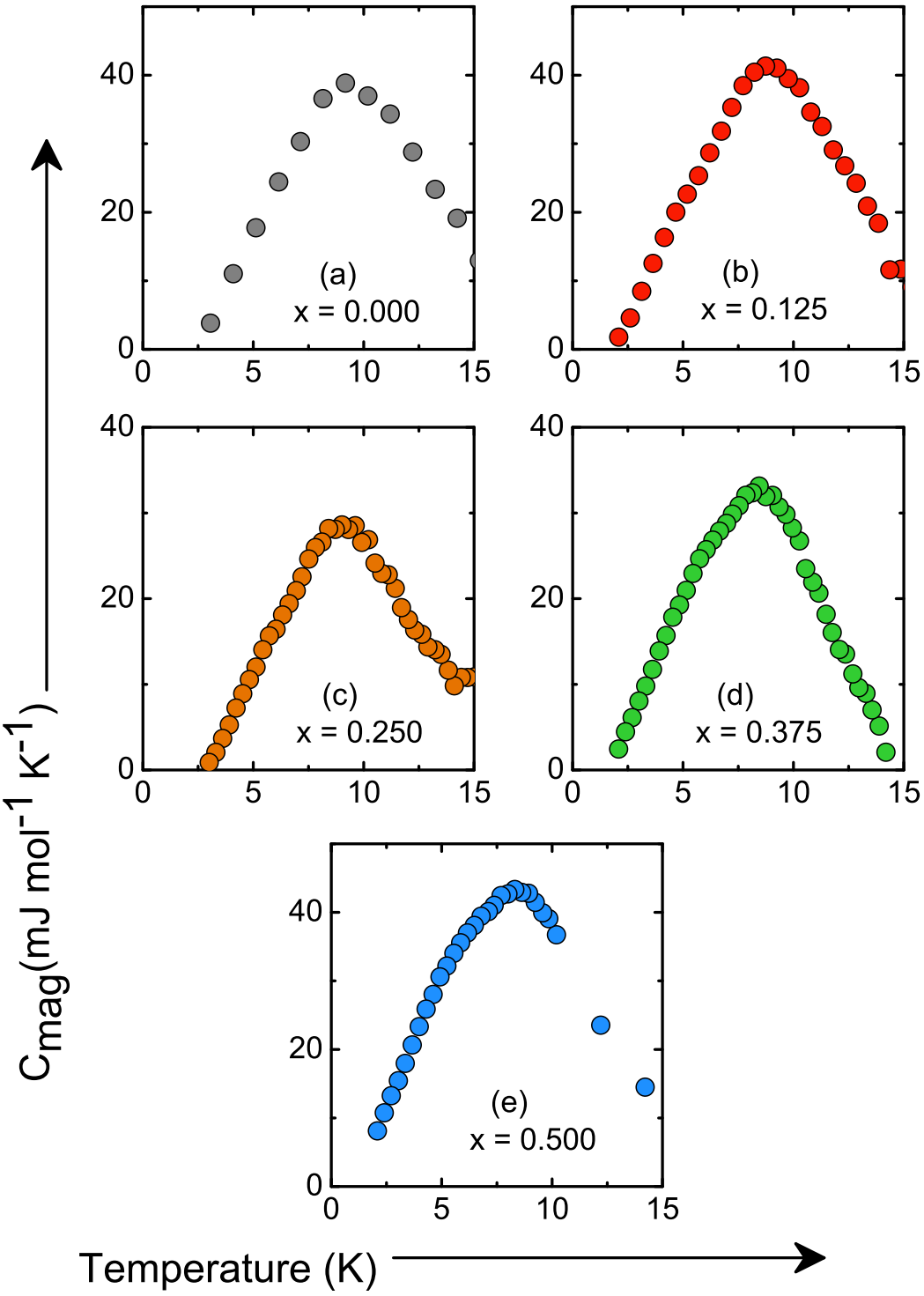

Figure 5.18: (a)–(e) Temperature variations of C_{mag} of $FeAl_{2-x}Ga_x$ at low temperatures.

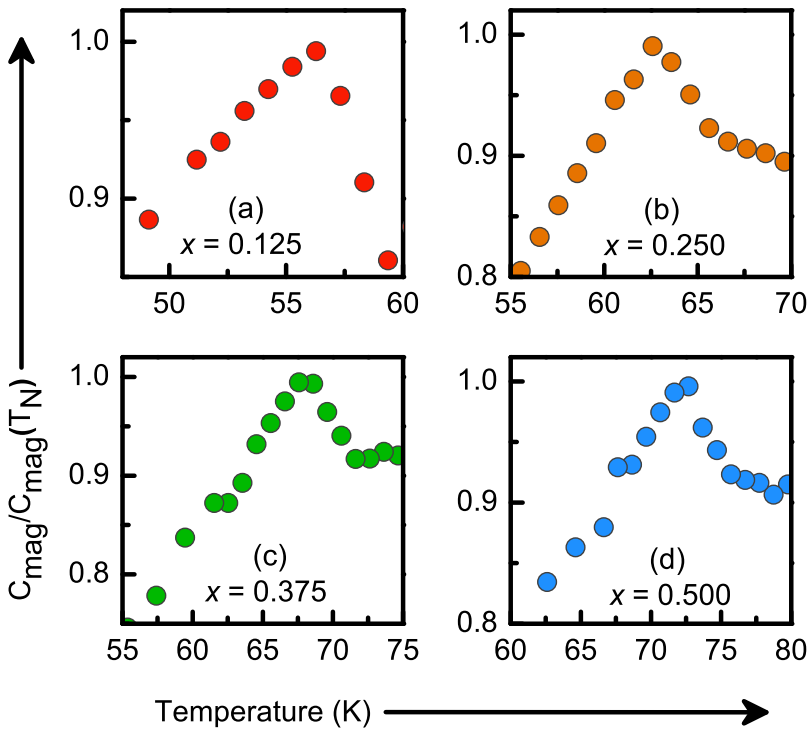

Figure 5.19: (a)–(d) C_{mag} around the antiferromagnetic transition T_N of $FeAl_{2-x}Ga_x$.

$FeAl_{2-x}Ga_x$ is known at present. The extraction of C_{mag} around the antiferromagnetic transition of $FeAl_{2-x}Ga_x$ thus seems almost impossible due to the above difficulties. However, the crystal structure of $FeAl_{2-x}Ga_x$ remains unaltered with the variation of Ga concentration in the concentration range $0 \leq x \leq 0.5$ while the antiferromagnetic transition temperature T_N shifts to higher temperatures. In addition, the temperature variation of C_{mag} is generally a λ-type peak across antiferromagnetic transition for which it rapidly decreases to zero above the transition. Therefore, from the above facts we can infer that the specific heat of the composition $x = 0$ has mainly phonon contribution in the temperature range where the $x > 0$ compositions have their antiferromagnetic transition and we can extract C_{mag} of the $x > 0$ compositions around the antiferromagnetic transition by subtracting the specific heat data of the $x = 0$ composition. The variations of so obtained C_{mag} of the $x > 0$ compositions with temperature are shown in the Figs. 5.19(a)–(d). A peak corresponding to the antiferromagnetic transition is clearly

discernible in all the compositions.

Here it should be noted that C_{mag} obtained by the above procedure is approximate only. There certainly are short-range magnetic ordering above T_N in the $x = 0$ composition and as well as in the $x \neq 0$ compositions which contributes to the specific heat. Also, in the above procedure, the extraction of C_{mag} of the $x = 0$ composition is not possible. However, even with all these limitations, the antiferromagnetic transition of the $x \neq 0$ compositions could be seen from the temperature variation of C_{mag}. The variation of T_N, obtained from the temperature variation ZFC magnetization and C_{mag}, with Ga concentration is shown in Fig. 5.20 which also highlights good agreement in the obtained values of T_N from magnetization and specific heat data.

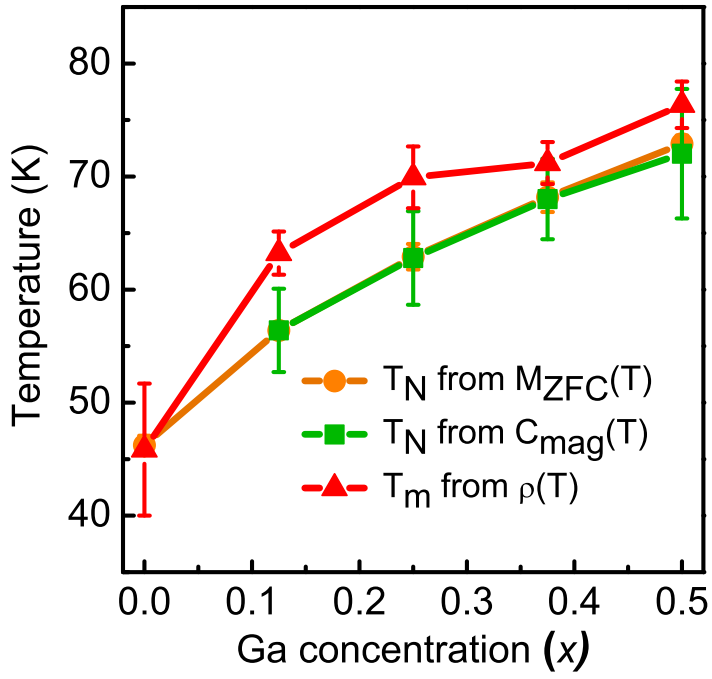

Figure 5.20: Variation of T_N, obtained from the temperature variations of ZFC magnetization M_{ZFC} and C_{mag}, and T_m with the Ga concentration in $FeAl_{2-x}Ga_x$.

5.6 Resistivity

Electrical resistivities (ρ) of the $FeAl_{2-x}Ga_x$ ($0 \leq x \leq 0.5$) alloys were measured in the temperature range 4 K – 300 K. The temperature variations of ρ of $FeAl_{2-x}Ga_x$ are shown in Fig. 5.21 in the normalized form $r(T) = \rho(T)/\rho(T = 4\text{ K})$. The values of ρ at T = 4 K are listed in Table 5.6.

Table 5.6: Resistivity (ρ) values of $FeAl_{2-x}Ga_x$ at T = 4 K.

Ga concentration (x)	ρ(T = 4 K) (μΩ-cm)
0.000	809(20)
0.125	1455(59)
0.250	1532(47)
0.375	1167(33)
0.500	1695(64)

ρ as a function of temperature shows a minimum in all compositions as shown in Fig. 5.21. The variation of T_m, the temperature at which the resistivity minimum appears, with Ga concentration is shown in Fig 5.20. The most astonishing observation is that $T_m \approx T_N$, i.e., the resistivity minimum occurred concomitantly with the antiferromagnetic transition.

Resistivity minimum in disordered alloys could arise due to a variety of reason (e.g., weak localization, Kondo effect etc. as discussed in Sec. 1.3), however, the simultaneous antiferromagnetic transition is quite unexpected. Out of these alloys, only resistivity of the composition $x = 0$ (i.e., $FeAl_2$) have been studied before by Lue et al. In their study, Lue et al. also found that a resistivity minimum appears in the temperature variation of resistivity of $FeAl_2$ and reported that $T_m \approx 43$ K which agrees well with the value (≈ 46 K) that we found here in this study.

Kondo effect, as discussed in Sec. 1.3.4 is one of the most common reasons which causes resistivity minimum at low temperatures in metals due to scattering of

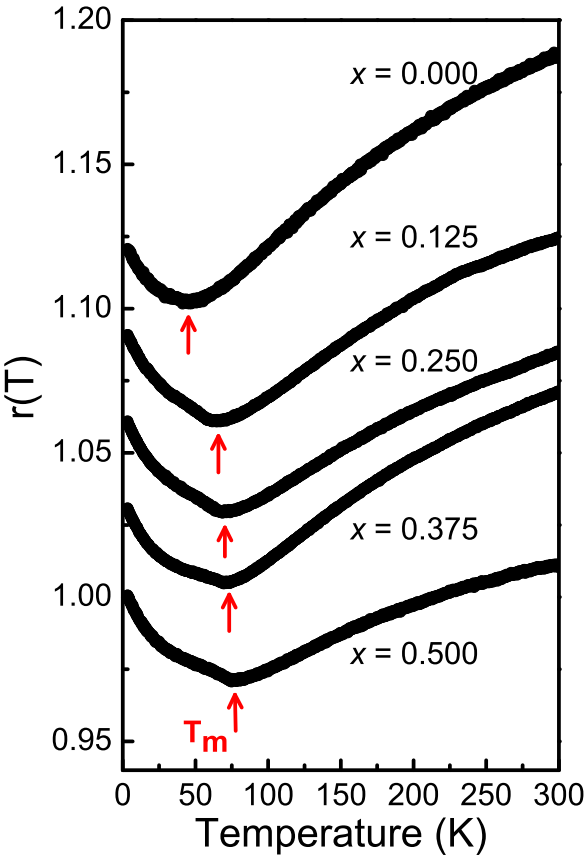

Figure 5.21: Electrical resistivity of $FeAl_{2-x}Ga_x$ as a function of temperature. The vertical arrows indicate T_m, the temperature at which the resistivity minima appears. Graphs are successively shifted from the $x = 0.5$ composition data by 0.03 on the Y-scale for clarity.

conduction electrons by isolated and dilute magnetic impurities. In such a scenario, $\rho(T) \sim \ln(T)$ at temperatures below T_m. However, Lue et al. [55] reported that $\rho(T) \sim \sqrt{T}$ below T_m in the composition $x = 0$. We also found that $\rho(T) \sim \sqrt{T}$ (shown in Fig. 5.22) in all the compositions which are in accordance with the observation made by Lue et al. These observed temperature variations of resistivity are in marked contrast to what expected for Kondo effect and therefore the possibility that Kondo effect is the origin of resistivity minimum in $FeAl_{2-x}Ga_x$ can be discarded and we must look into other effects for which a resistivity minimum could appear in disordered bulk alloys.

Quantum corrections in conductivity arising out of weak localization (WL) and disorder-enhanced electron-electron interactions (EEI) in disordered solids are other possible reasons as discussed in Sec. 1.3.2. The contribution to resistivity from EEI ef-

fect (ρ_{EEI}) due to diffusive motion of electrons causes an resistivity upturn which is proportional to $\sqrt{T}$ (i.e, $\rho_{EEI} \sim \sqrt{T}$). The temperature variation of resistivity contribution from WL effect (ρ_{WL}) is linearly related to $T^{p/2}$ where the index p depends on the inelastic scattering mechanism that dominates the given temperature range. $p = 2$ when the inelastic electron scattering is dominated by electron-electron scattering and $p = 3$ when electron-phonon scattering is the dominant inelastic scattering process. Both these two mechanisms of quantum corrections generally coexist in disordered solids. However, ρ_{EEI} dominates over ρ_{WL} at low temperatures since the value of the index p in ρ_{WL} is always greater than *one* in three-dimensional solids. The observation made by Lue at al. as well as our observation of the temperature variation of resistivity at low temperature (shown in Fig. 5.22) indeed indicates the dominance of ρ_{EEI} in $FeAl_{2-x}Ga_x$ at very low temperatures. Therefore, the resistivity data of $FeAl_{2-x}Ga_x$ at low temperature were fitted with the equation below:

$$r(T) = r_0 - a_{EEI}\sqrt{T} \tag{5.6}$$

where $\rho_0 = r_0\rho(T = 4\ \text{K})$ is the temperature independent part of the resistivity and $a_{EEI}\rho(T = 4\ \text{K})$ is the coefficient of the EEI effects induced resistivity. The fits are shown in Fig. 5.22 and the parameters obtained from the fit are listed in Table 5.7. As can be seen from Fig. 5.22, ρ_{EEI} almost entirely accounts for the resistivity of $FeAl_{2-x}Ga_x$ nearly up to 20 K.

Table 5.7: Values of the parameters r_0 and a_{EEI} obtained from the fitting of Eq. 5.6 with resistivity data of $FeAl_{2-x}Ga_x$.

Ga concentration (x)	Fit range	r_0	a_{EEI}
0.000	4 K – 20 K	1.0103(2)	0.00493(6)
0.125	4 K – 20 K	1.0112(1)	0.00544(4)
0.250	4 K – 20 K	1.0115(1)	0.00570(3)
0.375	4 K – 20 K	1.01095(9)	0.00544(2)
0.500	4 K – 20 K	1.0108(2)	0.00548(4)

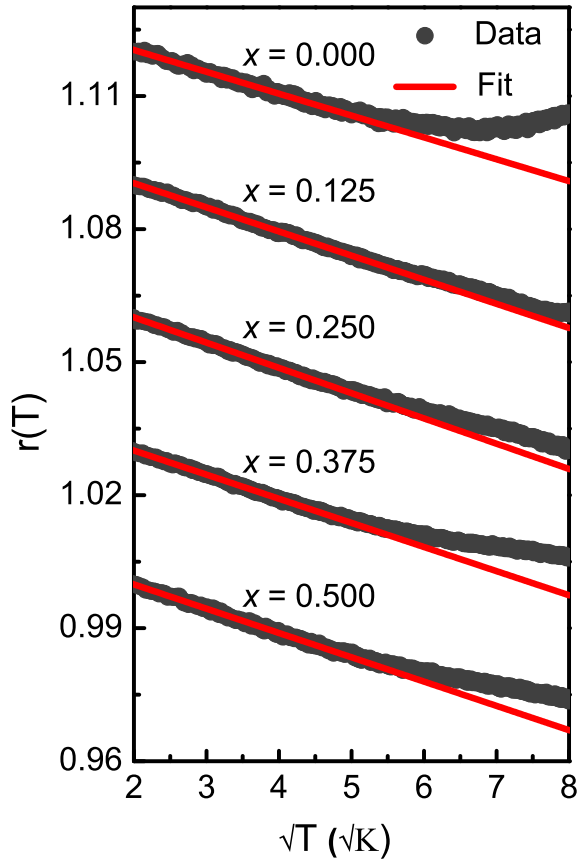

Figure 5.22: Variations of ρ of $FeAl_{2-x}Ga_x$ with $\sqrt{T}$ at low temperatures and the fit with electron-electron interactions induced resistivity ρ_{EEI}. Graphs are successively shifted from the $x = 0.5$ composition data by 0.03 on the Y-scale for clarity.

With increasing temperature, the dominance of ρ_{WL} over ρ_{EEI} gradually increases as the exponent of T in the expression of ρ_{WL} is larger than that in ρ_{EEI}. The change from ρ_{EEI} dominated region to ρ_{WL} dominated region can be seen from the deviation of $\rho(T)$ from the $\sqrt{T}$ dependence in Fig. 5.22 and from the change of slope in resistivity curve shown in Fig. 5.21. The underlying scattering processes of ρ_{WL} and ρ_{EEI} are elastic in nature. In addition to these elastic scatterings of electrons, we also have the inelastic scattering processes like electron-electron, electron-phonon, spin-orbit scattering. As the temperature increases, the rate of these inelastic scattering processes increases. These inelastic scatterings destroy the phase coherence, and therefore electron localization gradually dies out with increasing temperature and

the classical Boltzmann (ballistic) transport behavior gets restored above the resistivity minimum. In normal metals, dominant inelastic scattering contributions to resistivity come from electron-electron (ρ_{e-e}) and electron-phonon (ρ_{e-ph}) inelastic scattering processes. While ρ_{e-e} dominates over ρ_{e-ph} at low temperatures, the role gets reversed at intermediate and high temperatures. In presence of a strong electron correlation, ρ_{e-e} dominates over ρ_{e-ph} up to a significantly higher temperature. The role of electron correlation in determining the physical properties of Fe-Al alloy system evolves as the Al concentration changes. On the Fe-rich part of the phase diagram, electron correlation effects are nearly insignificant for the temperature range in which we have measured the resistivity in this study. As the Al concentration increases, electron correlation effects

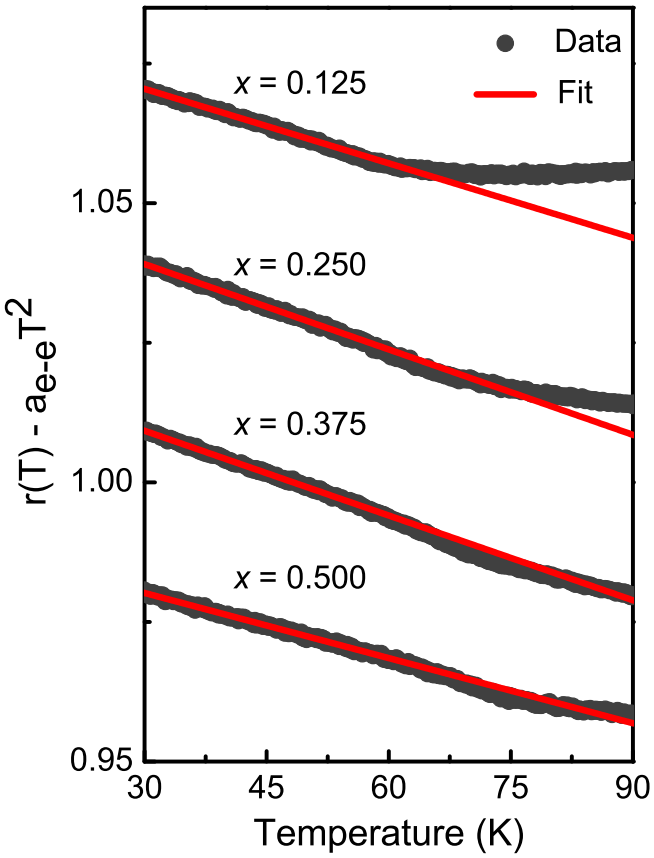

Figure 5.23: Temperature variation of ρ of $FeAl_{2-x}Ga_x$ at temperatures between the resistivity minimum and ρ_{EEI} dominated region, and the fit with Eq. 5.7. Graphs are successively shifted from the $x = 0.5$ composition data by 0.03 on the Y-scale for clarity.

Table 5.8: Values of the parameters r_0, a_{WL} and a_{e-e} obtained from the fitting of resistivity data of $FeAl_{2-x}Ga_x$ using Eq. 5.7.

Ga concentration (x)	Fit range	r_0	a_{WL}	a_{e-e}
0.000	–	–	–	–
0.125	27.5 K – 50 K	0.9938(7)	$4.4(4) \times 10^{-4}$	$1.3(5) \times 10^{-6}$
0.250	30 K – 55 K	0.9944(7)	$5.1(4) \times 10^{-4}$	$2.3(4) \times 10^{-6}$
0.375	30 K – 57.5 K	0.9944(4)	$5.1(2) \times 10^{-4}$	$3.6(2) \times 10^{-6}$
0.500	30 K – 60 K	0.9919(6)	$3.9(3) \times 10^{-4}$	$1.8(3) \times 10^{-6}$

become increasingly important. It's role in determining the magnetic ground state of equiatomic B2 FeAl have garnered significant debate which still continues [133, 134]. On the Al-rich part of the Fe-Al phase diagram, the intermetallic compound Fe_2Al_5 has a large electronic specific heat coefficient (83 mJ mol^{-1} K^{-2}) [184]. Consistent with these reports, we also found that the value of electronic specific heat coefficient $\gamma \sim 25$ mol^{-1} K^{-2} (as discussed in Sec. 5.5) in $FeAl_{2-x}Ga_x$ which is an order of magnitude larger than typically expected for a normal $3d$ intermetallic system. Therefore, resistivity data in the temperature range below the resistivity minimum but above the ρ_{EEI} dominated region were fitted considering contributions of $\rho_{WL} \sim T^{p/2}$ and $\rho_{e-e} \sim T^2$:

$$r(T) = r_0 - a_{WL}T^{p/2} + a_{e-e}T^2 \tag{5.7}$$

where $a_{WL}\rho(T = 4\text{ K})$ is the coefficient of the weak localization correction to resistivity and $a_{e-e}\rho(T = 4\text{ K})$ is the coefficient of inelastic electron-electron scattering induced resistivity. Fits of resistivity data with the above considerations are shown in Fig. 5.23 which depicts a good agreement. The parameters obtained from the fitting are tabulated in Table 5.8. The temperature range between the resistivity minimum and ρ_{EEI} dominated region is very small, particularly in the composition $x = 0$. This precludes such a fit with reliable fitting parameters for the composition $x = 0$.

Normalized resistivity $r(T) = \rho(T)/\rho(T = 4\text{ K})$ of $FeAl_{2-x}Ga_x$ above T_m is shown in Fig. 5.24 in the scale of T^2 which depicts a linear relation between $r(T)$

and T^2. However, T^2 dependence of resistivity at this temperature range has a different origin than inelastic electron-electron scatterings described for the intermediate temperature range. Such inelastic electron-electron scatterings are in general not the dominating contributions over inelastic electron-phonon scattering at this high temperatures. In this region of temperature, inelastic electron-phonon scattering induced resistivity ρ_{e-ph} should be so large that it would dominate over any other contributions present in the system. In ordered metals and alloys, ρ_{e-ph} is known to vary with temperature as T^5 (Bloch–Grüneisen formula) or T^3 (Bloch–Wilson formula when *s-d* electron scattering is present such as in transition metal and alloys) for $T \ll \theta_D$. However, when electrons scatter from the potential of a disordered lattice, such as in amorphous and disordered

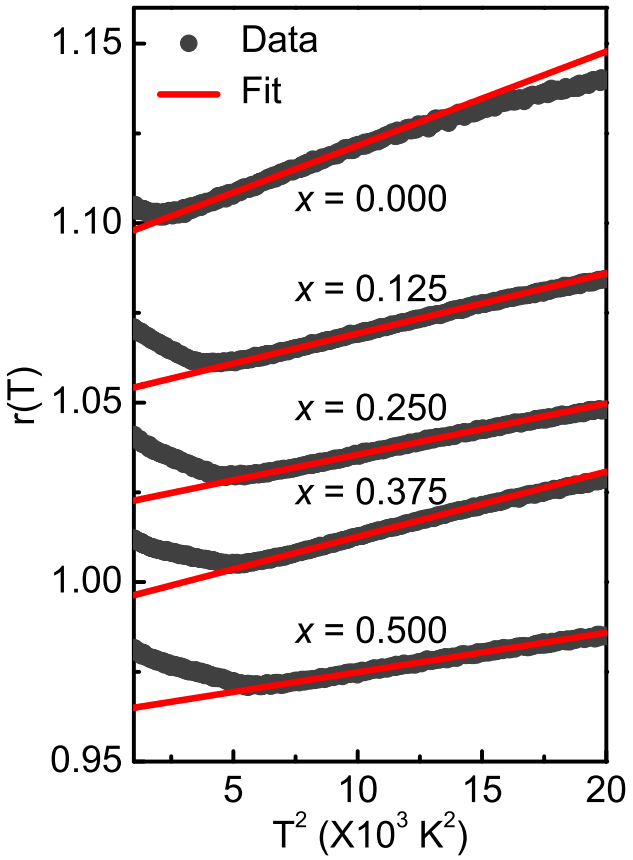

Figure 5.24: Temperature variations of ρ of $FeAl_{2-x}Ga_x$ above the resistivity minimum and the fit with inelastic electron-phonon scattering induced resistivity ρ_{e-ph}. Graphs are successively shifted from the $x = 0.5$ composition data by 0.03 on the Y-scale for clarity.

alloys, the temperature dependence of resistivity is given by diffraction model which can be expressed as [185–189]:

$$r_{e-ph}(T) = a_1 + a_2 \exp\left[-8a_3 \left(\frac{T}{\theta_D} \right)^2 \int_0^{\theta_D/T} \frac{z dz}{e^z - 1} \right] \tag{5.8}$$

where a_1 and a_2 are given by the static structure factor $S_0(2k_F)$ (k_F is the Fermi wave vector) as $S_0(2k_F) = 1 + \frac{a_1}{a_2}$ and $a_3 = \frac{3\hbar^2 k_F^2}{2Mk_B\theta_D}$ (M is the atomic mass). For $T < \theta_D$, Eq. 5.8 can be approximated to show that $r_{e-ph} \sim T^2$. Therefore, resistivity of $FeAl_{2-x}Ga_x$ above the resistivity minimum were fitted with equation:

$$r(T) = r_0 + a_{e-ph} T^2 \tag{5.9}$$

where $a_{e-ph}\rho(T = 4\ \text{K})$ is the coefficient of inelastic electron-phonon scattering induced resistivity. The fits are shown in Fig. 5.24 and the parameters obtained from the fits are listed in Table 5.9.

Table 5.9: Values of the parameters r_0 and a_{e-ph} obtained from the fitting of resistivity data of $FeAl_{2-x}Ga_x$ using Eq. 5.9.

Ga concentration (x)	Fit range	r_0	a_{e-ph}
0.000	56.5 K – 100 K	0.97538(7)	$2.62(1) \times 10^{-6}$
0.125	80.5 K – 120 K	0.96253(5)	$1.672(5) \times 10^{-6}$
0.250	83.5 K – 122.5 K	0.96127(6)	$1.423(6) \times 10^{-6}$
0.375	83.5 K – 118 K	0.96453(6)	$1.812(5) \times 10^{-6}$
0.500	89.5 K – 126.5 K	0.96389(8)	$1.099(6) \times 10^{-6}$

5.7 Magnetoresistivity

WL and EEI effects both cause an increase in resistivity at low temperatures. The distinction between these two effects from the temperature variation of resistivity alone is then often ambiguous. However, WL and EEI effects have drastically differ-

ent responses to an applied magnetic field and therefore magnetoresistance (MR) can be used differentiate these two effects [190]. As discussed in Sec. 1.3.2, weak localization arises because of the constructive quantum interference between two counter-propagating electron waves traveling in a closed loop. In presence of a magnetic field, they acquire an extra phase difference which suppresses the interference effect. As the interference effect gets suppressed, resistivity increment due to weak localization becomes less when an external magnetic field is present, as compared to when there is no applied magnetic field. As a result, WL contribution to the magnetoresistance is *negative* and magnetoconductivity $\Delta\sigma(H,T) = \sigma(H,T) - \sigma(0,T)$ for bulk systems can be expressed as [191, 192]:

$$\Big[\Delta\sigma(H,T)\Big]_{WL} = \frac{e^2}{2\pi^2\hbar}\sqrt{\frac{eH}{\hbar c}}f(z) \tag{5.10}$$

where $z = \frac{\hbar c}{4eHL_{Th}^2}$, $L_{Th} = \sqrt{D\tau_{in}}$ is the Thouless length (τ_{in} is the mean free time for inelastic collision and D is the diffusion coefficient) and

$$f(z) = \sum_{n=0}^{\infty}\left[2\left(\sqrt{n+z+1} - \sqrt{n+z}\right) - \frac{1}{\sqrt{n+z+1/2}}\right] \tag{5.11}$$

In case of a weak magnetic field, $z \gg 1$ and then $f(z)$ is given by:

$$f(z) = \frac{1}{48}z^{-3/2} \tag{5.12}$$

However, in the limit of strong magnetic field $z \ll 1$ and then $f(z) = 0.605$. For strong magnetic field, $\Delta\sigma(H,T)$ is then can be written as:

$$\Big[\Delta\sigma(H,T)\Big]_{WL} = 0.918\sqrt{H}\ \text{mho/cm} \tag{5.13}$$

when H is expressed in kOe.

On the other hand, magnetoresistance contribution of EEI effect is *positive*

which comes from the splitting of spin-up and spin-down bands. Application of magnetic field causes spin splitting of the triplet state corresponding to $S_z = \pm 1$ of interacting electrons and introduces a gap $g\mu_B H$ between the lowest unoccupied spin-up electron and highest occupied spin-down electron. This spin splitting increases the resistivity of the system, and thereby produces *positive* magnetoresistance. $\Delta\sigma(H,T)$ for EEI effect is given by [24]:

$$\Big[\Delta\sigma(H,T)\Big]_{EEI} = -\frac{e^2\tilde{F}_\sigma}{4\pi^2\hbar}\sqrt{\frac{k_B T}{2D\hbar}}f(h) \tag{5.14}$$

where $h = \frac{g\mu_B H}{k_B T}$. For bulk systems in strong ($h \gg 1$) and weak ($h \ll 1$) weak magnetic field, $f(h)$ is given by:

$$f(h) = \begin{cases} \sqrt{h} - 1.3 \;\; (h \gg 1) \\ 0.053h^2 \;\; (h \ll 1) \end{cases} \tag{5.15}$$

From Eq. 5.13 and Eq.5.15, it is now clear that in case of a strong magnetic field, magnetoresistance contributions of both the WL and EEI effects vary linearly with $\sqrt{H}$. However, while the contribution of WL effect is *negative* EEI effect gives *positive* contribution to magnetoresistance.

The goal of this section is to find out whether weak localization is the origin of the resistivity minima in $FeAl_{2-x}Ga_x$. As can be seen from Fig. 5.22, resistivity of $FeAl_{2-x}Ga_x$ is dominated by EEI effects below 20 K. Therefore, magnetoresistances were measured above 20 K to avoid appreciable contributions from the EEI effects. The variation of $\Delta\sigma$ of $FeAl_{2-x}Ga_x$ with $\sqrt{H}$ in high magnetic field region at several temperatures and their linear fit are shown in Fig. 5.25. First, all the $\Delta\sigma$ are *positive* which substantiates that weak localization caused the observed resistivity minima in $FeAl_{2-x}Ga_x$. The obtained slope of the fitted curves are 0.77 for $x = 0.5$ at $T = 60$ K, 1.00 for $x = 0.5$ at $T = 40$ K, 1.31 for $x = 0.25$ at $T = 35$ K and 3.48 for $x = 0$ at $T = 28$ K which are close to the value expected according to Eq. 5.13 for magnetoconductivity variation due to weak localization at high magnetic field. However, the value for the

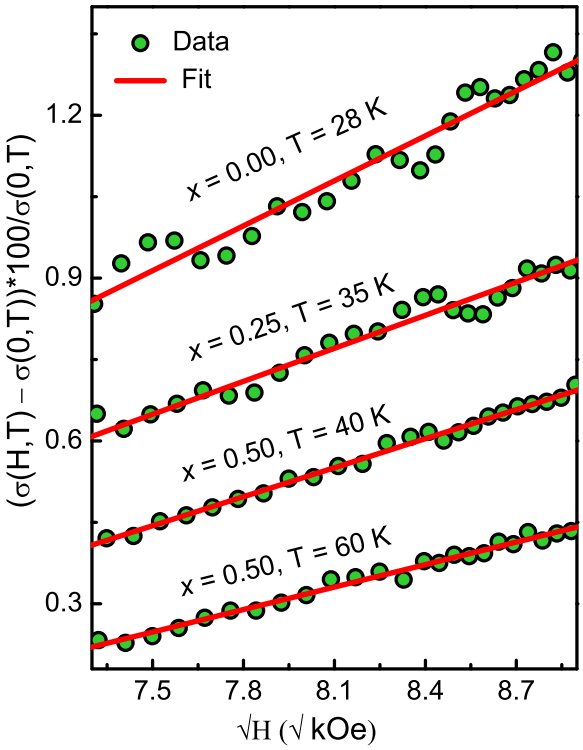

Figure 5.25: Variation of $\Delta\sigma$ with $\sqrt{H}$ in $FeAl_{2-x}Ga_x$ and straight line fit to the data. Graphs are successively shifted from the $x = 0.50$ at $T = 60$ K data by 0.15 on the Y-scale for clarity.

composition $x = 0$ shows large deviation from the expected value which might be due to the proximity of another magnetic transition at $T^* \sim 32$ K.

5.8 Conclusions

In this chapter structural, magnetic and transport properties of $FeAl_{2-x}Ga_x$ ($0 \leq x \leq 0.5$) have been discussed in details. Analysis of the XRD patterns showed that when Ga atoms are added to the triclinic aP19 structure of $FeAl_2$, they preferably occupy the position of Al atoms and increases substitutional disorder in the system with increasing Ga concentration. From the studies of dc magnetization and ac susceptibility, we have shown that the low temperature magnetic state of $FeAl_{2-x}Ga_X$ is a spin glass. A

paramagnetic to antiferromagnetic transition also occurs at intermediate temperatures and electrical transport measurement showed that this antiferromagnetic transition appears concomitantly with a resistivity minimum originating from weak localization of electrons. The weak localization origin of the resistivity minimum in $FeAl_{2-x}Ga_x$ has been further confirmed by the magnetoresistance measurements.

6 Electronic Structure and Magnetic Phase Diagram of Disordered $Au_{1-x}Cr_x$ Alloys

6.1 Introduction

The exploration of phase diagrams of newly synthesized alloys as well as the scrutiny of previously developed phase diagrams with more sophisticated experimental techniques and improved theoretical modelings constitute a major part of materials research. The magnetic phase diagram of disordered $Au_{1-x}Cr_x$ ($0 \leq x \leq 0.3$) alloy system is investigated in this chapter using mean field analysis of the magnetic exchange interaction parameters obtained from first-principles calculations to assess various experimental findings. The magnetic properties of this system have been explored by various methods like neutron diffraction, Mössbauer effect and magnetizations measurements [61, 193–200]. Nakai et al. [61] constructed the magnetic phase diagram based on these magnetic measurements and neutron diffraction studies, which illustrates that the low temperature magnetic state is a spin glass for $x < 0.1$ and a long-range antiferromagnetically ordered phase appears for $x > 0.15$. In the intermediate range between them, a mixed phase of spin glass and antiferromagnetic ordering occurs. Neutron diffraction studies [61, 196–198, 200] reveal that the Cr magnetic moments in the long-range antiferromagnetic state align ferromagnetically in one of the (100) planes, but align antiferromagnetically along the [100] axis. However, studying the magnetic susceptibility in the concentration region $0.13 \leq x \leq 0.18$, Radha et al. [62] later claimed that the cluster glass/spin glass behavior extends even up to the Cr concentra-

tion $x = 0.18$. We have scrutinized these experimental reports using mean field analysis of the magnetic exchange interaction parameters.

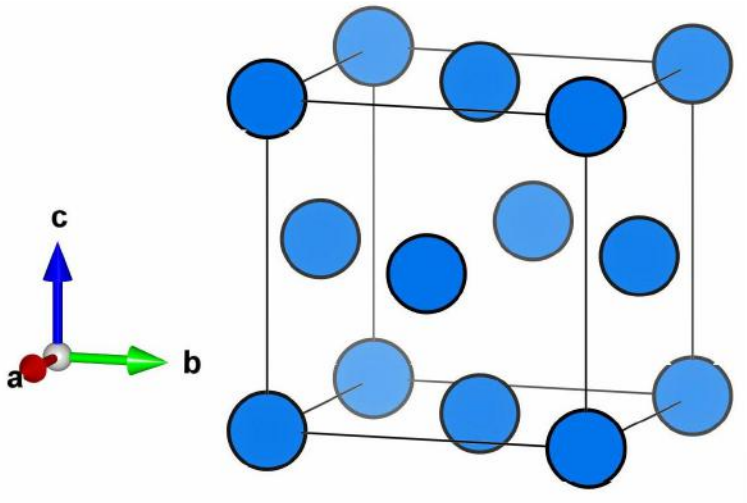

Figure 6.1: Depiction of FCC unit cell of space group $Fm\bar{3}m$.

In disordered antiferromagnetic alloys with close-packed structures, noncollinear spin ordering often occurs due to strong magnetic frustrations [63–68]. A computational package TB-LMTO-ASR [201, 202] has been recently developed in-house at our center by combining TB-LMTO [82] with ASR [83, 104] to study such noncollinear magnetic structures in disordered alloys. Disordered $Au_{1-x}Cr_x$ ($0 \leq x \leq 0.3$) alloys have face centered cubic (FCC) structure [61, 203] as shown in Fig. 6.1 (space group number and symbols are 225 and $Fm\bar{3}m$, respectively). The disorder here is substitutional type meaning that Au and Cr atoms randomly occupy the lattice sites with probability equal to their concentration in the system. FCC lattice is also a close-packed structure, and therefore the possible occurrence of such noncollinear magnetic structures in these alloys is also explored in this chapter using TB-LMTO-ASR.

6.2 Spin configuration and electronic structure

Experimental lattice parameter values are available only for a very few composition. Therefore, before proceeding to the calculations of electronic and magnetic properties, lattice parameter values were determined from the minimization of the total energy of the system for different Cr concentrations. Total energy was calculated for a series of lattice parameters to obtain the optimum value corresponding to the lowest total energy of the system. These total energy calculations were performed self-consistently using the generalized gradient approximation (GGA) [94] to the exchange-correlation functional. TB-LMTO-CPA with the Madelung contribution based on the screened Coulomb potential as proposed by Ruban and Skriver et al. [204, 205] was used for the total energy calculations. The lattice parameter vs total energy calculations were carried out for different compositions of $Au_{1-x}Cr_x$ in the range $0 \leq x \leq 0.3$. Fig. 6.2(a) depicts an exemplary variation of total energy with lattice parameter for the Cr concentration $x = 0.3$.

Fig. 6.2(b) shows the variation of lattice parameter with Cr concentration obtained from the minimization of total energy. The errors in the obtained lattice parameter values were estimated as the minimum of lattice parameter difference for which the total energy could be resolved within its error window. The lattice parameter values of different Cr concentrations expected according to the Vegard's law [206] are also shown in Fig. 6.2(b). Cr has a smaller atomic radius than Au, therefore lattice parameter decreases with increasing Cr concentration. Although the lattice parameter values obtained from the total energy minimizations agree well with the Vegard's law within the error window for Cr concentrations $x < 0.1$, the increasing deviation from Vegard's law with the increase in Cr concentration is evident from Fig. 6.2(b). The size mismatch between the Au and Cr atoms leads to this increasing deviation of lattice parameter from the Vegard's law as Cr concentration increases. Nakai et al. [197] reported the experi-

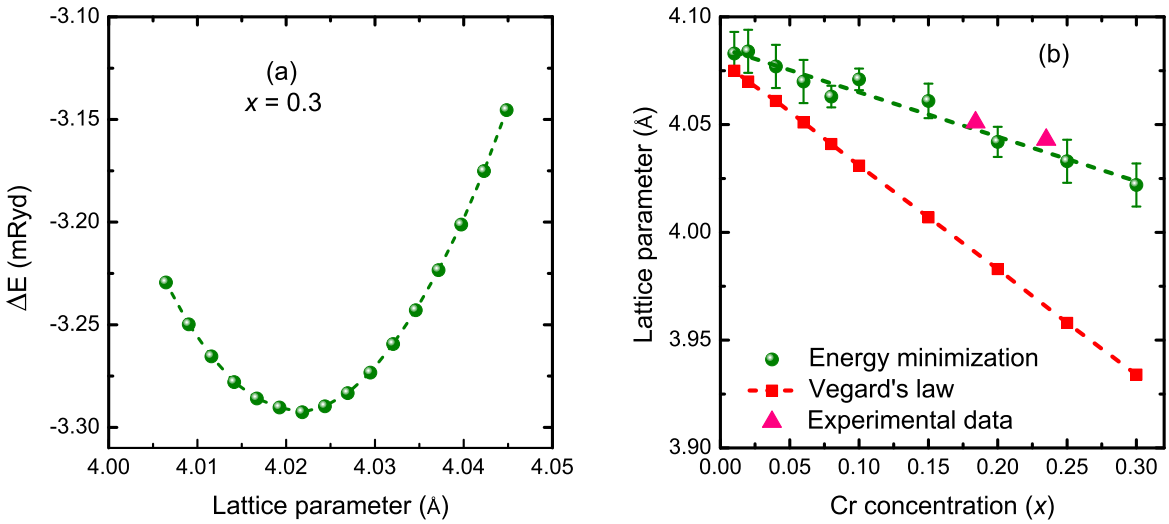

Figure 6.2: (a) Variation of energy ΔE for the Cr concentration $x = 0.3$ in disordered $Au_{1-x}Cr_x$ with lattice parameter. $E = \Delta E - 27297.99$, where E is the total energy in Rydberg. (b) Variation of lattice parameter of disordered $Au_{1-x}Cr_x$ alloy, obtained from total energy minimization and Vegard's law, with Cr concentration. The dotted lines are given as guide to the eye for a straight line. The triangles are the experimental data reported by Nakai et al. [197].

mental values of lattice parameter for the Cr concentrations $x = 0.184$ and 0.235. The obtained lattice parameter values from the total energy calculations agree excellently with the experimental report of Nakai et al. [197] as can be seen from Fig. 6.2(b).

After obtaining the lattice parameters from the minimization of total energy, the stability of various collinear and noncollinear spin configurations was explored using TB-LMTO-ASR [202]. Fig. 6.3 displays the choice of our magnetic primitive unit cell on a FCC lattice. Pictorial representation of the various collinear and noncollinear spin configurations, ferromagnetic (FM) and antiferromagnetic (AFM) 1Q, 2Q, and 3Q, explored are shown in Fig. 6.4.

The basic methodology of TB-LMTO-ASR has been described in Sec. 2.2.3.2. However, unlike the collinear case where we can define a global quantization axis, for noncollinear spin configurations we have a local quantization axis characterized by a unit vector $\mathbf{e}_{\mathbf{R}_i}(\theta_{\mathbf{R}_i}, \phi_{\mathbf{R}_i})$ in the atomic sphere labeled by $\mathbf{R}_i$ with respect to a set of

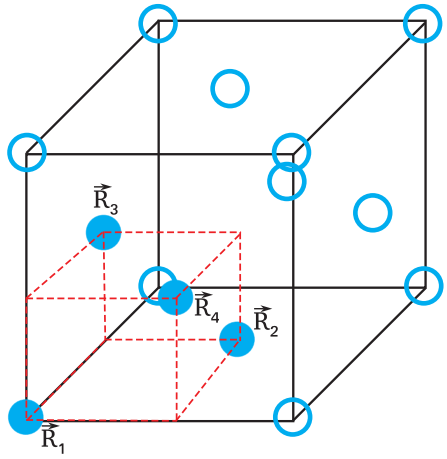

Figure 6.3: Depiction of magnetic primitive unit cell on a FCC lattice

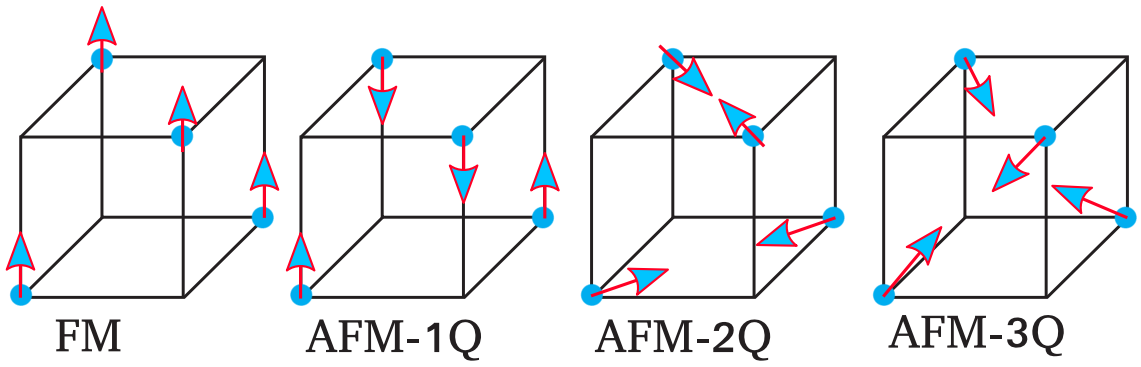

Figure 6.4: Ferromagnetic (FM) and antiferromagnetic (AFM) 1Q, 2Q, and 3Q spin configurations on the magnetic primitive lattice of a FCC structure.

suitably chosen global axes. Here we have chosen the positive c-axis as the global axis of quantization (z-axis). Two sites on the bottom x-y plane were labeled as $\mathbf{R}_1$, $\mathbf{R}_2$ and those on the top x-y plane were labeled as $\mathbf{R}_3$, $\mathbf{R}_4$ (shown in Fig. 6.3). The spherical angles for the different spin configurations are listed in Table 6.1.

Table 6.1: Coordinate details of the spins for FM and AFM 1Q, 2Q, and 3Q magnetic structures. Angles θ and ϕ are given in units of π.

Spin configuration	$\mathbf{R}_1$		$\mathbf{R}_2$		$\mathbf{R}_3$		$\mathbf{R}_4$	
	θ	ϕ	θ	ϕ	θ	Φ	θ	ϕ
FM	0	0	0	0	0	0	0	0
1Q	0	0	0	0	1	0	1	0
2Q	0.50	0.25	0.50	1.25	0.50	0.75	0.50	1.75
3Q	0.30	0.25	0.30	1.25	0.30	0.75	0.30	1.75

As described in Sec. 2.2.3.2, the augmented space theorem gives the averaged Green's function as:

$$\ll \mathbf{G}_{\mathbf{R}_i\mathbf{L},\mathbf{R}_j\mathbf{L}'}(E) \gg = \langle \mathbf{R}_i\mathbf{L}\{\emptyset\}| \left(E\tilde{\mathbf{I}} - \tilde{\mathscr{H}}\right)^{-1} \left|\mathbf{R}_j\mathbf{L}'\{\emptyset\}\right\rangle \tag{6.1}$$

where $\mathbf{R}_i$ label the lattice positions, $\mathbf{L}$ is the composite angular momentum index (l, m), and $\tilde{\mathscr{H}} \in \Psi = \mathscr{H} \otimes \Phi$ in which $\mathscr{H}$ is the Hilbert space spanned by the TB-LMTO basis $\left\{|\mathbf{R}_i\mathbf{L}\rangle\right\}$ and Φ is spanned by all configurations of the system. $|\{\emptyset\}\rangle$ is that state in Φ without any configuration fluctuations. The averaged projected and magnetic density of states are respectively given by:

$$\begin{aligned} \ll n_{\mathbf{R}_i\mathbf{L}}(E) \gg &= -\frac{1}{\pi}\mathrm{Im\ Tr}_\beta \left\{ \langle \mathbf{R}_i\mathbf{L}\{\emptyset\}| \widehat{\mathbf{G}}(E+i0) \left|\mathbf{R}_j\mathbf{L}'\{\emptyset\}\right\rangle \right\} \\ \ll \mathbf{m}_{\mathbf{R}_i\mathbf{L}}(E) \gg &= -\frac{1}{\pi}\mathrm{Im\ Tr}_\beta \left\{ \mathbf{S}\, \langle \mathbf{R}_i\mathbf{L}\{\emptyset\}| \widehat{\mathbf{G}}(E+i0) \left|\mathbf{R}_j\mathbf{L}'\{\emptyset\}\right\rangle \right\} \end{aligned} \tag{6.2}$$

where $\mathbf{S}$ is the spin operator in the spinor space. The averaged Green's functions were calculated as continued fraction by the recursion method in the full augmented space. The trace is over spinor space and in order to obtain a generalized noncollinear magnetization density the non-diagonal elements of the Green's function in the spinor space also need to be calculated [201]. At this point three recursions have to be carried out with the local quantization axis rotated in the x, y or z direction by SU(2) rotation matrices given by:

$$\mathbb{U} = \begin{bmatrix} e^{i\phi_{\mathbf{R}_i}/2}\cos\left(\theta_{\mathbf{R}_i}/2\right) & e^{-i\phi_{\mathbf{R}_i}/2}\sin\left(\theta_{\mathbf{R}_i}/2\right) \\ -e^{i\phi_{\mathbf{R}_i}/2}\sin\left(\theta_{\mathbf{R}_i}/2\right) & e^{-i\phi_{\mathbf{R}_i}/2}\cos\left(\theta_{\mathbf{R}_i}/2\right) \end{bmatrix}$$

A local spin axis is now defined under rigid moment approximation within an atomic sphere in which $\mathbf{S}_z$ is diagonal. The unitary SU(2) rotation operators $\mathbb{U}_x$, $\mathbb{U}_y$ and $\mathbb{U}_z = I$

then diagonalize $\mathbf{S}_x$, $\mathbf{S}_y$, and $\mathbf{S}_z$, respectively. Therefore,

$$\begin{aligned} \ll m^{\mu}_{\mathbf{R}_i\mathbf{L}}(E) \gg &= -\frac{1}{\pi}\mathrm{Im\ Tr}\Big\{\mathbf{S}^{\mu}\mathbb{U}^{\dagger}_{\mu}\mathbb{U}_{\mu}\left\langle \mathbf{R}_i\mathbf{L}\{\emptyset\}\right|\mathbf{G}(E)\left|\mathbf{R}_j\mathbf{L}'\{\emptyset\}\right\rangle\mathbb{U}^{\dagger}_{\mu}\mathbb{U}_{\mu}\Big\} \\ &= -\frac{1}{\pi}\mathrm{Im\ Tr}\Big\{\mathbf{S}'_{\mu}\left\langle \mathbf{R}_i\mathbf{L}\{\emptyset\}\right|\mathbf{G}'(E)\left|\mathbf{R}_j\mathbf{L}'\{\emptyset\}\right\rangle\Big\} \end{aligned} \tag{6.3}$$

and

$$\ll m^{\mu}_{\mathbf{R}_i} \gg = \sum_{\mathbf{L}}\int_{-\infty}^{E_F} dE \ll m^{\mu}_{\mathbf{R}_i\mathbf{L}}(E) \gg \tag{6.4}$$

Now, only the diagonal elements of $\left\langle \mathbf{R}_i\mathbf{L}\{\emptyset\}\right|\mathbf{G}'(E)\left|\mathbf{R}_j\mathbf{L}'\{\emptyset\}\right\rangle$ need to be calculated as $\mathbf{S}'_{\mu}$ are diagonal in spinor space.

For the Cr concentrations $x < 0.1$, disordered $Au_{1-x}Cr_x$ alloys are spin glasses at low temperatures in which both the directions of moments and position of the Cr atoms are random. For Cr concentrations in between $x = 0.10$ and $x = 0.15$, the system is in a mixed state of spin glass and antiferromagnetic phases. So, the Cr concentration range nearly up to $x = 0.15$ cannot be dealt with TB-LMTO-ASR. Therefore, self-consistent electronic structure and total energy calculations were carried out for the

Table 6.2: Relative energy differences of the FM, AFM-2Q, and AFM-3Q spin configurations from the AFM-1Q configuration and local magnetic moment μ_{Cr} of Cr atom in disordered $Au_{1-x}Cr_x$ alloys.

Cr concentration (x)	Spin configuration	Relative difference in total energy per atom (meV)	μ_{Cr} (μ_B)
x = 0.30	AFM-1Q	0	3.16
	AFM-2Q	39.6	3.15
	AFM-3Q	53.7	3.15
	FM	405.6	2.98
x = 0.25	AFM-1Q	0	3.22
	AFM-2Q	41.3	3.22
	AFM-3Q	55.4	3.22
	FM	345.8	3.12
x = 0.20	AFM-1Q	0	3.28
	AFM-2Q	41.3	3.29
	AFM-3Q	56.2	3.29
	FM	276.3	3.26

collinear and noncollinear spin configurations shown in Fig. 6.4 in the Cr concentration range $0.20 \leq x \leq 0.30$. Relative energy differences of various spin configurations from the AFM-1Q configuration and the local magnetic moment of Cr atom μ_{Cr} are listed in Table 6.2. As can be seen from the table, the AFM-1Q spin configuration has the lowest energy in all the compositions and is consistent with the earlier experimental reports from neutron diffraction studies [196, 197].

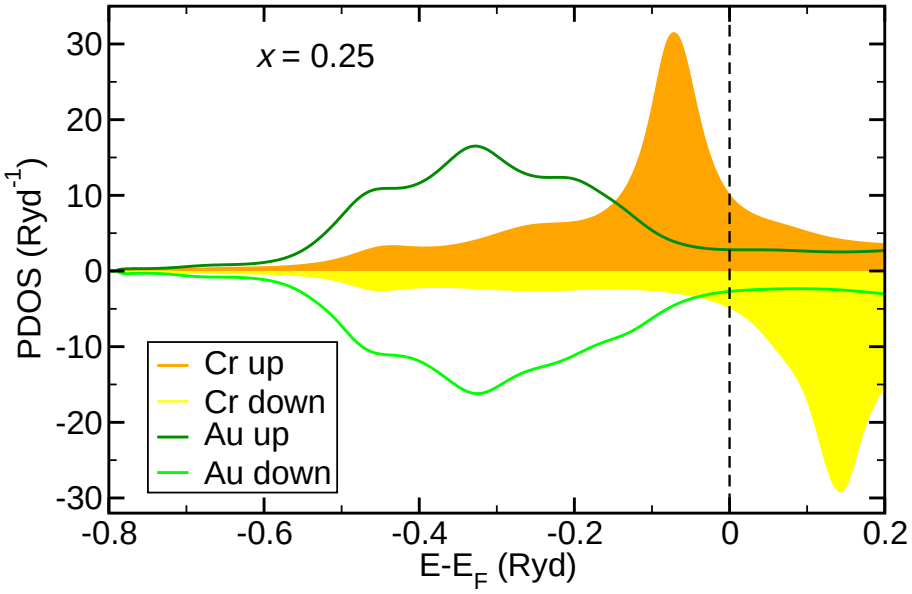

Figure 6.5: The spin-projected density of states, projected on the Au and Cr atoms, for AFM-1Q spin arrangement at the Cr concentration $x = 0.25$ in disordered $Au_{1-x}Cr_x$.

Fig. 6.5 displays the calculated spin-projected densities of states (PDOS), projected on the Au and Cr atoms, of the lowest energy antiferromagnetic 1Q spin configuration for the Cr concentration $x = 0.25$. The density of states did not vary much with the Cr concentration, and the Au atoms were found to carry negligible magnetic moments. The variation of μ_{Cr} with Cr concentration is shown in Fig. 6.6. For comparison, experimentally reported μ_{Cr} values [62, 196, 198, 200] are also shown in the graph which depicts a reasonable agreement between our calculated values and experimental reports.

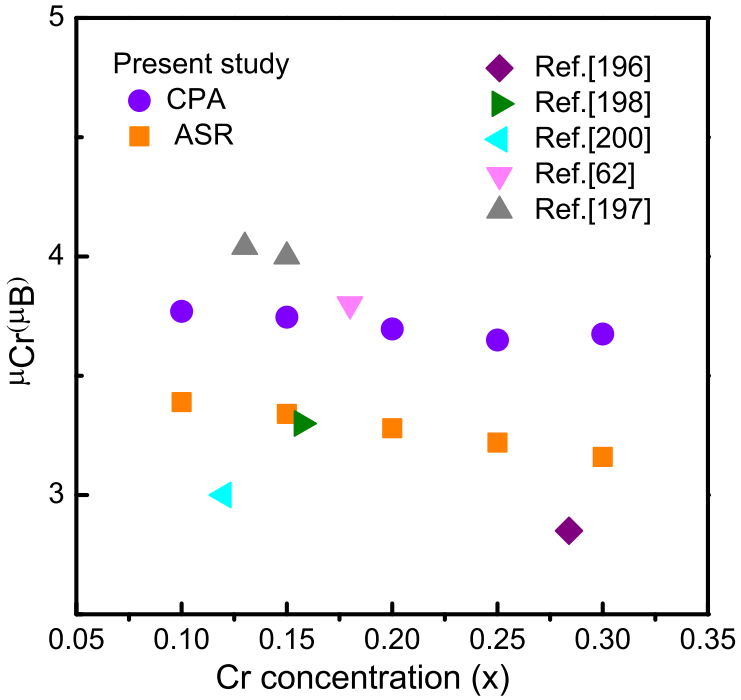

Figure 6.6: Variation of Cr magnetic moment μ_{Cr} with Cr concentration in disordered $Au_{1-x}Cr_x$ alloy.

6.3 Magnetic exchange interaction parameters

The magnetic exchange interaction parameters were calculated using the method of Lichtenstein [117, 118] as described in Sec. 2.2. The variation of nearest neighbor Cr-Cr exchange interaction ($J^{Cr-Cr}(R_0)$) with Cr concentration is shown in Fig. 6.7(a). Fig. 6.7(b) shows the variation of Cr-Cr exchange energy (J^{Cr-Cr}) as a function of Cr-Cr distance for different Cr concentrations. The Cr-Au and Au-Au exchange energies were found to be negligible in comparison with the dominant Cr-Cr interaction energy. $J^{Cr-Cr}(R_0)$ was antiferromagnetic in all the compositions and showed a strong compositional dependence; it increased with increasing Cr concentration. As can be seen from Fig. 6.7(b), the exchange interaction is oscillatory in nature and behaves like a RKKY interaction which is in accordance with the earlier experimental reports [61, 196, 197]. The disorder scattering leads to sharp decay of the exchange interactions with distance

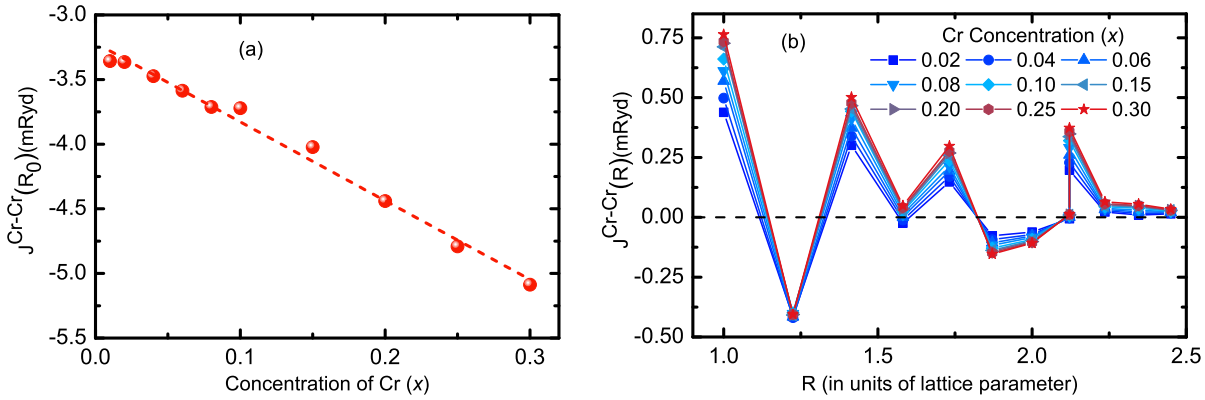

Figure 6.7: (a) Variation of nearest neighbor Cr-Cr magnetic exchange energy $J^{Cr-Cr}(R_0)$ as a function of Cr concentration in disordered $Au_{1-x}Cr_x$ alloy. The dotted line is a guide for straight line. (b) Cr-Cr magnetic exchange energies J^{Cr-Cr} (excluding $J^{Cr-Cr}(R_0)$) as a function of distance R at different Cr concentrations in disordered $Au_{1-x}Cr_x$ alloy.

and asymmetry in oscillatory behavior. The oscillatory nature of J^{Cr-Cr} is the source of frustration in this system which leads to the possibility of a spin glass phase.

6.4 Magnetic phase diagram

Using the magnetic exchange interaction parameters obtained in the above section, a mean field analysis was carried out to draw the magnetic phase diagram of the system. As the Au atoms carry negligible magnetic moments, we neglected their interactions. The starting point of the analysis was the Ising Hamiltonian described below onto which the GPM model [114] maps the problem of magnetic ordering of an alloy system:

$$\mathscr{H} = -\frac{1}{2}\sum_{\mathbf{R}_i}\sum_{\mathbf{R}_j} J\big(|\mathbf{R}_i - \mathbf{R}_j|\big) S_{\mathbf{R}_i} S_{\mathbf{R}_j} \tag{6.5}$$

where $J\big(|\mathbf{R}_i - \mathbf{R}_j|\big)$ is the magnetic exchange interaction between the moments situated at the sites $\mathbf{R}_i$ and $\mathbf{R}_j$, $S_{\mathbf{R}_i}$ takes the values ± 1 according to whether the moment situated at the site $\mathbf{R}_i$ is oriented along the global quantization direction or opposite to it.

As seen in the above section, the dominant magnetic exchange interaction in

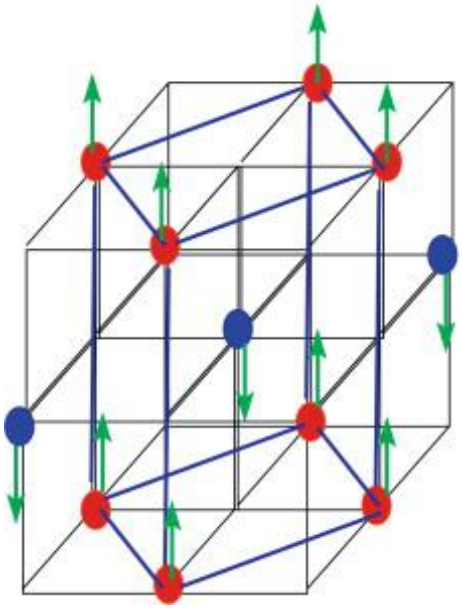

Figure 6.8: The partitioning of FCC lattice for the description of AFM-1Q phase. Atoms in different sublattices are shown in different colors.

the system is the nearest neighbor Cr-Cr interaction ($J^{Cr-Cr}(R_0)$) which is *negative* (i.e., $J^{Cr-Cr}(R_0) < 0$). Consequently the order parameter of the problem cannot be given as $\sigma_{\mathbf{R}_i} = \langle S_{\mathbf{R}_i} \rangle$, rather a staggered version of $\sigma_{\mathbf{R}_i}$ needs to be considered. The FCC lattice has been divided into two interpenetrating sublattices L_1 and L_2 with sides $a/\sqrt{2}, a/\sqrt{2}$, and a as illustrated in Fig. 6.8. These sublattices are arranged such that nearest neighbor of a site in L_1 belongs to L_2 and vice versa. Eight of the nearest neighbors of the original FCC lattice now sit on L_1 and the other four on L_2. Now, the staggered local occupation variable $\widehat{S}_{\mathbf{R}_i}$ and the staggered exchange interaction $\widehat{J}$ can be defined as:

$$\widehat{S}_{\mathbf{R}_i}\widehat{S}_{\mathbf{R}_j} = I_{ij} S_{\mathbf{R}_i} S_{\mathbf{R}_j} \quad \text{and} \quad \widehat{J}\big(|\mathbf{R}_i - \mathbf{R}_j|\big) = I_{ij} J\big(|\mathbf{R}_i - \mathbf{R}_j|\big) \tag{6.6}$$

where $I_{ij} = \pm 1$ according to whether $\mathbf{R}_i$ and $\mathbf{R}_j$ are in same or different sublattices. Then Eq. 6.5 can be rewritten as:

$$\mathscr{H} = -\frac{1}{2} \sum_{\mathbf{R}_i} \sum_{\mathbf{R}_j} \widehat{J}\big(|\mathbf{R}_i - \mathbf{R}_j|\big) \widehat{S}_{\mathbf{R}_i} \widehat{S}_{\mathbf{R}_j} \tag{6.7}$$

The above Hamiltonian describes how the atomic spheres carrying $Cr^{\uparrow}$ and $Cr^{\downarrow}$ atoms are arranged in the ground state. The free energy of the system within single-site mean field approximation is given by [207]:

$$F = \frac{1}{2}\sum_{\mathbf{R}_i}\sum_{\mathbf{R}_j}\widehat{J}\big(|\mathbf{R}_i - \mathbf{R}_j|\big)\widehat{\sigma}_{\mathbf{R}_i}\widehat{\sigma}_{\mathbf{R}_j} - (1/\beta)\sum_{\mathbf{R}_i}\ln\cosh\big(\beta\widehat{h}_{\mathbf{R}_i}\big) \tag{6.8}$$

where $\beta = 1/k_B T$, $\widehat{\sigma}_{\mathbf{R}_i} = \langle\widehat{S}_{\mathbf{R}_i}\rangle$ is the local magnetization and $h_{\mathbf{R}_i}$ is the local random staggered mean-field given by:

$$\widehat{h}_{\mathbf{R}_i} = \sum_{\mathbf{R}_i}\widehat{J}\big(|\mathbf{R}_i - \mathbf{R}_j|\big)\widehat{\sigma}_{\mathbf{R}_i} \tag{6.9}$$

Minimization of the free energy expression of Eq. 6.8 with respect to the local order parameter $\widehat{\sigma}_{\mathbf{R}_i}$ gives its relationship with the local staggered mean field $\widehat{h}_{\mathbf{R}_i}$:

$$\widehat{\sigma}_{\mathbf{R}_i} = \tanh\big(\beta\widehat{h}_{\mathbf{R}_i}\big) \tag{6.10}$$

Now, in a random alloy $\widehat{h}_{\mathbf{R}_i}$ at different sites are themselves random and we need to calculate the probability distribution of these staggered Weiss fields $\Pr\big(\widehat{h}_{\mathbf{R}_i}\big)$. For RKKY interaction, the scaled moments $\widetilde{M}_n = \sum_R \big(\widehat{J}(R)/\widehat{J}(R_0)\big)^n$ decrease rapidly with n and according to the arguments made by Mookerjee [207], and Mookerjee and Roy [208], $\Pr\big(\widehat{h}_{\mathbf{R}_i}\big)$ are Gaussian given by the expression:

$$\Pr(\widehat{h}_{\mathbf{R}_i}) = \sqrt{\frac{1}{2\pi J_1^2}}\exp\left[-\frac{\big(\widehat{h}_{\mathbf{R}_i} - J_0\big)^2}{(2J_1)^2}\right] \tag{6.11}$$

where

$$\begin{aligned} J_0 &= xm\sum_{\mathbf{R}_i}\widehat{J}(\mathbf{R}_i) = mk_B T_N \\ J_1^2 &= xq\sum_{\mathbf{R}_i}\big(\widehat{J}(\mathbf{R}_i)\big)^2 = q(k_B T_{sg})^2 \end{aligned} \tag{6.12}$$

In Eq. 6.12, x is the concentration of magnetic atoms in the system which in the present case is the Cr concentration in the system, m and q are the configuration averaged order parameters of the system:

$$\begin{aligned} m &= \int \widehat{\sigma}_{\mathbf{R}_i}\left(\widehat{h}_{\mathbf{R}_i}\right) \Pr\left(\widehat{h}_{\mathbf{R}_i}\right) \mathrm{d}\widehat{h}_{\mathbf{R}_i} \\ q &= \int \left[\widehat{\sigma}_{\mathbf{R}_i}\left(\widehat{h}_{\mathbf{R}_i}\right)\right]^2 \Pr\left(\widehat{h}_{\mathbf{R}_i}\right) \mathrm{d}\widehat{h}_{\mathbf{R}_i} \end{aligned} \tag{6.13}$$

Substituting Eq. 6.11 and Eq. 6.12 into Eq. 6.13 one can obtain:

$$\begin{aligned} m &= \sqrt{\frac{1}{2\pi}} \int \mathrm{d}z \exp\left(-z^2/2\right) \tanh\left[\beta(mT_N + qT_{sg}z)\right] \\ q &= \sqrt{\frac{1}{2\pi}} \int \mathrm{d}z \exp\left(-z^2/2\right) \tanh^2\left[\beta(mT_N + qT_{sg}z)\right] \end{aligned} \tag{6.14}$$

Different magnetic phases, e.g., long-range ordered ferromagnetic and antiferromagnetic phases, spin glass, paramagnet can be identified from the probability density of the mean field and phase boundaries can be obtained by expanding Eq. 6.14 for small n and q [207]:

(i) m=0, q=0: In this case, the probability density is a delta function at the origin. Then the local mean field vanishes everywhere and the net magnetization is zero. This is characteristic of a paramagnetic arrangement. Such an arrangement is stable for $T > T_N$.

(ii) m=0, q $\neq$ 0: Now the distribution of the local Weiss fields is a Gaussian centered at the origin, but with a spread $k_B T_{sg}\sqrt{q}$. In this case we have a net local magnetization, and the *positive* and *negative* moment sites are distributed randomly. However, as the global averaged moment is zero, the number of *positive* moment sites is equal to the number of *negative* moment sites. This means that the system has a short-range magnetic order without any long-range ordering. This is char-

acteristic of the spin-glass phase. The paramagnetic–spin glass phase boundary is given by $k_B T = \sqrt{x}\sum_{\mathbf{R}_i}\left(\widehat{J}(\mathbf{R}_i)\right)^2$ with critical temperature $T_{sg} = \frac{\sqrt{x}\sum_{\mathbf{R}_i}\left(\widehat{J}(\mathbf{R}_i)\right)^2}{k_B}$.

(iii) m $\neq$ 0, q $\neq$ 0: In this case also the probability density is Gaussian with a spread $k_B T_N \sqrt{q}$ but now centered away from the origin. Therefore, again we have a net local magnetization, and the *positive* and *negative* moment sites are distributed randomly. However, since now the global averaged moment $m \neq 0$, there is antiferromagnetic ordering. This is characteristic of a random antiferromagnetic system. The paramagnetic–antiferromagnetic phase boundary is given by $k_B T = x\sum_{\mathbf{R}_i}\widehat{J}(\mathbf{R}_i)$ with critical temperature $T_N = \frac{x\sum_{\mathbf{R}_i}\widehat{J}(\mathbf{R}_i)}{k_B}$.

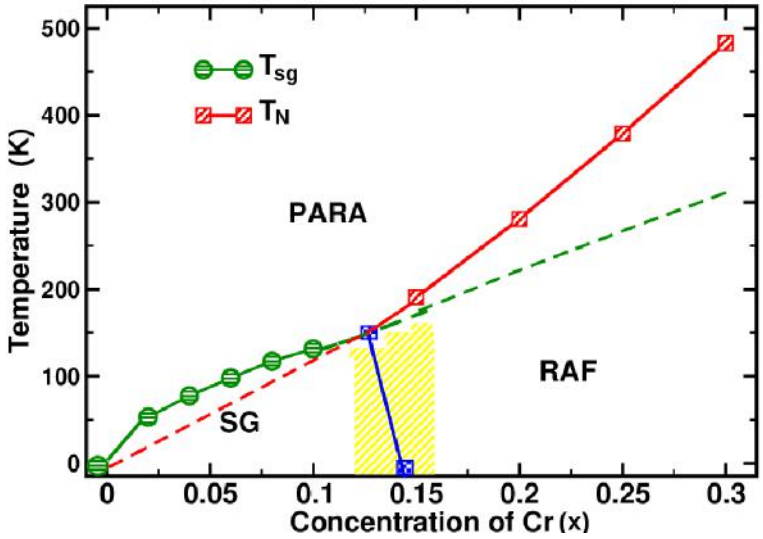

Figure 6.9: Magnetic phase diagram of disordered $Au_{1-x}Cr_x$ alloy. 'PARA' labels the paramagnetic phase, 'RAF' the antiferromagnetic phase, and 'SG' the spin glass phases. T_{sg} and T_N are respectively the spin glass freezing and Néel temperatures.

At $T = 0$, the critical concentration that separates the spin glass state from the antiferromagnetic phase is given by $\sqrt{x}J_0/J_1 = \sqrt{\pi/2}$. The magnetic phase diagram obtained from the above arguments is shown in Fig. 6.9. The shaded region in the figure is the cluster glass region which cannot be adequately described by a single-site mean-field theory described as above.

The obtained magnetic phase diagram of $Au_{1-x}Cr_x$ ($0 \leq x \leq 0.3$) matches

well with the experimental reports of Nakai et al. [61]. The concentration at which the system goes from the spin glass state to the long-range ordered antiferromagnetic phase also agrees well with their experimentally reported value. Although the qualitative agreement of the calculated magnetic phase diagram with experimental report [61] is good, we overestimated the transition temperatures here which is always the case for mean field analysis and is a known drawback.

6.5 Conclusions

Magnetic properties of disordered $Au_{1-x}Cr_x$ ($0 \leq x \leq 0.3$) alloys have been investigated in this chapter using first-principles density functional based theories and mean field analysis, and then compared with experimental reports. The lattice parameters calculated from the minimizations of total energy agree well with the experimentally reported values, however, they showed an increasing deviation from the Vegard's law as the Cr concentration increases in the system due to the size mismatch between the Au and Cr atoms. Various collinear and noncollinear spin configurations have been explored using TB-LMTO-ASR code to find the most stable configuration which showed that the collinear antiferromagnetic spin configuration AFM-1Q is the most stable configuration in the long-range ordered antiferromagnetic region and conforms with the experimental reports. The magnetic phase diagram has been constructed using mean field analysis of the magnetic exchange interaction parameters which qualitatively agrees well with the experimental reports.

7 Conclusions and Future Outlooks

The structural, magnetic and transport properties of magnetic alloys with substitutional type disordered, in which the constituent atoms randomly occupy a regular lattice, have been investigated in this thesis using experimental and theoretical methods. Various aspects of disordered alloys like the effects of short-range ordering and disorder-induced effects like weak localization have been explored.

In disordered $Fe_{1-x}Al_x$ alloy system we have explored the evolution of disordered content or the tendency of forming short-range ordered structure as a function of Al concentration and the associated effects on the magnetic and transport properties. These studies have established a very interesting behavior that disorder increases up to $x = 0.35$ beyond which it decreases with increasing values of x. As lattice parameter of this alloy system increases with disordering, this peculiar evolution of the disorder content in the samples results in a lattice parameter anomaly which has been a longstanding puzzle for this system: lattice parameter increases linearly up to $x \approx 0.30$ beyond which it tends to deviate from linearity, sometimes even decreases and the reported values of lattice parameter varies widely among various reports. This peculiar evolution of disorder with Al concentration also affects the magnetic properties of the system and gives rise anomalous variation of Fe magnetic moment and paramagnetic to ferromagnetic transition temperature. We have shown that with increasing Al concentration the low temperature magnetic state evolves from a ferromagnetic phase at $x = 0.25$ to a spin glass state at higher Al compositions around $x = 0.45$. The presence of short-range ordering at $x = 0.50$ and 0.55 causes a low temperature mixed magnetic phase of fer-

romagnetic and spin glass characters. The peculiar evolution of disorder content in the sample we found as a function of Al concentration can be studied in a future work using diffuse scattering and analysis of the pair distribution function (PDF). By calculating the magnetic exchange interaction parameters from first-principles theories and performing Monte-Carlo simulations we lent further support to the experimentally observed results. To study the effects of short-range ordered structures on the magnetic properties of a disordered system, we carried out Monte-Carlo simulations with SQS which is a superior method of handling inhomogeneous disorder compared to other existing methods. Here we have used this SQS based Monte-Carlo simulation only at the equiatomic composition, however the method can be extended to other non-stoichiometric compositions in future works. The presence of short-range ordered structures and clusters and their influence on the system properties are ubiquitous to disordered systems. The method of SQS based Monte-Carlo simulations can be applied to study such systems.

We then explored the structural, magnetic and transport properties of $FeAl_{2-x}Ga_x$ alloy system. We have shown that with increasing Ga concentration, Ga atoms gradually replace the Al atoms and substitutional disorder increases. Consequently, the temperature T_m at which weak localization of electrons occurs also increases with increasing Ga concentration. The most interesting phenomenon we found in this system is that the antiferromagnetic transition occurs concomitantly with this disorder-induced weak localization. The weak localization temperature T_m and the antiferromagnetic transition temperature T_N follows each as the Ga concentration varies in the system. However, this concomitant nature of the disorder-induced weak localization and the antiferromagnetic transition is not adequately explainable within existing theories of weak localization and this issue should be taken up in future theoretical works. Also, we postulated that the magnetic interactions lie mostly in a plane and the antiferromagnetic transition arises from weak interplaner interactions. This can be explored in a future work via other measurements like neutron diffraction and NMR.

In disordered $Au_{1-x}Cr_x$ alloy system we have investigated the possibility of a noncollinear magnetic structure using DFT and have drawn the magnetic phase diagram of the system through mean field analysis of the magnetic exchange interaction parameters. The results obtained from these theoretical studies are in excellent agreement with experimental reports. Many Mn-based intermetallic disordered alloys show noncollinear magnetic arrangements where this study can be extended to supplement the experimental observations in future works.

In summary, the joint theoretical and experimental studies performed in this thesis has shed light on various aspects of magnetic alloys with the substitutional disorder and also found a novel phenomenon for disordered alloy system. The magnetic phase diagrams of many disordered intermetallic alloys are not completely understood where this type of joint experimental and theoretical studies can be performed to supplement each other, and also would be beneficial for exploring new alloy system.

References

[1] C. Kittel, *Introduction to solid state*, 8th ed. (John Wiley & Sons, 2004).

[2] N. W. Ashcroft and N. D. Mermin, *Solid State Physics* (Saunders College, Philadelphia, 1976).

[3] D. A. Porter, K. E. Easterling, and M. Sherif, *Phase transformations in metals and alloys, (revised reprint)* (CRC press, 2009).

[4] J. W. Christian, *The theory of transformations in metals and alloys* (Pergamon Press, 2002).

[5] F. C. Nix and W. Shockley, Reviews of Modern Physics **10**, 1 (1938).

[6] A. R. Troiano, Metallography, Microstructure, and Analysis **5** (2016).

[7] A. Inoue, Acta materialia **48** (2000).

[8] J. M. Cowley, Physical Review **77**, 669 (1950).

[9] J. M. Cowley, Physical Review **120**, 1648 (1960).

[10] O. Gunnarsson, M. Calandra, and J. E. Han, Review of Modern Physics **75**, 1085 (2003).

[11] N. F. Mott, Philosophical Magazine **26**, 1015 (1972).

[12] M. Gurvitch, Physical Review B **24**, 7404 (1981).

[13] N. E. Hussey, K. Takenaka, and H. Takagi, Philosophical Magazine **84**, 2847 (2004).

[14] P. W. Anderson, Physical Review **109**, 1492 (1958).

[15] A. Lagendijk, B. van Tiggelen, and D. S. Wiersma, Physics Today **62**, 24 (2009).

[16] N. F. Mott and W. D. Twose, Advances in Physics **10**, 107 (1961).

[17] N. F. Mott, Philosophical Magazine **22**, 7 (1970).

[18] N. F. Mott, Journal of Physics C: Solid State Physics **20**, 3075 (1987).

[19] E. Abrahams, P. W. Anderson, D. C. Licciardello, and T. V. Ramakrishnan, Physical Review Letters **42**, 673 (1979).

[20] G. Bergmann, Physics Reports **107**, 1 (1984).

[21] M. A. Howson and B. L. Gallagher, Physics Reports **170**, 265 (1988).

[22] B. Kramer and A. MacKinnon, Reports on Progress in Physics **56**, 1469 (1993).

[23] Y. Zhou and S. Ramanathan, Critical Reviews in Solid State and Materials Sciences **38**, 286 (2013).

[24] P. A. Lee and T. V. Ramakrishnan, Review of Modern Physics **57**, 287 (1985).

[25] D. Belitz and T. R. Kirkpatrick, Reviews of modern physics **66**, 261 (1994).

[26] J. A. Mydosh, *Spin glasses: an experimental introduction* (Taylor and Francis, 1993).

[27] P. J. Ford, Contemporary Physics **23**, 141 (1982).

[28] K. Binder and A. P. Young, Reviews of Modern physics **58**, 801 (1986).

[29] J. A. Mydosh, Reports on Progress in Physics **78**, 052501 (2015).

[30] A. P. Murani, Journal of Magnetism and Magnetic Materials **5**, 95 (1977).

[31] V. Cannella and J. A. Mydosh, Physical Review B **6**, 4220 (1972).

[32] M. A. Ruderman and C. Kittel, Physical Review **96**, 99 (1954).

[33] T. Kasuya, Progress of Theoretical Physics **16**, 45 (1956).

[34] K. Yosida, Physical Review **106**, 893 (1957).

[35] S. F. Edwards and P. W. Anderson, Journal of Physics F: Metal Physics **5**, 965 (1975).

[36] L. Kouwenhoven and L. Glazman, Physics world **14**, 33 (2001).

[37] A. C. Hewson, *The kondo problem to heavy fermions*, Vol. 2 (Cambridge university press, 1997).

[38] J. Kondo, Journal of the Physical Society of Japan **74**, 1 (2005).

[39] J. Kondo, Progress of theoretical physics **32**, 37 (1964).

[40] M. P. Sarachik, E. Corenzwit, and L. D. Longinotti, Physical Review **135**, A1041 (1964).

[41] D. R. Hamann, Physical Review **158**, 570 (1967).

[42] P. G. Gonzales-Ormeño, H. M. Petrilli, and C. G. Schön, Scripta Materialia **54**, 1271 (2006).

[43] F. Stein and M. Palm, International journal of materials research **98**, 580 (2007).

[44] B. Sundman, I. Ohnuma, N. Dupin, U. R. Kattner, and S. G. Fries, Acta Materialia **57**, 2896 (2009).

[45] K. Han, I. Ohnuma, and R. Kainuma, Journal of Alloys and Compounds **668**, 97 (2016).

[46] G. A. Perez Alcazar and E. Galvao da Silva, Journal of Physics F: Metal Physics **17**, 2323 (1987).

[47] E. P. Yelsukov, E. V. Voronina, and V. A. Barinov, Journal of Magnetism and Magnetic Materials **115**, 271 (1992).

[48] K. Sumiyama, Y. Hirose, and Y. Nakamura, Journal of the Physical Society of Japan **59**, 2963 (1990).

[49] S. A. Makhlouf, M. Shiga, and K. Sumiyama, Journal of the Physical Society of Japan **60**, 3537 (1991).

[50] M. Shiga and Y. Nakamura, Journal of the Physical Society of Japan **40**, 1295 (1976).

[51] E. Menéndez, M. O. Liedke, J. Fassbender, T. Gemming, A. Weber, L. J. Heyderman, K. V. Rao, S. C. Deevi, S. Suriñach, M. D. Baró, J Sort, and J. Nogués, small **5**, 229 (2009).

[52] R. Bali, S. Wintz, F. Meutzner, R. Hübner, R. Boucher, A. A. Ünal, S. Valencia, A. Neudert, K. Potzger, J. Bauch, F. Kronast, S. Facsko, J. Lindner, and J. Fassbender, Nano letters **14**, 435 (2014).

[53] M. Mihalkovič and M. Widom, Physical Review B **85**, 014113 (2012).

[54] I. Chumak, K. W. Richter, and H. Ehrenberg, Acta Crystallographica Section C **66**, i87 (2010).

[55] C. S. Lue, Y. Öner, D. G. Naugle, and Joseph H. Ross, Physical Review B **63**, 184405 (2001).

[56] J. Chi, Y. Li, F. G. Vagizov, V. Goruganti, and J. H. Ross, Physical Review B **71**, 024431 (2005).

[57] D. Kaptás, E. Sváb, Z. Somogyvári, G. André, L. F. Kiss, J. Balogh, L. Bujdosó, T. Kemény, and I. Vincze, Physical Review B **73**, 012401 (2006).

[58] Z. Jagličić, S. Vrtnik, M. Feuerbacher, and J. Dolinšek, Physical Review B **83**, 224427 (2011).

[59] M. Mihalkovič, M. Krajčí, and M. Widom, Physical Review B **87**, 100201 (2013).

[60] M. Weinert and R. E. Watson, Physical Review B **58**, 9732 (1998).

[61] Y. Nakai, M. Sakuma, and N. Kunitomi, Journal of the Physical Society of Japan **56**, 301 (1987).

[62] S. Radha, A. K. Nigam, S. K. Malik, and Girish Chandra, Journal of Magnetism and Magnetic Materials **140**, 101 (1995).

[63] Y. Endoh and Y. Ishikawa, Journal of the Physical Society of Japan **30**, 1614 (1971).

[64] S. J. Kennedy and T. J. Hicks, Journal of Physics F: Metal Physics **17**, 1599 (1987).

[65] K. Sasao, R. Y. Umetsu, K. Fukamichi, and A. Sakuma, Journal of Alloys and Compounds **352**, 21 (2003).

[66] A. Kohn, A. Kovács, R. Fan, G. J. McIntyre, R. C. C. Ward, and J. P. Goff, Scientific reports **3** (2013).

[67] J. M. D. Coey, Canadian Journal of Physics **65**, 1210 (1987).

[68] A. Z. Menshikov and G. P. Gasnikova, Journal of Physics: Condensed Matter **6**, 791 (1994).

[69] J. Goldstein, D. E. Newbury, P. Echlin, D. C. Joy, A. D. Romig Jr, C. E. Lyman, C. Fiori, and E. Lifshin, *Scanning electron microscopy and x-ray microanalysis: a text for biologists, materials scientists, and geologists* (Plenum Press, 2nd edn, 1992, 1992).

[70] B. D. Cullity, *Elements of x-ray diffraction* (Addison-Wesley Pub. Co., 1978).

[71] `https://en.wikipedia.org/wiki/X-ray_crystallography`.

[72] B. E. Warren, *X-ray diffraction* (Courier Corporation, 1969).

[73] L. Lutterotti, S. Matthies, H.-R. Wenk, A. S. Schultz, and J. W. Richardson Jr., Journal of Applied Physics **81**, 594 (1997).

[74] L. Lutterotti, D. Chateigner, S. Ferrari, and J. Ricote, Thin Solid Films **450**, 34 (2004).

[75] L. Lutterotti, Nuclear Instruments and Methods in Physics Research Section B: Beam Interactions with Materials and Atoms **268**, 334 (2010).

[76] *Low level measurements handbook* (6th ed., Keithley Instruments Inc., USA, 2004).

[77] R. Nath, "Investigation of novel electrical and magnetic properties of perovskite oxides", PhD thesis (University of Calcutta, 2015).

[78] `https://en.wikipedia.org/wiki/Vibrating_sample_magnetometer`.

[79] S. Foner, Review of Scientific Instruments **30**, 548 (1959).

[80] B. D. Josephson, Physics letters **1**, 251 (1962).

[81] `https://en.wikipedia.org/wiki/SQUID`.

[82] O. K. Andersen and O. Jepsen, Physical Review Letters **53**, 2571 (1984).

[83] A. Mookerjee, Journal of Physics C: Solid State Physics **6**, 1340 (1973).

[84] A. Zunger, S. H. Wei, L. G. Ferreira, and J. E. Bernard, Physical Review Letters **65**, 353 (1990).

[85] P. Soven, Physical Review **156**, 809 (1967).

[86] B. Velický, Physical Review **184**, 614 (1969).

[87] B. L. Gyorffy, Physical Review B **5**, 2382 (1972).

[88] F. Yonezawa and K. Morigaki, Progress of Theoretical Physics Supplement **53**, 1 (1973).

[89] R. M. Martin, *Electronic structure: basic theory and practical methods* (Cambridge university press, 2004).

[90] P. Hohenberg and W. Kohn, Physical Review **136**, B864 (1964).

[91] W. Kohn and L. J. Sham, Physical Review **140**, A1133 (1965).

[92] D. M. Ceperley and B. J. Alder, Physical Review Letters **45**, 566 (1980).

[93] J. P. Perdew and Y. Wang, Physical Review B **45**, 13244 (1992).

[94] J. P. Perdew, K. Burke, and M. Ernzerhof, Physical Review Letters **77**, 3865 (1996).

[95] O. K. Andersen, Physical Review B **12**, 3060 (1975).

[96] H. L. Skriver, *The lmto method: muffin-tin orbitals and electronic structure*, Vol. 41 (Springer, 2012).

[97] A. Mookerjee and D. D. Sarma, *Electronic structure of alloys, surfaces and clusters* (CRC Press, 2002).

[98] J. Korringa, Physica **13**, 392 (1947).

[99] W. Kohn and N. Rostoker, Physical Review **94**, 1111 (1954).

[100] G. M. Stocks, W. M. Temmerman, and B. L. Gyorffy, Physical Review Letters **41**, 339 (1978).

[101] A. Mookerjee, Journal of Physics C: Solid State Physics **6**, L205 (1973).

[102] T. Saha, I. Dasgupta, and A. Mookerjee, Journal of Physics: Condensed Matter **6**, L245 (1994).

[103] T. Saha, I. Dasgupta, and A. Mookerjee, Physical Review B **50**, 13267 (1994).

[104] R. Haydock, V. Heine, and M. J. Kelly, Journal of Physics C: Solid State Physics **5**, 2845 (1972).

[105] A. Chakrabarti and A. Mookerjee, Journal of Physics: Condensed Matter **13**, 10149 (2001).

[106] A. Alam, T. Saha-Dasgupta, and A. Mookerjee, Physical Review B **81**, 054201 (2010).

[107] A. Alam, T. Saha-Dasgupta, A. Mookerjee, A. Chakrabarti, and G. P. Das, Physical Review B **75**, 134203 (2007).

[108] R. Banerjee and A. Mookerjee, International Journal of Modern Physics C **21**, 205 (2010).

[109] S. H. Wei, L. G. Ferreira, J. E. Bernard, and A. Zunger, Physical Review B **42**, 9622 (1990).

[110] A. P. Jena, "Study of electronic, structural, and magnetic properties of disordered solids", PhD thesis (University of Calcutta, 2014).

[111] K. A. Mäder and A. Zunger, Physical Review B **51**, 10462 (1995).

[112] J. von Pezold, A. Dick, M. Friák, and J. Neugebauer, Physical Review B **81**, 094203 (2010).

[113] A. Van de Walle, P. Tiwary, M. De Jong, D. L. Olmsted, M. Asta, A. Dick, D. Shin, Y. Wang, L. Q. Chen, and Z. K. Liu, Calphad **42**, 13 (2013).

[114] F. Ducastelle and F. Gautier, Journal of Physics F: Metal Physics **6**, 2039 (1976).

[115] I. Dasgupta, T. Saha, and A. Mookerjee, Physical Review B **51**, 3413 (1995).

[116] N. R. Burke, Surface Science **58**, 349 (1976).

[117] A. I. Liechtenstein, M. I. Katsnelson, and V. A. Gubanov, Journal of Physics F: Metal Physics **14**, L125 (1984).

[118] A. I. Liechtenstein, M. I. Katsnelson, V. P. Antropov, and V. A. Gubanov, Journal of Magnetism and Magnetic Materials **67**, 65 (1987).

[119] I. Turek, J. Kudrnovskỳ, V. Drchal, and P. Bruno, Philosophical Magazine **86**, 1713 (2006).

[120] I. A. Abrikosov, S. I. Simak, B. Johansson, A. V. Ruban, and H. L. Skriver, Physical Review B **56**, 9319 (1997).

[121] H. Ebert, D. Koedderitzsch, and J. Minar, Reports on Progress in Physics **74**, 096501 (2011).

[122] G. R. Caskey, J. M. Franz, and D. J. Sellmyer, Journal of Physics and Chemistry of Solids **34**, 1179 (1973).

[123] J. Bogner, W. Steiner, M. Reissner, P. Mohn, P. Blaha, K. Schwarz, R. Krachler, H. Ipser, and B. Sepiol, Physical Review B **58**, 14922 (1998).

[124] N. I. Kulikov, A. V. Postnikov, G. Borstel, and J. Braun, Physical Review B **59**, 6824 (1999).

[125] G. P. Das, B. K. Rao, P. Jena, and S. C. Deevi, Physical Review B **66**, 184203 (2002).

[126] Y. M. Gu and L. Fritsche, Journal of Physics: Condensed Matter **4**, 1905 (1992).

[127] J. Zou and C. L. Fu, Physical Review B **51**, 2115 (1995).

[128] S. K. Bose, V. Drchal, J. Kudrnovský, O. Jepsen, and O. K. Andersen, Physical Review B **55**, 8184 (1997).

[129] E. Apiñaniz, F. Plazaola, and J. S. Garitaonandia, The European Physical Journal B - Condensed Matter and Complex Systems **31**, 167 (2003).

[130] H. Chacham, E. Galvo da Silva, D. Guenzburger, and D. E. Ellis, Physical Review B **35**, 1602 (1987).

[131] V. Sundararajan, B. R. Sahu, D. G. Kanhere, P. V. Panat, and G. P. Das, Journal of Physics: Condensed Matter **7**, 6019 (1995).

[132] A. V. Smirnov, W. A. Shelton, and D. D. Johnson, Physical Review B **71**, 064408 (2005).

[133] P. Mohn, C. Persson, P. Blaha, K. Schwarz, P. Novák, and H. Eschrig, Physical Review Letters **87**, 196401 (2001).

[134] A. Galler, C. Taranto, M. Wallerberger, M. Kaltak, G. Kresse, G. Sangiovanni, A. Toschi, and K. Held, Physical Review B **92**, 205132 (2015).

[135] G. P. Huffman and R. M. Fisher, Journal of Applied Physics **38**, 735 (1967).

[136] M. J. Besnus, A. Herr, and A. J. P. Meyer, Journal of Physics F: Metal Physics **5**, 2138 (1975).

[137] H. Xiao and I. Baker, Acta Metallurgica et Materialia **43**, 391 (1995).

[138] D. G. Morris, J. C. Joye, and M. Leboeuf, Philosophical Magazine A **69**, 961 (1994).

[139] Y. A. Chang, L. M. Pike, C. T. Liu, A. R. Bilbrey, and D. S. Stone, Intermetallics **1**, 107 (1993).

[140] J. L. Jordan and S. C. Deevi, Intermetallics **11**, 507 (2003).

[141] I. Baker and P. R. Munroe, International Materials Reviews **42**, 181 (1997).

[142] C. T. Liu, E. P. George, P. J. Maziasz, and J. H. Schneibel, Materials Science and Engineering: A **258**, 84 (1998).

[143] H. Domke and L. K. Thomas, Journal of Magnetism and Magnetic Materials **45**, 305 (1984).

[144] C. L. Fu, Y.-Y. Ye, M. H. Yoo, and K. M. Ho, Physical Review B **48**, 6712 (1993).

[145] R. J. Wasilewski, Journal of Physics and Chemistry of Solids **29**, 39 (1968).

[146] A. Parthasarathi and P. A. Beck, Solid State Communications **18**, 211 (1976).

[147] R. Wagoner, M. Reissner, W. Steiner, J. Bogner, H. Sassik, P. Pongratz, and B. Sepiol, Journal of Magnetism and Magnetic Materials **140**, 57 (1995).

[148] C. Gammer, C. Mangler, H. P. Karnthaler, and C. Rentenberger, Scripta Materialia **65**, 57 (2011).

[149] K. Szymański, D. Satuła, L. Dobrzyński, E. Voronina, E. P. Yelsukov, and T. Miyanaga, Physical Review B **72**, 104409 (2005).

[150] R. Brajpuriya, P. Sharma, S. Jani, S. Kaimal, T. Shripathi, N. Lakshmi, and K. Venugopalan, Applied Surface Science **257**, 10 (2010).

[151] N. Metropolis, A. W. Rosenbluth, M. N. Rosenbluth, A. H. Teller, and E. Teller, The journal of chemical physics **21**, 1087 (1953).

[152] D. Negri, A. R. Yavari, and A. Deriu, Acta materialia **47**, 4545 (1999).

[153] E. Apiñaniz, F. Plazaola, J. S. Garitaonandia, D. Marti n, and J. A. Jiménez, Journal of applied physics **93**, 7649 (2003).

[154] S. Gialanella, X. Amils, M. D. Baro, P. Delcroix, G. Le Caër, L. Lutterotti, and S. Suriñach, Acta materialia **46**, 3305 (1998).

[155] A. Hernando, X. Amils, J. Nogués, S. Suriñach, M. D. Baró, and M. R. Ibarra, Physical Review B **58**, R11864 (1998).

[156] J. Nogués, E. Apiñaniz, J. Sort, M. Amboage, M. d'Astuto, O. Mathon, R. Puzniak, I. Fita, J. S. Garitaonandia, S. Suriñach, J. S. Muñoz, M. D. Baró, F. Plazaola, and F. Baudelet, Physical Review B **74**, 024407 (2006).

[157] S. Gialanella, Intermetallics **3**, 73 (1995).

[158] D. A. Eelman, J. R. Dahn, G. R. MacKay, and R. A. Dunlap, Journal of Alloys and Compounds **266**, 234 (1998).

[159] S. Enzo, R. Frattini, R. Gupta, P. P. Macri, G. Principi, L. Schiffini, and G. Scipione, Acta materialia **44**, 3105 (1996).

[160] L. E. Zamora, G. A. Pérez Alcázar, G. Y. Vélez, J. D. Betancur, J. F. Marco, J. J. Romero, A. Martínez, F. J. Palomares, and J. M. González, Physical Review B **79**, 094418 (2009).

[161] D. M. Rodríguez, E. Apiñaniz, J. S. Garitaonandia, F. Plazaola, D. S. Schmool, and G. Cuello, Journal of magnetism and magnetic materials **272**, 1510 (2004).

[162] E. Menéndez, J. Sort, M. O. Liedke, J. Fassbender, S. Suriñach, M. D. Baró, and J. Nogués, New journal of physics **10**, 103030 (2008).

[163] D. M. Rodríguez, E. Apiñaniz, F. Plazaola, J. S. Garitaonandia, J. A. Jiménez, D. S. Schmool, and G. J. Cuello, Physical Review B **71**, 212408 (2005).

[164] X. Amils, J. Nogués, S. Suriñach, J. S. Muñoz, L. Lutterotti, S. Gialanella, and M. D. Baró, Nanostructured Materials **11**, 689 (1999).

[165] N. F. Mott, in Proceedings of the royal society of london a: mathematical, physical and engineering sciences, Vol. 153, 880 (The Royal Society, 1936), pp. 699–717.

[166] A. H. Wilson, Proceedings of the Royal Society of London. Series A, Mathematical and Physical Sciences, 580 (1938).

[167] I. Mannari, Progress of Theoretical Physics **22**, 335 (1959).

[168] N. Rivier and K. Adkins, Journal of Physics F: Metal Physics **5**, 1745 (1975).

[169] P. Shukla and M. Wortis, Physical Review B **21**, 159 (1980).

[170] D. A. Venero, R. R. García, L. F. Barquín, E. Apiñaniz, J. S. Garitaonandia, and F. Plazaola, IEEE Transactions on Magnetics **44**, 3883 (2008).

[171] G. A. P. Alcazar, J. A. Plascak, and E. G. da Silva, Physical Review B **34**, 1940 (1986).

[172] A. S. Freitas, D. F. de Albuquerque, I. P. Fittipaldi, and N. O. Moreno, Journal of Applied Physics **113**, 093903 (2013).

[173] J. A. Plascak, L. E. Zamora, and G. A. Pérez Alcazar, Physical Review B **61**, 3188 (2000).

[174] J. Restrepo, G. A. Pérez Alcazar, and D. P. Landau, Journal of Applied Physics **89**, 7341 (2001).

[175] J. Restrepo, J. M. González, and G. A. Pérez Alcazar, Journal of applied physics **81**, 5270 (1997).

[176] D. A. Dias, J. R. de Sousa, and J. A. Plascak, Physics Letters A **373**, 3513 (2009).

[177] A. S. Freitas, D. F. de Albuquerque, and N. O. Moreno, Physica A: Statistical Mechanics and its Applications **391**, 6332 (2012).

[178] W. R. Aguirre Contreras, L. E. Zamora, G. A. Pérez Alcázar, and J. A. Plascak, Physical Review B **72**, 052402 (2005).

[179] M. Salazar, L. E. Zamora, G. A. P. Alcazar, J. A. Plascak, and W. R. Aguirre, Physica B: Condensed Matter **320**, 236 (2002).

[180] J. Restrepo, G. A. Pérez Alcázar, and D. P. Landau, Journal of Applied Physics **87**, 6528 (2000).

[181] H. Kawamura, Journal of the Physical Society of Japan **79**, 011007 (2010).

[182] J. R. L. de Almeida and D. J. Thouless, Journal of Physics A: Mathematical and General **11**, 983 (1978).

[183] M. Gabay and G. Toulouse, Physical Review Letters **47**, 201 (1981).

[184] J. Chi, X. Zheng, S. Y. Rodriguez, Y. Li, W. Gou, V. Goruganti, K. D. D. Rathnayaka, and J. H. Ross, Physical Review B **82**, 174419 (2010).

[185] S. Srinivas, S. N. Kaul, and S. N. Kane, Journal of non-crystalline solids **248**, 211 (1999).

[186] J. M. Ziman, Philosophical Magazine **6**, 1013 (1961).

[187] S. R. Nagel, Physical Review B **16**, 1694 (1977).

[188] P. J. Cote and L. V. Meisel, Physical Review Letters **39**, 102 (1977).

[189] S. N. Kaul, W. Kettler, and M. Rosenberg, Physical Review B **33**, 4987 (1986).

[190] T. Chui, P. Lindenfeld, W. L. McLean, and K. Mui, Physical Review Letters **47**, 1617 (1981).

[191] A. Kawabata, Solid State Communications **34**, 431 (1980).

[192] A. Kawabata, Journal of the Physical Society of Japan **49**, 628 (1980).

[193] K. Yasukochi, Y. Kuwasawa, K. Sekizawa, K. Sugiyama, N. Usui, and T. Ogasawara, Journal of the Physical Society of Japan **19**, 1259 (1964).

[194] K. Inoue, Y. Nakamura, and N. Kunitomi, Journal of the Physical Society of Japan **27**, 1159 (1969).

[195] M. Kohgi, T. Yamada, N. Kunitomi, and Y. Maeda, Journal of the Physical Society of Japan **28**, 793 (1970).

[196] N. Kunitomi, Y. Nakai, Y. Yamada, and K. Inoue, Journal of the Physical Society of Japan **28**, 795 (1970).

[197] Y. Nakai, N. Kunitomi, and Y. Yamada, Journal of the Physical Society of Japan **29**, 978 (1970).

[198] Y. Nakai, N. Kunitomi, Y. Endoh, and Y. Ishikawa, Solid State Communications **9**, 921 (1971).

[199] K. Okuda and Y. Nakai, Journal of the Physical Society of Japan **32**, 639 (1972).

[200] Y. Nakai, T. Urano, and N. Kunitomi, Journal of the Physical Society of Japan **34**, 1197 (1973).

[201] A. Bergman, L. Nordström, A. B. Klautau, S. Frota-Pessôa, and O. Eriksson, Physical Review B **73**, 174434 (2006).

[202] S. Ganguly, M. Costa, A. B. Klautau, A. Bergman, B. Sanyal, A. Mookerjee, and O. Eriksson, Physical Review B **83**, 094407 (2011).

[203] K. Koga and K. Ohshima, Journal of Physics: Condensed Matter **2**, 5647 (1990).

[204] A. V. Ruban and H. L. Skriver, Physical Review B **66**, 024201 (2002).

[205] A. V. Ruban, S. Shallcross, S. I. Simak, and H. L. Skriver, Physical Review B **70**, 125115 (2004).

[206] A. R. Denton and N. W. Ashcroft, Physical Review A **43**, 3161 (1991).

[207] A. Mookerjee, Pramana **11**, 223 (1978).

[208] A. Mookerjee and S. B. Roy, Pramana **21**, 171 (1983).